University of Glasgow

Development and Application of Quantitative Image Analysis for Preclinical MRI Research

HAITHAM FAROOQ IBRAHIM AL-MUBARAK

B.Sc., M.Sc.

SUBMITTED IN FULFILMENT OF THE REQUIREMENTS FOR THE DEGREE OF

Doctor of Philosophy

Institute of Neuroscience and Psychology

College of Medical, Veterinary and Life Sciences

April 2020

Summary

The aim of this thesis is to develop quantitative analysis methods to validate MRI and improve the detection of tumour infiltration. The major components include a description of the development the quantitative methods to better validate imaging biomarkers and detect of infiltration of tumour cells into normal tissue, which were then applied to a mouse model of glioblastoma invasion. To do this, a new histology model, called Stacked In-plane Histology (SIH), was developed to allow a quantitative analysis of MRI.

Validating imaging biomarkers for glioblastoma infiltration

Cancer can be defined as a disease in which a group of abnormal cells grow uncontrollably, often with fatal outcomes. According to (Cancer research UK, 2019), there are more than 363,000 new cancer cases in the UK every year, an increase from the 990 cases reported daily in 2014-2016, with only half of all patients recovering.

Glioblastoma (GB) is the most frequent and malignant form of primary brain tumours with a very poor prognosis. Even with the development of modern diagnostic strategies and new therapies, the five-year survival rate is just 5%, with the median survival time only 14 months.

Unfortunately, glioblastoma can affect patients at any age, including young children, but has a peak occurrence between the ages of 65 and 75 years. The standard treatment for GB consists of surgical resection, followed by radiotherapy and chemotherapy. However, the infiltration of GB cells into healthy adjacent brain tissue is a major obstacle for successful treatment, making complete removal of a tumour by surgery a difficult task, with the potential for tumour recurrence.

Magnetic Resonance Imaging (MRI) is a non-invasive, multipurpose imaging tool used for the diagnosis and monitoring of cancerous tumours. It can provide morphological, physiological, and metabolic information about the tumour. Currently, MRI is the standard diagnostic tool for GB before the pathological examination of tissue from surgical resection or biopsy specimens. The standard

MRI sequences used for diagnosis of GB include T2-Weighted (T2W), T1-Weighted (T1W), Fluid-Attenuated Inversion Recovery (FLAIR), and Contrast Enhance T1 gadolinium (CE-T1) scans. These conventional scans are used to localize the tumour, in addition to associated oedema and necrosis. Although these scans can identify the bulk of the tumour, it is known that they do not detect regions infiltrated by GB cells.

The MRI signal depends upon many physical parameters including water content, local structure, tumbling rates, diffusion, and hypoxia (Dominietto, 2014). There has been considerable interest in identifying whether such biologically indirect image contrasts can be used as non-invasive imaging biomarkers, either for normal biological functions, pathogenic processes or pharmacological responses to therapeutic interventions (Atkinson et al., 2001). In fact, when new MRI methods are proposed as imaging biomarkers of particular diseases, it is crucial that they are validated against histopathology. In humans, such validation is limited to a biopsy, which is the gold standard of diagnosis for most types of cancer. Some types of biopsies can take an image-guided approach using MRI, Computed Tomography (CT) or Ultrasound (US). However, a biopsy may miss the most malignant region of the tumour and is difficult to repeat. Biomarker validation can be performed in preclinical disease models, where the animal can be terminated immediately after imaging for histological analysis. Here, in principle, co-registration of the biomarker images with the histopathology would allow for direct validation. However, in practice, most preclinical validation studies have been limited to using simple visual comparisons to assess the correlation between the imaging biomarker and underlying histopathology.

First objective (Chapter 5): Histopathology is the gold standard for assessing non-invasive imaging biomarkers, with most validation approaches involving a qualitative visual inspection. To allow a more quantitative analysis, previous studies have attempted to co-register MRI with histology. However, these studies have focused on developing better algorithms to deal with the distortions common in histology sections. By contrast, we have taken an approach to improve the quality of the histological processing and analysis, for example, by taking into account the imaging slice orientation and thickness. Multiple histology sections were cut in the MR imaging plane to produce a Stacked In-plane Histology (SIH) map. This approach, which is applied to the next two objectives, creates a

histopathology map which can be used as the gold standard to quantitatively validate imaging biomarkers.

Second objective (Chapter 6): Glioblastoma is the most malignant form of primary brain tumour and recurrence following treatment is common. Non-invasive MR imaging is an important component of brain tumour diagnosis and treatment planning. Unfortunately, clinic MRI (T1W, T2W, CE-T1, and FLAIR) fails to detect regions of glioblastoma cell infiltration beyond the solid tumour region identified by contrast enhanced T1 scans. However, advanced MRI techniques such as Arterial Spin Labelling (ASL) could provide us with extra information (perfusion) which may allow better detection of infiltration. In order to assess whether local perfusion perturbation could provide a useful biomarker for glioblastoma cell infiltration, we quantitatively analysed the correlation between perfusion MRI (ASL) and stacked in-plane histology. This work used a mouse model of glioblastoma that mimics the infiltrative behaviour found in human patients. The results demonstrate the ability of perfusion imaging to probe regions of low tumour cell infiltration, while confirming the sensitivity limitations of clinic imaging modalities.

Third objective (Chapter 7): It is widely hypothesised that Multiparametric MRI (mpMRI), can extract more information than is obtained from the constituent individual MR images, by reconstructing a single map that contains complementary information. Using the MRI and histology dataset from objective 2, we used a multi-regression algorithm to reconstruct a single map which was highly correlated ($r>0.6$) with histology. The results are promising, showing that mpMRI can better predict the whole tumour region, including the region of tumour cell infiltration.

Table of Contents

Chapter 1: General introduction to imaging and treatment of brain tumours

1.1 Background to cancer 2
1.2 The brain anatomy 2
1.3 Brain tumours 2
1.4 Glioma 3
1.5 Glioblastoma 4
1.6 Medical imaging of GB 5
1.7 Treatment of glioblastoma 7
1.7.1 Surgery 7
1.7.2 Radiotherapy 8
1.7.3 Chemotherapy 9
1.8 Preclinical GB models 10

Chapter 2: The theory of magnetic resonance imaging

2.1 Background of MRI 13
2.2 MRI principle 13
2.2.1 Resonance 16
2.2.2 RF pulse 17
2.3 Relaxation 17
2.3.1 T1 relaxation 18
2.3.2 T2 relaxation 19
2.3.3 T2 * relaxation 19
2.4 Gradients 20
2.5 Gradient and spin echo sequences 22
2.6 MR signal 24
2.7 k-space 25
2.8 Main parts of MRI scanner 27
2.9 Applications of relaxation 28
2.9.1 T1 Weighted imaging 29
2.9.2 T2 Weighted imaging 29
2.10 Diffusion 30
2.10.1 Diffusion encoding 31
2.10.2 Apparent diffusion coefficient 33
2.10.3 Diffusion tensor imaging 34
2.11 Applications of diffusion weighted imaging 36

2.12 Blood brain barrier integrity 37
2.13 Perfusion 38
2.14 Perfusion weighted magnetic resonance imaging 39
2.14.1 Contrast Enhanced T1 40
2.14.2 Dynamic contrast enhanced 41
2.14.3 Dynamic susceptibility contrast MRI 41
2.14.4 Arterial spin labelling 41
2.15 Application of ASL 45

Chapter 3: An introduction to image analysis techniques
3.1 Introduction 47
3.2 MRI pre-processing 47
3.2.1 Retrieve data 47
3.2.2 Normalization 47
3.2.3 Sensitivity of surface coil 48
3.2.4 ADC map calculation 49
3.2.5 Skull stripping 49
3.2.6 Filter 50
3.3 MRI Post-processing 52
3.3.1 Segmentation 52
3.3.2 Registration 55
3.4 Histology 58
3.4.1 Pre-processing histology 60
3.4.2 Post-processing histology 61
3.5 Validation Measurement 61
3.5.1 Visual assessment 61
3.5.2 Dice similarity coefficient 61
3.5.3 ROC analysis 62
3.5.4 Reproducibility 63

Chapter 4: Material and experimental methods
4.1 Animal study design 66
4.1.1 Mice and tumour implantation 66
4.1.2 Experimental design 67
4.1.3 MRI acquisition 68
4.1.4 Histology protocols 71

Chapter 5: Stacked in-plane histology for quantitative validation application to an infiltrative brain tumour model

5.1 Introduction 74

5.2 Experimental protocol 77

5.3 Data processing pipeline 79

5.4 MRI data analysis 79

5.5 Histology data analysis 80

5.5.1 Histology to MRI co-registration and production of 3D matrices 80

5.5.2 Segmentation protocol 81

5.5.3 Statistical analysis 82

5.6 Results & Discussion 82

5.6.1 Tumour volume measurement via single-section histology (SSH) 83

5.6.2 Determining optimal number of histology sections for SIH maps 84

5.6.3 SIH to MRI registration quality 86

5.6.4 Volumetric assessment of SIH maps 87

5.6.5 Towards voxel-by-voxel assessment 89

5.7 Conclusion 91

Chapter 6: Quantitative histopathological assessment of perfusion MRI as a marker of GB infiltration

6.1 Introduction 93

6.2 Tumour region of interest selection 95

6.3 Statistical analysis 96

6.4 Results 96

6.4.1 A marginal infiltration of mouse model 96

6.4.2 PWI detects more extensive regions of tumour infiltration than clinic MRI 98

6.4.3 Relationship between perfusion and invasion in tumour margin 101

6.4.4 Perfusion variation as a marker of tumour cell infiltration 102

6.5 Discussion 104

6.6 Limitations 107

6.7 Conclusion 107

Chapter 7: Investigating how to optimally combine multiparametric MRI data to detect GB infiltration

7.1 Introduction 109
7.2 Regression analysis models 112
7.3 MRI pre-processing 113
7.4 Statistical analysis 115
7.5 Results 116
7.5.1 Visual analysis 118
7.5.2 Pearson correlation 118
7.5.3 Volumetric analysis of tumour 119
7.5.4 Probability density function analysis 121
7.6 Discussion 123
7.7 Conclusion 125
7.8 Future directions 125

Chapter 8: General conclusion

8.1 Discussion 127
8.1.1 Limatations 131
8.2 Conclusion 131
8.3 Future directions 133
Appendix A Published peer reviewed articles during PhD study 135
9.1 References 157

List of Figures

Figure 1.1 : Invasion of tumour cells into normal brain tissue. 5

Figure 1.2**:** Shows the difference in spatial resolution between CT andMRI of mouse. 6

Figure 1.3**:** The theoretical distribution of tumour cell density extended beyond area detected by T2W and CE-T1. 7

Figure 1.4: Shows the surgical location of small glioblastoma before and after exogenous 5-ALA dye. 8

Figure 1.5: Three types of radiation therapy target volume GTV ,CTV and PTV. 9

Figure 1.6: Glioblastoma tumour cells derived from human biopsies injected within the mouse brain's healthy tissue. 10

Figure 2.1: The magnetic field causes the nucleus to precess at the Larmor frequency. 14

Figure 2.2 Spin align with and without external magnetic field present. 15

Figure 2.3: Schematic diagram showing the separation of energy levels with and without an external magnetic field. 15

Figure 2.4: Schematic diagram showing the net magnetisation parallel to the external magnetic field during a 90° pulseand dephase. 17

Figure 2.5: T1 recovery and T2 decay curves. 18

Figure 2.6: A T2* signal decay after an RF pulse. 19

Figure 2.7: Gradient (Gz) as a linear function of main magnetic field. 20

Figure 2.8: Shows principles of slice selection. 21

Figure 2.9: *In vivo* brain MR images acquired in (A) Axial (B) Sagittal (C) Coronal. 22

Figure 2.10: Time diagram of basic gradient-echo sequence. 23

Figure 2.11: Time diagram of basic spin-echo imaging sequence. 24

Figure 2.12: k-space diagram. 26

Figure 2.13: The major parts of an MR scanner and electrical components. 28

Figure 2.14: Example of T1W image of mouse brain. 29

Figure 2.15: Example of T2W image of mouse brain. 30

Figure 2.16: Free diffusion particle moving from two points. 31

Figure 2.17: The Stejskal-Tanner diffusion sequence. 31

Figure 2.18: Mono-exponential of diffusion signal decay of water in MR. 33

Figure 2.19: Illustration of isotropic and anisotropic diffusion. 34

Figure 2.20: Represented eigenvalues of isotropic and anisotropic diffusion. 35

Figure 2.21: Example of DWI with a malignant brain tumour in mouse. 36

Figure 2.22: Example of ADC map of brain tumour in mouse. 36

Figure 2.23: Example of FA image of brain tumour in mouse. 37

Figure 2.24: Illustration of blood-brain barrier components. 37

Figure 2.25: Difference of flow between normal and abnormal tissue. 39

Figure 2.26: Injection of contrast agent (Gd) in mouse-tail. 40

Figure 2.27: Shows T1W brain image pre and post injection ,and subtraction after injection of Gd contrast. 40

Figure 2.28: Illustration describing the principles of freely diffusible tracer theory. 42

Figure 2.29: Illustration of perfusion imaging, showing the control and label slices positioned on a mouse head and subtraction result between them. 43

Figure 2.30: (A) Pulse sequence (mbASL), (B) The location of the label and control slices. 44

Figure 2.31: Example of perfusion weighted image using mbASL. 44

Figure 3.1: (A) Phantom image with vertical profile line. (B) Representing pixels' intensity along line in (A). 48

Figure 3.2: DWI before and after removing sensitivity of surface coil. 49

Figure 3.3: T2W brain image before and after skull stripping. 50

Figure 3.4: Applying anisotropic diffusion filter. 52

Figure 3.5: Applying Gaussian Mixture Model on mouse brain. 55

Figure 3.6: Linear, rigid ,rotation and affine transformation models. 56

Figure 3.7: Comparison 2D histograms with and without rotation. 57

Figure 3.8: Block diagram of the histology process. 59

Figure 3.9: Example of H&E stains imaging. 59

Figure 3.10: Example of HLA stains imaging. 60

Figure 3.11: Visual assessment using checkerboard after co-registration of MRI with histology images. 61

Figure 3.12: The interaction of two regions A and B. 62

Figure 3.13: Diagram of comparison of two regions true positive (TP), true negative (TN), false positive (FP) and false negative (FN) regions. 63

Figure 4.1: Tumour margin samples of brains stained for H&E and HLA. Regions of vascular cuffing by invading tumour cells are enlarged. 66

Figure 4.2: Experimental protocol of first study. 67

Figure 4.3: Experimental protocol of second study. 67

Figure 4.4: MRI Biospect 7T scanner and equipment used in the experiment. 68

Figure 4.5 : Example of MR images of first experiment in week12. 70

Figure 4.6: Example of MR images of second experiment weeks 15 and 17. 71

Figure 5.1: Effect of cutting angle (φ) on MRI and histology with comparison of slice thickness. 78

Figure 5.2: The cutting of histology sections were guided by 0.5 mm thick $T2W_{Histology}$ with slice thickness comparsion. 78

Figure 5.3: Simplified diagram of the image processing pipeline leading to the production of 3D matrices after combining MRI modalities and SIH data. 79

Figure 5.4: Co-register of three HLA sections to construct at SIH map and 3D matrix. 81

Figure 5.5: Examples of histology sections for both HLA and H&E stains and tumour volume error comparison between sections. 83

Figure 5.6: SIH maps generated using several sections of HLA with tumour volume comparison. ROC analysis to evaluate the ability of 5 sections SIH maps to probe the tumour volume. 85

Figure 5.7: Example of non-rigid co-registration of histology with T2W MRI and Checkerboard validation. 86

Figure 5.8: Volumetric analysis for T2W five individual histology sections and SIH. 88

Figure 5.9: Power calculation between SIH and T2W for two different single slice groups (A) section SSH1 (B) section SSH2. 89

Figure 5.10: Scatter plots between T2W, ADC MRI modalities and histology. 90

Figure 6.1: T2W and CE-T1 (pre and post injection) at week 12 with Ki67 immunohistochemistry on slices. 97

Figure 6.2: T2W images at different times after injection of G7 tumour cells illustrating normal tumour growth and animal weight. 97

Figure 6.3: (A) Example of manual selection of ROIs in week 9 and week 12. (B)Tumour volumes with different MRI modalites (C) Tumour volume comparsion between MRI modalites and SIH. 99

Figure 6.4: (A) Dice score, (B) Accuracy index (C), Sensitivity index and (D) specificity index compasion between different MRI modalites. 100

Figure 6.5: (A) Fluorescence microscopy images probing HLA and dextran 70kDa. (B) MRI (T2, ADC, PWI) and fluorescent microscope images (HLA, dextran) from a mouse at 12 weeks. 102

Figure 6.6: Images and scatter plots of PWI signal against SIH for each voxel Core, and margin region box plots comparison. 104

Figure 7.1: Reconstruction of a single tumour map from different MRI modalities. 110

Figure 7.2: Schematic showing the voxel by voxel analysis method used to generate a single tumour map. 111

Figure 7.3: Examples of Linear regression, Quadratic regression, and Cubic regression fitting. 113

Figure 7.4: Image processing pipeline to create regression maps. 114

Figure 7.5: Comparison of original MR images in different regression maps. 118

Figure 7.6: Pearson correlation comparison between regression maps and SIH. 119

Figure 7.7: Volumetric analysis of tumour between QRM and CRM regression maps and SIH map. 120

Figure 7.8: Comparison of volumetric analysis between multiple regression maps and SIH 120

Figure 7.9: Comparison of volumetric analysis between QRM, CRM and SIH. 121

Figure 7.10: Comparison of normalised probability density function (PDF) between CRM and SIH for whole brain. 122

Figure 7.11: Comparison between QRM, CRM and SIH. 123

List of Tables

Table 7.1: The multi-regression coefficients (bi) of IRM, QRM and CRM. 117

Dedication

This work is dedicated to my beloved family

My parents: Mom and Dad

My brother Akeel

My wife

And for my three lovely sons

Acknowledgements

Throughout my studies I received a tremendous amount of support from multiple people. I would like to take this opportunity to thank them for helping me to achieve my PhD.

First, I give thanks to Allah for helping me and giving me the knowledge, patience, and strength to successfully complete this PhD. I would like to acknowledge the advice and guidance of my advisors, Dr. William Holmes and Dr. Antione Vallatos. They have been more than mentors in guiding me throughout my entire time in the in INP/MVLS at University of Glasgow and have played a pivotal role in this project. They were always there to offer help and support and were understating of the problems that arose throughout my writing. They provided the required background and experiential knowledge for the work. Also, I would like to thank Dr. Jozien Goense, Dr. John Foster, Dr. Joanna Birch, and Giacinta Frisillo for their help and feedback.

I am sincerely thankful for the support of my family members, without whom I wouldn't have been able to finish my thesis. No words can express my gratitude and thanks to my wife for caring for my family while I was busy with my studies, and for her patience and endless support and sacrifices. Also, I would like to thank and appreciate my sponsor, The Ministry of Higher Education and Scientific Research in Iraq, for their administrative and financial support.

Finally, I would like to thank my colleagues, Abdulrahman, Mohammed and Samantha for their encouragement and support. In addition, I would like to thank all the staff of INP/MVLs, Lindsay, James, Linda, and Conor for providing me with essential information about the thesis that helped a lot in planning and pacing my work.

Declaration

I declare that this thesis contains the result of my own work and has not been submitted for any other degree at the University of Glasgow or any other institution.

Haitham AL-Mubarak

Abbreviations

^{1}H	Hydrogen atoms
3D	Three dimensional
5-ALA	5-Amiinolevulinic acid
A	Cross-section area
ADC	Apparent Diffusion Coefficient
ASL	Arterial Spin Labelling
b	Magnitude of diffusion encoding gradients
B_1	RF magnetic field
BBB	Blood-Brain Barrier
B_0	The main magnetic field-7 Tesla
B_{local}	Local magnetization
C	Curie
CA	Contrast Agent
CAD	Computer Aided Diagnosis
CBF	Cerebral Blood Flow
CBV	Cerebral Blood Volume
CE-T1	Contrast Enhanced T1
cMRI	Clinic MRI
CNS	Central Nervous System
CRM	Cubic Regression Map
CSF	Cerebrospinal Fluid
CT	Computed Tomography
CTV	Clinical Target Volume
CV	Coefficient of Variation
D	Diffusion coefficient
DC	Direct Current
DCE	Dynamic Contrast-Enhanced
Dice	Dice Similarity Coefficient
DICOM	Digital Imaging and Communication in Medicine
DSC	Dynamic Susceptibility Contrast
DTI	Diffusion Tensor Imaging
DWI	Diffusion Weighted Imaging
EM	Expectation Maximization
EPI	Echo Planner Imaging
f	Frequency
FA	Fractional Anisotropy
FCM	Fuzzy C-Means
FID	Free Induction Decay
FITC-dextran	Fluorescein Isothiocyanate–dextran
FLAIR	Fluid Attenuated Inversion Recovery
FN	False Negative
FOV	Field Of View
FP	False Positive
G	Gradient amplitude
Gd-DTPA	Gadolinium-Diethylene Triamine Penta-Acetic
GB	Glioblastoma
Gd	Gadolinium
GE	Gradient Echo
GM	Grey Matter
GMM	Gaussian Mixture Model

GTV	Gross Tumour Volume
G_x	X-gradient
G_y	Y-gradient
G_z	Z-gradient
H	Entropy
h	Planck's constant
H&E	Haematoxylin and Eosin
HLA	Human Leukocyte Antigen
I	Spin quantum number
ICP	Intracranial Pressure
IRM	Interaction Regression Map
k_B	Boltzmann constant
k	k-space
K_x	Frequency encoded
K_y	Phase encoded
m	Mean value
LRM	Linear Regression Map
mbASL	Multiple Boli Arterial Spin Labelling
mpMRI	Multiple parametric MRI
$M_{control}$	Control Image
MD	Mean Diffusivity
MI	Mutual Information
m_I	Spin quantum number
M_{label}	Labelled Image
M_{post}	Image post injection with Gd
M_{pre}	Image pre injection with Gd
M_0	Net equilibrium magnetisation
MRA	Magnetic Resonance Angiograph
MRI	Magnetic Resonance Imaging
MTT	Mean Transit Time
MSME	Multi Slice Multi Echo
M_{xy}	Transvers component of the net magnetisation
NC3RS	UK government policy of Replacement, Refinement and Reduction
M_z	Longitudinal component of the net magnetisation
N_{down}	Number of spins in lower energy level
NMR	Nuclear Magnetic Resonance
N_{up}	Number of spins in upper energy level
PBS	Phospate Buffered Sline
PET	Positron Emission Tomography
PTV	Planning Target Volume
PWI	Perfusion Weighted Imaging
QRM	Quadratic Regression Map
RARE	Rapid Acquisition with Relaxation Enhancement
RF	Radio Frequency
RGB	Red, Green and Blue
ROC	Receiver Operating Characteristic
ROI	Region Of Interest
S	Signal
SE	Spin Echo
SIH	Stacked In-plane Histology
SNR	Signal to Noise Ratio
SOC	Standard Of Care

SPECT	Single-Photo Emission Computed Tomography
SSH	Single Section of Histology
STD	Standard Deviation
t	Time
T	Temperature
T1	Longitudinal relaxation time
T1W	T1Weighted
T2	Transvers relaxation time
$T2^*$	Effective T2 relaxation time
T2W	T2Weighted
TE	Echo Time
TI	Inversion Time
TM	Transformation Model
TMZ	Temozolomide
TN	True Negative
t_p	Period of time
TP	True Positive
TR	Repetition Time
US	Ultrasound
VEGF	Vascular Endothelial Growth Factor
V_{max}	Maximum Tumour Volume
V_{min}	Minimum Tumour Volume
VOI	Volume Of Interest
$\boldsymbol{\omega_0}$	Larmor frequency
WHO	World Health Organisation
WM	White Matter
Δ	Observation time
ΔE	Energy difference
δ	Duration of the gradient pulse
λ	Parallel diffusivity
λ_1, λ_2, λ_3	The first, second and third eigenvalues of diffusion tensor
μ	Magnetic moment
Σi	Covariance matrix
γ	Gyromagnetic ratio

Peer Reviewed Publication Resulting from This Thesis (see appendix A)

- Stacked in-plane histology for quantitative validation of non-invasive imaging biomarkers: application to an infiltrative brain tumour model.

H.Al-Mubarak; L. Gallagher; W. M. Holmes; A. Vallatos; J. L. Birch; L. Gilmour; A. J. Chalmers; J. E. Foster, Journal of Neuroscience Methods,(2019), Vol: 326, Page: 108372, Doi: 10.1016/j.jneumeth.2019.108372

- Quantitative histopathologic assessment of perfusion MRI as a marker of glioblastoma cell infiltration in and beyond the peritumoral oedema region.

A.Vallatos, A., **Al-Mubarak, H. F. I.**, Birch, J. L., Gallagher, L., Mullin, J. M., Gilmour, L., Holmes, W. M., Chalmers, A. J., (2018), J Magn Reson Imaging: 1-12, Doi: 10.1002/jmri.26580.

- Changes an apparent diffusion coefficient across the macroscopic tumour margin correlate with novel tissue measures of infiltration in a preclinical glioblastoma Model (Conference abstract).

Thompson G., Vallatos A., Birch J., **Al-Mubarak H.,** Gallagher L., Gilmour L., Waldman A., Holmes W., and Chalmers A., Neuro Oncol, 2018, 20: i15., Doi: 10.1093/neuonc/nox238.066.

Award Prize

- National 3R's Prize 2018 by the Animal Welfare and Ethical Review Board (AWERB),UK.

Selected Conference Proceedings

- **Annual conference CRUK-EPSRC 'Heterogeneity' held by Cancer Imaging Centres, 2016, Manchester, UK.**
  The Quantitative Assessment of Glioblastoma MRI Data by Multi-spectral Analysis, Poster, 1.
  H. Al-Mubarak, A. Vallatos, J.E. Foster, A.J. Chalmers, W.M. Holmes.

- **The Sanono-Sinapse Meeting, 29th September 2016, Dundee, UK.**
  Optimising small animal MRI to measure invasion and tumour heterogeneity in glioblastoma xenografts, Poster.
  A. Vallatos, H. Al-Mubarak, L. Gallagher, J.L. Birch, L. Gilmour, J.E. Foster, A.J. Chalmers, W.M. Holmes.

- **British Neuro-Oncology Society Annual Conference, 21-23 June 2017, Edinburgh, UK.**
  1- Probing glioblastoma infiltration into healthy tissue by magnetic resonance perfusion imaging: a quantitative MRI evaluation, oral presentation, session OS-22F.
  A. Vallatos, J.L. Birch, H. Al-Mubarak, L. Gallagher, L. Gilmour, J.E. Foster, A.J. Chalmers, W.M. Holmes.
  2- Changes in Apparent Diffusion Coefficient across the Macroscopic Tumour Margin Correlate with Novel Tissue Measures of Infiltration in a Preclinical Glioblastoma Model, Abstract. Neuro-Oncology, Volume 20, Issue suppl_1, 1 January 2018, Page i15, https://doi.org/10.1093/neuonc/nox238.066.
  Gerard Thompson, Antoine Vallatos, Joanna Birch, Haitham Al-Mubarak, Lindsay Gallagher, Lesley Gilmour, Adam Waldman, William Holmes, Anthony Chalmers.
  3- BBB permeability as a magnetic resonance imaging biomarker for low glioblastoma infiltration, Abstract, Neuro-Oncology, Volume 20, Issue suppl_1, 1 January 2018, Page i25 , https://doi.org/10.1093/neuonc/nox238.115.
  Antoine Vallatos, Joanna Birch, Haitham Al-Mubarak, Lindsay Gallagher, Lesley Gilmour, Anthony Chalmers, William Holmes.

- **25th Annual ISMRM Meeting and Exhibition, 22-27 April 2017, Haonolulu, USA.**
  Multi-parametric MRI of glioblastoma invasion quantitative evaluation using histological stacks, Poster, 2929.
  H. Al-Mubarak, A. Vallatos, L. Gallagher, J.L. Birch, L. Gilmour, J.E. Foster, A.J. Chalmers, W.M. Holmes.

- **ESMRMB Magnetic Resonance Materials in Physics, Biology and Medicine, Congress, October 19 – 21, 2017, Barcelona, Spain.**
  Detecting of Glioblastoma Invasion Cells Using Multi-parametric MRI and Quantitative Assessment with in-plane Histology, Oral presentation, 325.
  H. Al-Mubarak, A. Vallatos, J. Birch, L. Glmour, L. Gallagher, J. Mullin, A. Chalmers, W. Holemes.

- **Annual ISMRM–ESMRMB Meeting, 16-21 June 2018, Paris, France.**
  1- Detecting glioblastoma invasion using multi-parametric MRI and quantitative assessment with in plane histology,e-poster, 3831.
  H. Al-Mubarak, A. Vallatos, L. Gallagher, J.L. Birch, L. Gilmour, J.E. Foster, A.J. Chalmers, W.M. Holmes.

  2- Perfusion MRI as a marker of glioblastoma infiltration into health tissue, e-poster, 6026.
  A. Vallatos, H. Al-Mubarak, L. Gallagher, J.L. Birch, L. Gilmour, J.E. Foster, A.J. Chalmers, W.M. Holmes.

  3- Apparent diffusion coefficient correlates with histological tumour burden at infiltrating margins of a pre-clinical glioblastoma model, e-poster, 6526.
  Gerard Thompson, Antoine Vallatos, Joanna Birch, Haitham Al-Mubarak, Lindsay Gallagher, Lesley Gilmour, Adam Waldman, William Holmes, Anthony Chalmers.

  4-Quantitative Assessment of MRI Biomarkers Using Non-Rigid Registration of Stacked in-Plane Histology: Application in a Mouse G7 Tumour Model,e-poster, 4858.
  H. Al-Mubarak, A. Vallatos, L. Gallagher, J.L. Birch, L. Gilmour, J.E. Foster, A.J. Chalmers, W.M. Holmes.

- **The Sinapse Annual Scientific Meeting, 25 June 2018, Edinburgh, UK.**
  1- Stacked in plane histology for quantitative MRI assessment: Application to an infiltrative brain tumour model, oral presentation, O6.
  H. Al-Mubarak, A. Vallatos, L. Gallagher, J.L. Birch, L. Gilmour, J.E. Foster, A.J. Chalmers, W.M. Holmes.

  2- Perfusion as a marker of brain tumour infiltration into healthy brain tissue: a quantitative MRI evaluation, oral presentation, O13.
  H. Al-Mubarak, A. Vallatos, L. Gallagher, J.L. Birch, L. Gilmour, A.J. Chalmers, W.M. Holmes.

- **24th Annual ISMRM Scientific Meeting of the British Chapter, 24-26 September 2018, Oxford, UK.**
  1- Investigating How to Optimally Combine Multimodal MRI Data to Better Identify Glioblastoma Infiltration, oral presentation, O16.
  H. Al-Mubarak, A. Vallatos, L. Gallagher, J.L. Birch, L. Gilmour, J.E. Foster, A.J. Chalmers, W.M. Holmes.

  2- Stacked In-plane Histology for Quantitative Assessment of MRI Markers: Application to an Infiltrative Brain Tumour Model, Power pitch, PP24.
  H. Al-Mubarak, A. Vallatos, L. Gallagher, J.L. Birch, L. Gilmour, J.E. Foster, A.J. Chalmers, W.M. Holmes.

- **27th Annual ISMRM Meeting and Exhibition, 11-16 May 2019, Montreal, Canada.**

  1- Investigating How to Optimally Combine Multimodal MRI Data to Better Identify Glioblastoma Infiltration, e-poster, 2354.

  H. Al-Mubarak, A. Vallatos, L. Gallagher, J.L. Birch, L. Gilmour, J.E. Foster, A.J. Chalmers, W.M. Holmes.

  2- Stacked In-plane Histology for Quantitative Validation of Non-invasive Imaging Biomarkers: Application to an Infiltrative Brain Tumour Model, e-poster, 2390.

  H. Al-Mubarak, A. Vallatos, L. Gallagher, J.L. Birch, L. Gilmour, J.E. Foster, A.J. Chalmers, W.M. Holmes.

Chapter 1

General Introduction to Imaging and Treatment of Brain Tumours

1.1 Background to cancer

A tumour begins when cells in the body start to proliferate out of control. The absence of the normal rules of cell division and death may lead to alterations in normal cellular function and threaten life (Hejmadi, 2013). A tumour may originate due to external issues such as chemical carcinogens, pollution, radiation and so on, which can cause gene modifications resulting in unlimited growth (Yankeelov et al., 2012).

Tumours can be categorized by their cell type of origin and degree of aggressiveness. Benign tumours grow very slowly, have distinct borders, seldom infiltrate into the surrounding tissue, and can usually be completely removed by surgery and without recurrence (Louis et al., 2016). Malignant tumours on the other hand, grow rapidly, are difficult to remove completely by surgery and infiltrate to the surrounding normal tissues or metastasis (Hejmadi, 2013).

1.2 The brain anatomy

The brain is the most complex organ in the human body and is part of the Central Nervous System (CNS). It is surrounded by the skull and consists of Grey Matter (GM), White Matter (WM) and Cerebrospinal Fluid (CSF). GM consists of neural cell bodies, neuropil, glial cells, synapses, and capillaries (Mescher, 2016). WM contains myelinated axons. CSF is a clear fluid which exists in the ventricles and surrounds the brain and spinal cord.

1.3 Brain tumours

There are several types of brain tumours, such as glioblastoma, astrocytoma, pituitary adenoma, acoustic neuroma, meningioma, oligodendroglioma, haemangioblastoma, CNS lymphoma, and others (Hattingen and Pilatus, 2016, Mescher, 2016). Brain tumours can be classified into two categories: primary and secondary. Primary brain tumours arise from the cells inside the brain. Secondary brain tumours are the result of metastases. This occurs when tumour cells separate from a primary tumour site and migrate to the brain through the blood system or the lymphatic system (Cuddapah et al., 2014, Weinberg, 2007).

1.4 Glioma

Gliomas are the most common form of malignant primary brain tumours and arise *de novo* from glial cells and their progenitors in the brain. Until recently, glioma tumour cell classification was based on microscopic examination of tumour specimens by neuropathologists. However, since 2016, the World Health Organization (WHO) has classified tumours of the Central Nervous System (CNS) by integrating both classical histology features (morphological appearance) and molecular biomarkers that are based on the specific group's molecular and gene expression profile (Louis et al., 2016).

Gliomas have a variety of grades and degrees of aggressiveness that can be divided into low-grade benign gliomas (grade I and II) or high-grade malignant gliomas (grade III or IV).

Grade I tumours are different from the three other grades. Typically, tumour cells are relatively unchanged compared to normal cells, and proliferate very slowly and rarely infiltrate into the surrounding tissue. Complete surgical resection can usually be achieved due to the distinct borders between a normal brain and tumour tissue (Louis et al., 2016).

Grade II tumour cells do not look like normal cells. The tumour grows slowly and often progress into a higher-grade tumour despite therapy. Studies show that the tumours return in the form of highly invasive tumours (grade IV) 5 to 10 years after the original diagnosis and subsequent treatments (Bogdanska et al., 2017).

Grade III (Higher malignant) tumours are invasive tumours that share common characteristics with grade IV tumours. The tumour cells invade healthy neighbouring brain tissue and after this are more likely to become rapidly dividing cells, but the tumours contain no dead cells at their centre (necrotic). The tumour tends to recur after surgery (Lacroix et al., 2001).

Grade IV is a glioblastoma, which is a very aggressive tumour; they are heterogeneous, grow very fast, build new blood vessels, contain dead cells (necrosis) in the centre, and complete surgical resection is not achievable (De vleeschouwer, 2017).

1.5 Glioblastoma

Glioblastoma (GB) is a fatal and aggressive form of primary brain tumour. WHO classified this brain tumour as a grade IV (De vleeschouwer, 2017). GB generally develops *de novo*, meaning these tumours can develop spontaneously within the brain and do not arise from the migration of cells from another tumour found within the body (Ray, 2010). The median survival for patients with glioblastoma is approximately one and a half years (Bernas et al., 2007). Despite recent advances in radiotherapy, chemotherapy, surgical techniques, and newer drugs, there has been little improvement in patient survival.

One of the hallmarks of high-grade glioma is the ability of a single tumour cell or small groups to infiltrate adjacent normal tissue (Krakhmal et al., 2015). The invasion of tumour cells can occur in several ways (Fig.1.1), i.e., through the parenchyma (dashed green square), along vasculature (dashed blue square), via white matter tracts (dashed purple rectangle), or in the leptomeningeal space, dashed red rectangle (de Gooijer et al., 2018, Zagzag et al., 2008). The leptomeningeal space is the space between the arachnoid membrane and pia mater that is filled with cerebrospinal fluid and contains the large blood vessels that supply the brain. In fact, glioma cells are locally invasive and very rarely metastasise.

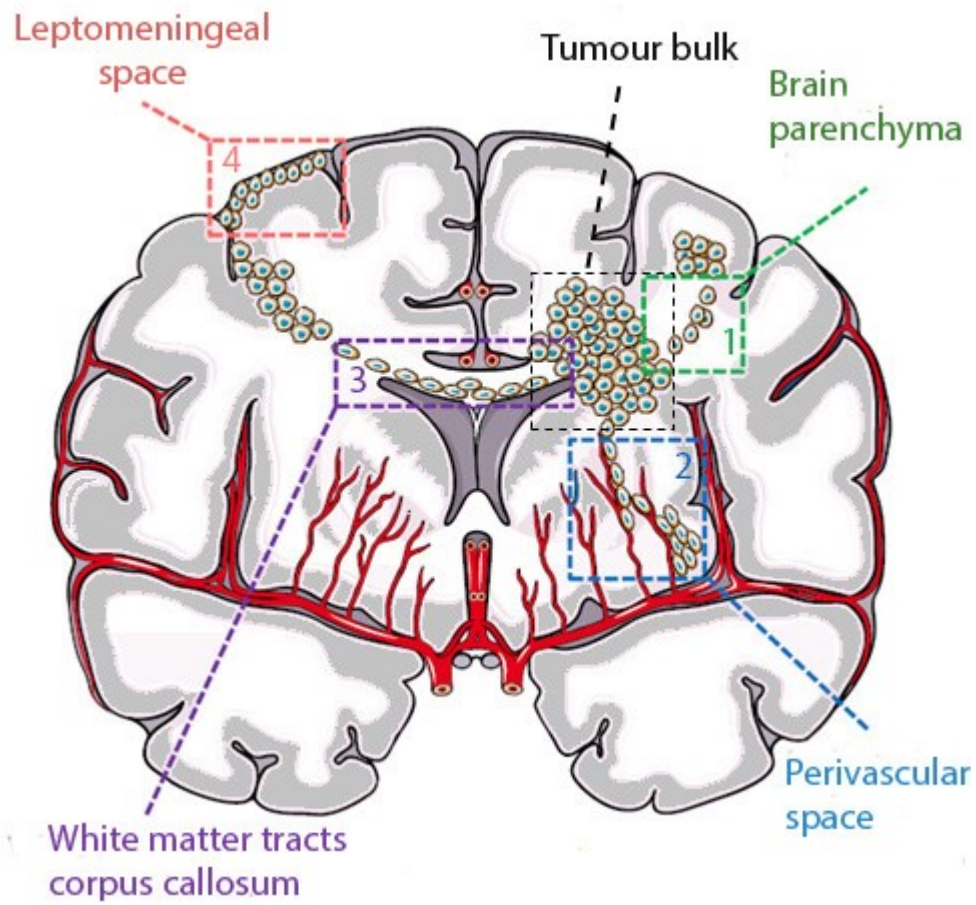

Figure 1.1: Invasion of tumour cells in to normal brain tissue. Four different routes of invasion have been described: (1) via the brain parenchyma, (2) perivascular space, (3) white matter tracts, and (4) leptomeningeal space. Adapted from (de Gooijer et al., 2018).

The primary routes of invasion by glioma cells are by migrating through the perivascular space surrounding blood vessels or along white matter tracts. Claes et al. (2007) reported that high-grade glioma cells usually use the same routes of migration that are travelled by immature neurons. The invasion of tumour cells mostly happens along white matter fibers and extend to corpus callosum into the contralateral hemisphere.

1.6 Medical imaging of GB

There are several techniques to evaluate tumour progression, diagnosis, and monitoring of GB. The standard imaging techniques used to diagnose and monitor brain tumours are X-ray Computed Tomography (CT) and Magnetic Resonance Imaging (MRI). Other techniques have been used such as Positron Emission Tomography (PET), and Single-Photon Emission Computed Tomography, SPECT,(De vleeschouwer, 2017).

In the clinic, CT images are widely used for diagnostic and therapeutic purposes in various medical disciplines. However, high doses of X-ray radiation can damage the normal tissues and image contrast is poor when looking at soft tissues. In contrast, MR images provide an excellent contrast between various forms of soft tissues which makes it very useful in tumour diagnosis (Fig.1.2).

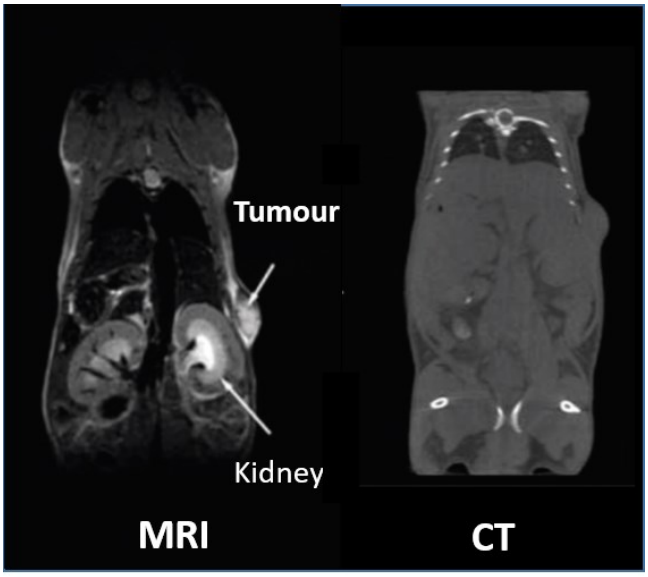

Figure 1.2: Shows the difference in spatial resolution between CT and MRI in mouse. MRI is superior in regards to the detail of the image and the tumour can be clearly seen. Image from (Karellas and Thomadsen, 2016).

MR images are generally classified into two types, clinic and advanced imaging. Clinic MRI (cMRI) images are qualitative, whereas advanced MRI methods provide quantitative or semi-quantitative measurements. These are discussed in chapter 2.

The standard MRI sequences that are used to detect GB in the clinic are T2-Weighted, T1-Weighted, Contrast Enhanced T1 and Fluid-attenuated inversion recovery. These clinic MRI (cMRI) modalities are useful to discriminate between brain tumours and normal tissue, although they are not able to detect the infiltration of tumour cells into the normal tissue (Sternberg et al., 2014). Several studies show that cMRI cannot detect the invasion of tumour cells beyond oedema (Swanson et al., 2002, Baldock et al., 2013, Vallatos et al., 2018a). Clinic MR cannot detect the invasion of a low density of tumour cells because, the current limit for tumour cell detection by MRI is in range between 100-500 cells (Muja and Bulte, 2009, Heyn et al., 2005). For more details see Fig.1.3.

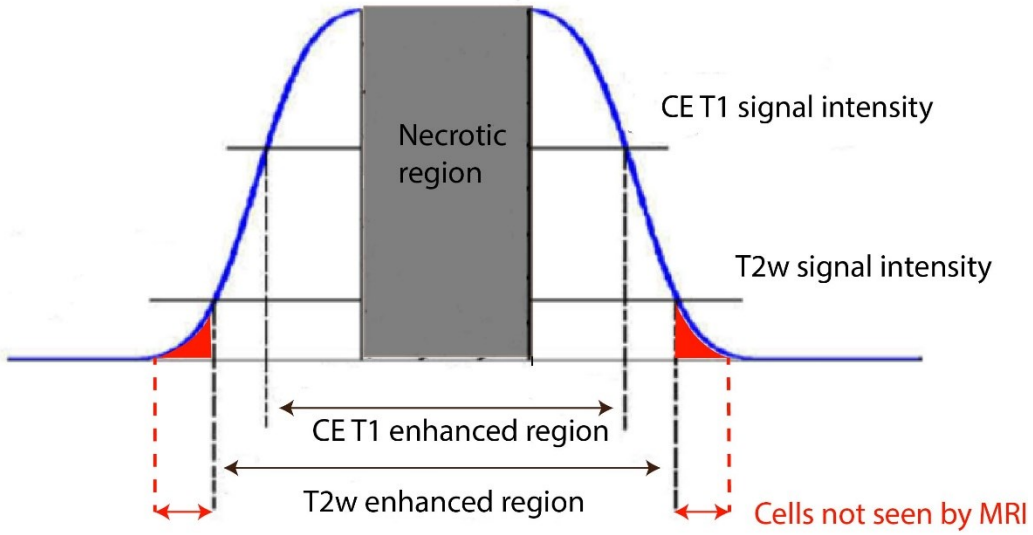

Figure 1.3: A theoretical distribution of tumour cell density represented by the smooth curve showing the tumour distribution extending beyond the region detected by T2W and beyond the region detected by CE-T1. Adapted from (Konukoglu et al., 2010).

1.7 Treatment of glioblastoma

The current Standard of Care (SOC) for glioblastoma treatment is maximal surgical resection followed by radiotherapy and chemotherapy with for example Temozolomide (Jain, 2018). However, since glioblastoma tumour cells can infiltrate several centimetres beyond the treatment volume defined by standard CT or MRI (Tracqui, 1995) this can lead to tumour recurrence and regrowth.

1.7.1 Surgery

Surgical resection is the first choice for the treatment of GB. However, this treatment routine almost always fails to remove the tumour completely due to the aggressive, heterogeneous and infiltrative nature of this type of tumour (Lacroix et al., 2001). Complete surgical removal is not always possible, as it is difficult to distinguish the tumour from normal tissue and sometimes the tumour's location is too near essential regions of the brain.

A significant development in oncology in recent years has been the use of fluorescence-guided surgery. The patient consumes a drink that enables surgeons during operation to target brain tumours accurately, by making cancer cells fluoresce pink. The liquid is called 5-Aminolevulinic Acid (5-ALA) that uses a fluorescent dye to make cancerous cells fluoresce under UV light (Fig.1.4 A,B).

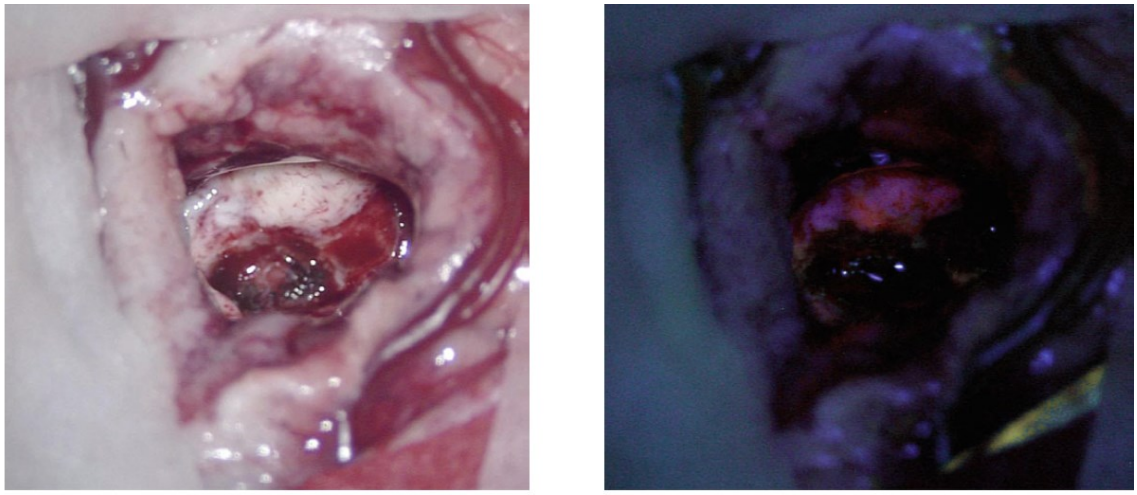

Figure 1.4: (A) Shows the surgical location of a small glioblastoma. (B) After drink of exogenous 5-ALA dye, the tumour cells become fluorescent under UV light. This feature can identify tumour cells clearly and facilitates resection. Adapted from (Hattingen and Pilatus, 2016).

1.7.2 Radiotherapy

Radiation therapy is an effective method to attack tumour cells. The radiation dose applied to the tumour is dependent on its location and the radio-sensitivity of the surrounding tissue. X-rays and gamma rays are routinely used in radiation therapy to treat various cancers. Their deposited energy can kill cancer cells or cause genetic changes resulting in cancer cell death (Baskar et al., 2012). The standard fractionated intensity X-rays in three-dimensional radiotherapy is in a total dose of 60Gy in 30 daily fractions, every weekday over a period of six weeks (Caranci et al., 2012).

In conventional radiation therapy three types of target volume are chosen to radiate. Firstly, the Gross Tumour Volume (GTV) is the lesion as identified in a magnetic resonance imaging scan with CE-T1 contrast. Secondly, the Clinical Target Volume (CTV) is defined as GTV plus an expansion margin of 2cm where there may be infiltration of tumour cells. Thirdly, the Planning Target Volume (PTV) is represented by CTV plus an expansion margin of 1cm (Burnet et al., 2004).

Figure 1.5 shows these three volumes. This additional margin results in a PTV, which may often be four or more times the volume of the original GTV. Figure 1.5 provides an illustration of how large PTV is compared to GTV. Hence, PTV usually incorporates a large number of critical brain regions and applying radiation to

these regions can result in irreversible damage. The conventional approach of adding a 2cm Euclidean margin to the GTV to construct a PTV is based on limited scientific evidence (Pirtoli and Gravina, 2016, Hattingen and Pilatus, 2016).

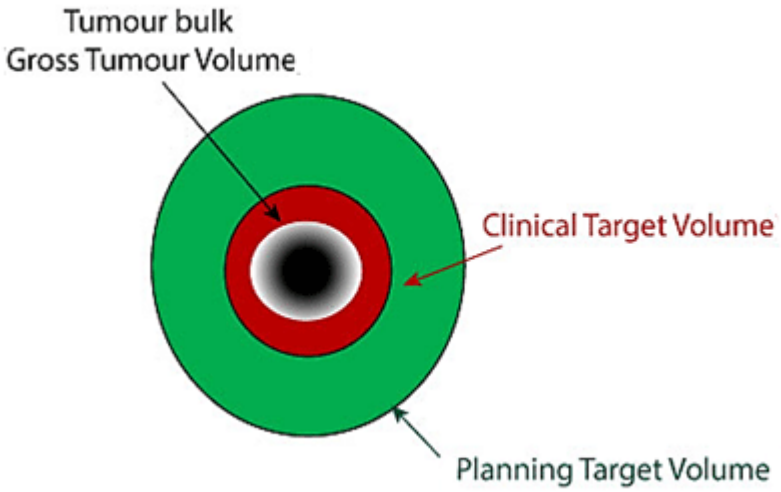

Figure 1.5: The three types of target volume are chosen to radiate the tumour: GTV in black representing tumour centre. CTV is together with a 2cm margin forms the GTV to be radiated. The PTV represents summation of areas GTV and CTV with additional 0.7cm margin. Adapted from (Burnet et al., 2004).

1.7.3 Chemotherapy

Chemotherapeutic agents work by targeting and killing tumour cells. There are many different types of chemotherapy medication, however, they all work in a similar way. The current drug for glioblastoma is Temozolomide (TMZ). TMZ is a DNA alkylating agent, which causes irreversible DNA damage and ultimately cell death.

Due to the lack of effective treatments available to cure glioblastoma patients, new therapies have been investigated such as anti-angiogenic gene therapy to reduce the rapid vascularization of GB (Gerstner and Batchelor, 2012), immunotherapy to increase patient survival , and hormone therapy to inhibit GB growth and to induce apoptotic pathways (Altiok et al., 2011).

1.8 Preclinical GB models

Preclinical animal models are useful to allow researchers to better understand tumour biology and develop new treatments. The choice of animal models is key to ensure that preclinical findings are relevant for human studies (Kiessling and Pichler, 2011). In this respect, a good animal model needs to reflect the biological properties of the patient. Animal models, such as rodents, are important tools in experiments (*in vivo or ex vivo*) because they are easy to handle, have a short lifespan, and have a central nervous system similar to that of humans.

There are currently many mouse GB cell lines that that can be used to recapitulate features of GB such as the G7, U251, U87, and GL261 that have been implanted into the brains of mice (Jacobs et al., 2011). Each glioma model may provide varying similarities to human GB, which can be used to test the effectiveness of novel chemotherapeutic combinations (Jacobs et al., 2011). However, there are two reasons why studying tumour cell invasion is difficult. First, there are few animal models that show an invasive growth pattern. Second, there is a deficiency of high-grade glioma staining for pathologic analysis (Inoue et al., 2012).

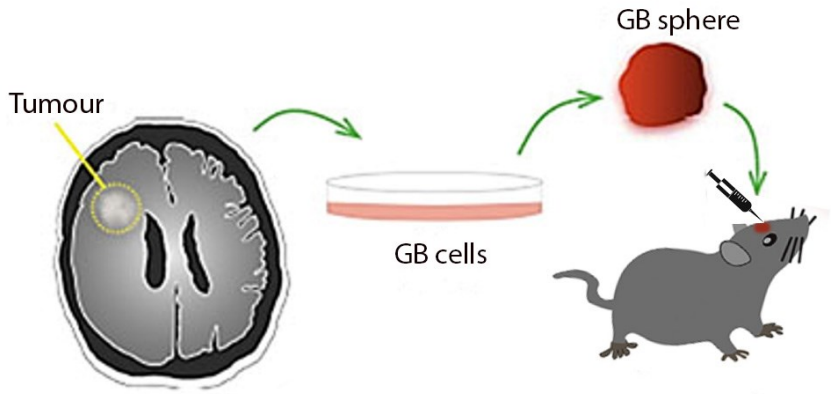

Figure 1.6: Glioblastoma tumour cells derived from human biopsies capture many characteristic of the tumour. Tumour cells are injected within the healthy mouse brain. Adapted from (Perrin et al., 2019).

This has recently improved with the use of the resected human G7 Glioblastoma cell lines, which were donated to the University of Glasgow by Dr. Colin Watts of the University of Cambridge, UK (Carruthers, 2015). This model is rich with stem cells which are resistant to radiotherapy and chemotherapy (Gomez-Roman et al.,

2017) and has a pathology resembling human disease, including an infiltrative margin which is useful to test new MRI techniques.

Chapter 2

The Theory of Magnetic Resonance Imaging

2.1 Background of MRI

Rabi et al. (1938) were the first to describe Nuclear Magnetic Resonance (NMR) as a method for determining nuclear magnetic moments. After the Second World War, Bloch (1946) observed the 'NMR' phenomenon, as an radio frequency signal response to irradiating magnetic nuclei in a magnetic field with continuous-wave Radio Frequency (RF) . Cope and Damadian (1970) were the first to use NMR to scan living things and observed that different types of tissue (e.g. normal tissue and cancerous tissue) have different signal relaxation properties. Following this discovery, many research groups started developing techniques and systems for imaging (Mansfield and Grannell, 1973, Lauterbur, 1973), leading to modern MRI.

In clinical practice, MRI has become a very common imaging tool, used for diagnosis, surgical planning, and follow-up of treatment outcomes. Compared with CT, MRI has superior soft-tissue contrast. MRI is also non-invasive and, unlike CT, does not use ionising radiation, thereby benefitting patient health. It is currently understood that exposure to the static magnetic field in MRI does not lead to harmful biological effects. MRI can be safely repeated to observe changes in pathology, such as the progression of a disease or the impact of treatment.

2.2 MRI principle

NMR signals are generally obtained from nuclei with an odd mass number (active MRI nuclei), such as ^{1}H, ^{13}C, ^{23}Na and ^{31}P (exceptions being ^{2}H and ^{14}N). These nuclei have a non-zero nuclear spin quantum number and a magnetic moment (μ). The interaction of the nuclei with the external magnetic field (B_0) causes the nuclear magnetic moments to align with and precess around the external magnetic field as shown in Fig.2.1.

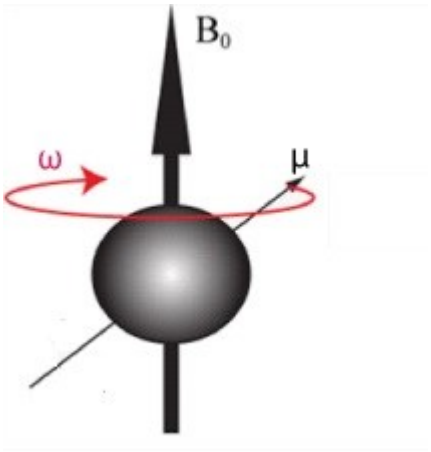

Figure 2.1: The external magnetic field causes the nucleus to precess at the Larmor frequency ω_0. The Larmor frequency of precession is related to the strength of the magnetic field, B_0.

The precession frequency is called the Larmor frequency ω_0, which is directly proportional to the strength of the magnetic field (B_0) and is written as follows:

$$\omega_0 = -\gamma B_0 \qquad \text{Equation 2.1}$$

Where γ is the gyromagnetic ratio, a constant specific to a particular nucleus (for protons, γ = 42.58 MHz/T), and B_0 the strength of the external magnetic field in Tesla.

Generally, medical magnetic resonance imaging uses the signal from the nuclei of hydrogen atoms (^{1}H) which contains a single proton. When no magnetic field is applied, the nuclear magnetic moments are oriented in random directions (Fig. 2.2A), and the net magnetisation (M_0) will be zero. However, by applying an external static magnetic field of B_0, the nuclei will align along the flux lines of the magnetic field (Fig.2.2B).

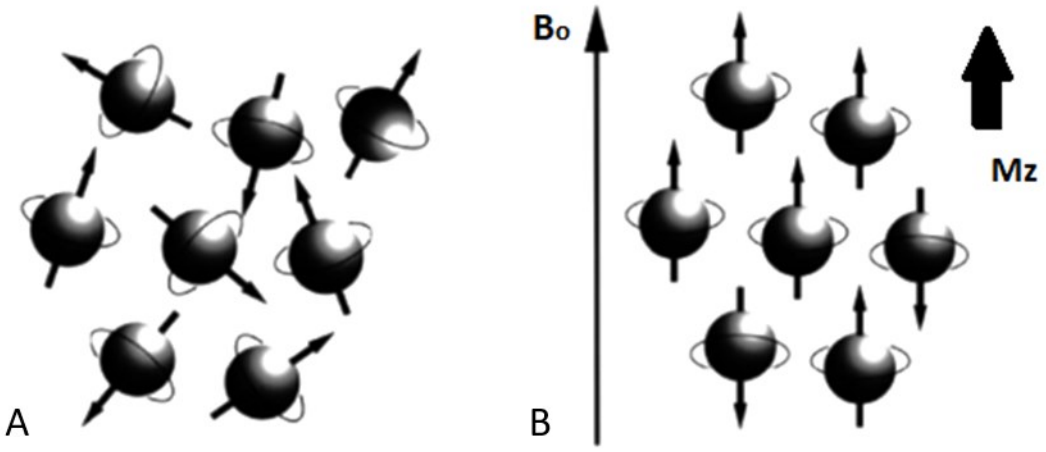

Figure 2.2 (A) With no external magnetic field present, spins rotate about their axes in a random direction. (B) In the presence of a magnetic field, slightly more spins align parallel to the main magnetic field, B, thus produce a net longitudinal magnetization, Mz. Note: diagram spins shown as perfectly aligned for convenience.

According to quantum mechanics, the number of possible orientations or energy states is determined by the nuclear spin quantum number, I. Hydrogen has a spin number of I= 1/2) and can adopt two possible spin states (2 I + 1). The low energy state (m_I = +1/2), where the nuclear spin vector is in the same direction as the static field, is called spin-up. The high-energy state (m_I = -1/2), where the nuclear spin vector is in the opposite direction, is called spin-down (Fig.2.3).

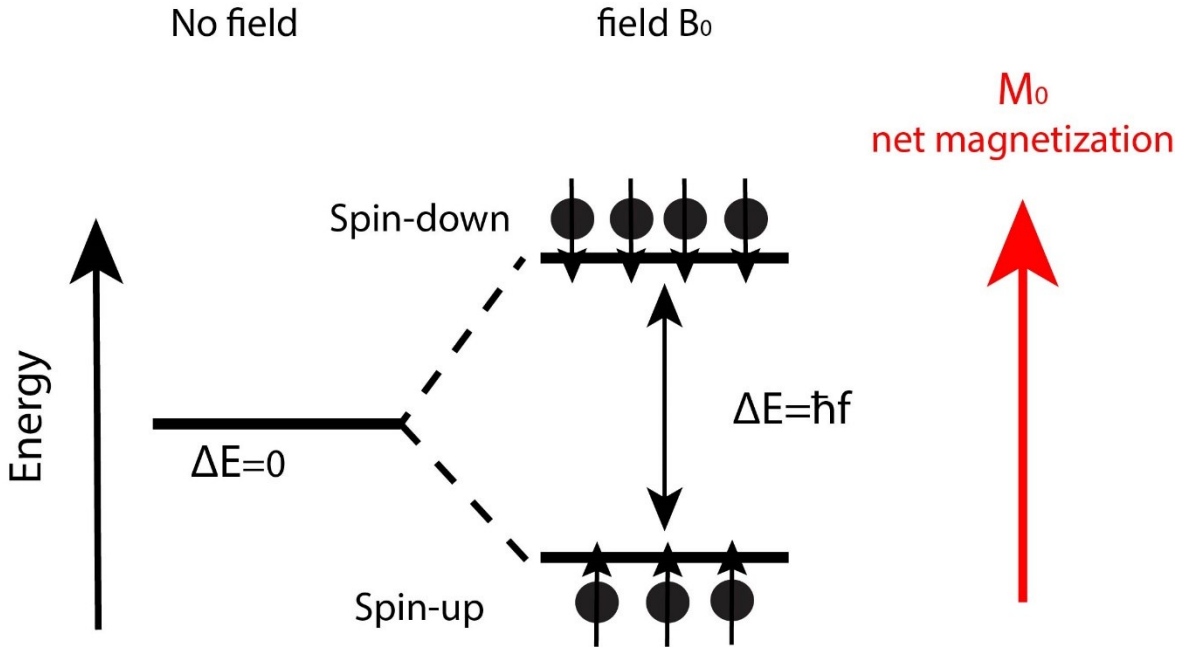

Figure 2.3: Schematic diagram showing the separation of energy levels of ^{1}H with and without of an external magnetic field (B_0).

The proportion of spins in the spin-up state (low energy) and spin-down (high-energy) state is determined by the Boltzmann distribution equation (2.2):

$$\frac{N_{down}}{N_{up}} = e^{\frac{-\Delta E}{k_B T}} \qquad \text{Equation 2.2}$$

Where N_{up} and N_{down} represent the number of spins in the upper and lower spin states, k_B is the Boltzmann constant ($1.38 \times 10^{-23} J/^oK$) and (T) is the temperature in Kelvin (^oK). The difference in energy between the lower energy state and higher energy state (ΔE) is equal to:

$$\Delta E = hf = \hbar\omega = \gamma\hbar B_0 \qquad \text{Equation 2.3}$$

Where h is Planck's constant which is equal to 6.62×10^{-34} m^2Kg/s and $\hbar = h/2\pi$. From this Curie's law of temperature-dependent paramagnetism can be derived:

$$M_0 = \frac{cB_0}{k_B T} \qquad \text{Equation 2.4}$$

Where C is the Curie constant and M_0 is the equilibrium net magnetisation.

2.2.1 Resonance

In physics, many systems are sensitive to the frequency of interactions, where the maximum energy transfer occurs at the resonance frequency. Excitation at this resonance frequency causes the system to enter an oscillating regime before returning to its initial state. NMR describes how protons aligned with the external magnetic field (B_0) can be excited when a Radio Frequency (RF) pulse ('excitation' pulse B_1), is applied at the same frequency as the precession frequency of the nuclei.

In the presence of an external magnetic field (B_0), the number of spin-up and spin-down nuclei are not equal. The net magnetization is called M_0. After applying the

RF pulse, the hydrogen nuclei absorb energy. This increases the number of high-energy (spin-down) nuclei (Fig.2.3) and creates phase coherence.

2.2.2 RF pulse

Magnetic resonance occurs when an RF pulse is applied at the same frequency as the Larmor frequency. For a group of nuclei, all the spins have the same phase after excitation by the RF pulse, resulting in a coherent transverse magnetization. In the presence of a receiver coil, the oscillating of the transverse magnetization induces an oscillating electric current in the receiver coil that can be measured. The dephasing due to the spins' interaction during relaxation causes a loss of coherence and a decrease of transverse magnetization (Fig.2.4A-C).

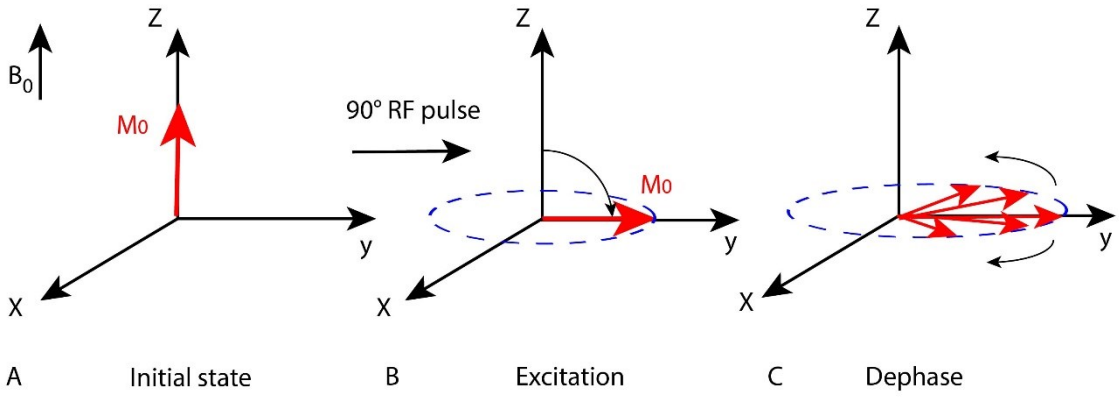

Figure 2.4: Schematic diagram showing (A) The equilibrium net magnetisation (M_0) parallel to the external magnetic field (B_0). (B) During the application of a 90° pulse, the M_0 moves from the z-axis to the xy-plane. (C) Spins lose coherence and dephase due to spin-spin relaxation.

2.3 Relaxation

Application of an RF pulse at the Larmor frequency will result in phase coherence and a net transverse magnetization (M_{xy}). The precessing transverse magnetization gives rise to the MR signal in the receiver coil. However, the MR signal quickly disappears due to two independent processes that return the net magnetization back to the equilibrium state (M_0). These two processes are spin-lattice relaxation (T1 relaxation) and spin-spin relaxation (T2 relaxation), respectively (Weishaupt et al., 2006, McRobbie et al., 2006). For more details see Fig.2.5A-B.

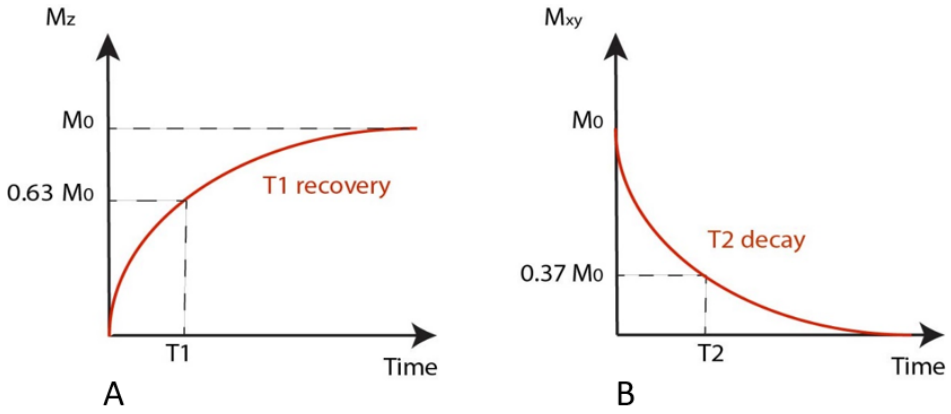

Figure 2.5: (A) T1 recovery curve which represents exponentially increasing longitudinal magnetisation. (B) T2 decay curve that represents the decay of magnetisation in the transverse plane (M_{xy}) after switching off the RF pulse.

2.3.1 T1 relaxation

Spin-lattice relaxation (T1) refers to the time taken for energised nuclei (following a 90^o pulse) to return to their equilibrium state. It is also known as the longitudinal relaxation time because, diagrammatically, it represents the time taken for the net magnetisation vector, M_0, to recover along the B_0 direction. The mechanism underlying T1 relaxation is a transfer of energy from the nuclear spins to their surrounding lattice atoms (Guy and ffytche, 2005). The nuclei in the lattice are subject to vibrational and rotational motions, which create a separate, fluctuating local magnetic field (B_{local}). This magnetic field can have frequency components matching the Larmor frequency of the nuclei, which can drive transitions between energy levels, returning the system to equilibrium. The recovery is exponential, with an exponential time constant termed T1, equation 2.5, Fig.2.5A. The relaxation time is defined as the time taken for 63% of the longitudinal magnetisation to recover. T1 depends on the inherent characteristics of the tissue and the magnetic field strength. The longitudinal relaxation of the net magnetization vector, M_z, parallel to the external magnetic field can be described by the equation:

$$M_z = M_0(1 - e^{\frac{-t}{T1}}) \qquad \text{Equation 2.5}$$

Where t is time, M_0 is the equilibrium net magnetization that depends on the proton density and the strength of the external magnetic field (section 2.2).

2.3.2 T2 relaxation

The z-component of the fluctuating local magnetic field B_{local}, will add to the static magnetic field B_0, causing the local Larmor frequency to be time varying. As individual spins experience a slightly different magnetic field, this results in dephasing and loss of transverse magnetisation (spin-spin relaxation). The decay is exponential, with an exponential time constant T2 (Fig.2.5B). T2 decay time is defined as the time taken for 63% of the transverse magnetisation to be lost. T2 also depends on the inherent characteristic of the tissue and the magnetic field strength and is usually faster than the corresponding T1 relaxation time. The transverse magnetization vector M_{xy} in the x-y plane can be described as:

$$M_{xy} = M_0 \, e^{\frac{-t}{T2}} \qquad \text{Equation 2.6}$$

2.3.3 T2 * relaxation

After an RF pulse is applied, the M_z is tilted into the x-y plane, producing a signal that is known as the Free Induction Decay (FID). The signal rapidly decays once the RF pulse is switched off due to parts per million level inhomogeneity in the static magnetic field, B_0 (Fig.2.6).

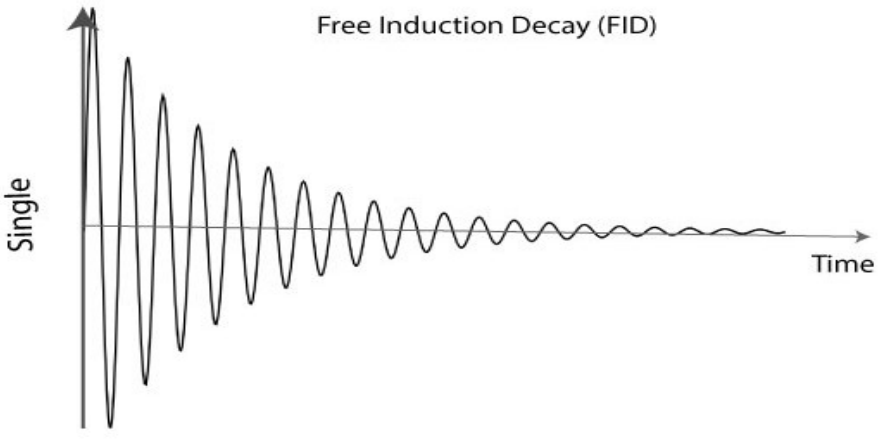

Figure 2.6: After an RF pulse, T2* signal in rapid decay of resulting from inhomogeneities in the main magnetic field.

2.4 Gradients

The magnetic field gradient system can be used to spatially locate nuclear spins, thus allowing the development of magnetic resonance imaging from the NMR phenomenon. It consists of three orthogonal gradient coils, which are designed to produce time-varying gradients in the longitudinal magnetic field (Fig.2.7).

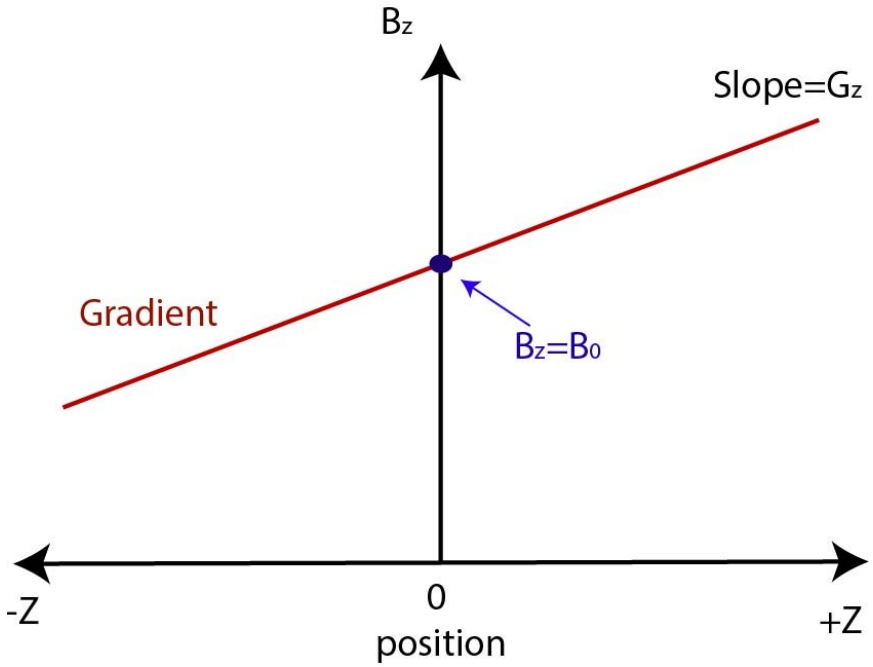

Figure 2.7: During a gradient pulse G_z where the magnetic field becomes a linear function of position on the z axis. $B_z = B_0$, at the centre of the magnet.

The gradient coils produce a linear variation of the magnetic field in the three directions, these are termed the x-gradient, G_x, the y-gradient, G_y, and the z-gradient, G_z (Weishaupt et al., 2006). The magnetic field of these gradients can be defined as follows:

$$G_x = \frac{\partial B_z}{\partial x}, \qquad G_y = \frac{\partial B_z}{\partial y}, \qquad G_z = \frac{\partial B_z}{\partial z} \qquad \text{Equation 2.7}$$

For example, the resultant magnetic field in the presence of a z-gradient can be expressed as:

$$B_z = B_0 + G_z z \qquad \text{Equation 2.8}$$

Where B_0 is the static magnetic field strength, G_z is a constant gradient measured in T/m, and z is the spatial location within the object being imaged.

Magnetic field gradients can be used to select a slice for imaging. The slice-selection gradient is applied in the presence of an RF pulse whose bandwidth matches the precession frequency of spins in a thin slice that is to be imaged (Mougin, 2010), as shown in Fig.2.8.

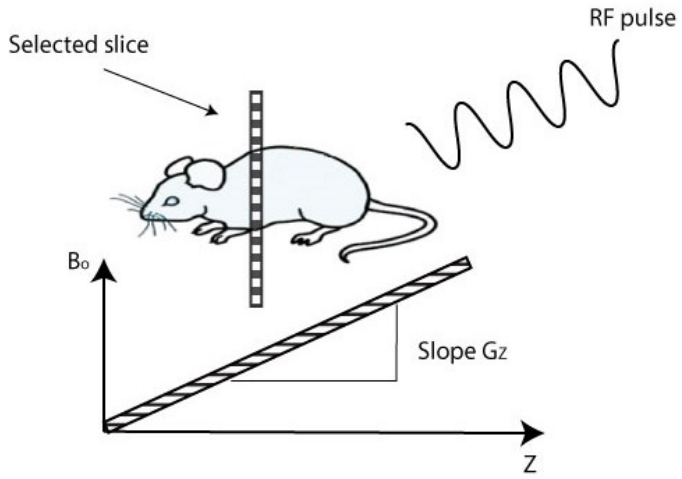

Figure 2.8: Principles of slice selection are achieved by applying a one-dimensional, linear magnetic field gradient during the period that the RF pulse is applied.

A slice can be acquired with any orientation, but it is generally acquired in three orthogonal directions relative to the brain, namely, axial, sagittal, and coronal. Figure 2.9 illustrates MRI brain images taken in the three slice orientations.

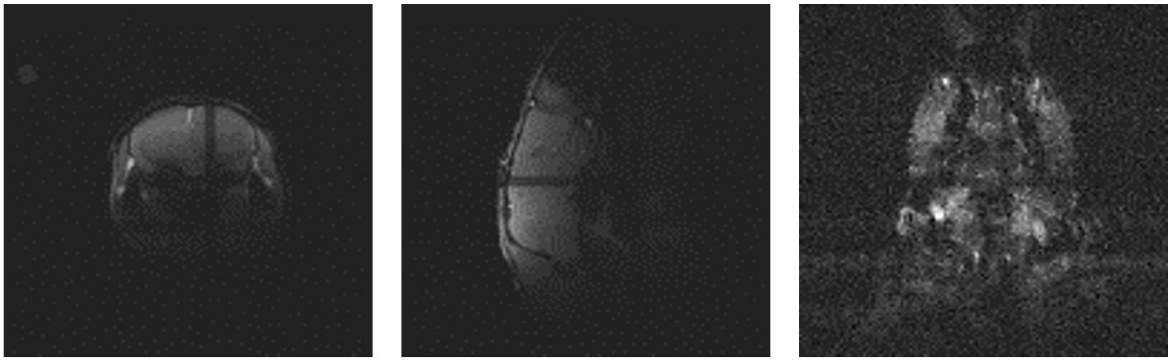

A B C

Figure 2.9: *In vivo* MRI images acquired by 7T scanner showing (A) Axial (B) Sagittal, and (C) Coronal.

These magnetic field gradients are used to perform spatial encoding in two ways: frequency encoding and phase encoding. In frequency encoding, the gradient is applied to make the precession frequency linearly related to the spatial location (combining Equations 2.1 and 2.8):

$$\omega(\mathrm{x}) = \omega_0 + \gamma \mathrm{G_x} x \qquad \text{Equation 2.9}$$

In phase encoding, the gradient is applied for a period of time (t_p), during which a phase is linearly accumulated along the phase encoding direction (z):

$$\phi(\mathrm{y}) = \gamma \mathrm{G_y} \mathrm{y} \mathrm{t_p} \qquad \text{Equation 2.10}$$

2.5 Gradient and spin echo sequences

In MRI, signals can be generated using either Gradient-Echo (GE) or Spin-Echo (SE) sequences. In GE sequences (Fig.2.10), the RF pulse is set to produce a magnetisation rotation angle, called the flip angle (α), of less than 90^o which is combined with short TEs and TRs. After the RF pulse, a negatively pulsed frequency-encoded gradient is immediately applied, causing rapid dephasing of the spins. A second frequency-encoded gradient with in opposite polarity is then applied, causing the spins to rephase. This is termed a gradient-echo. The signal obtained in this type of sequence depends on T2*, which is a fast decay following

the RF pulse. The time needed to produce an echo is shorter than that compared with SE sequences.

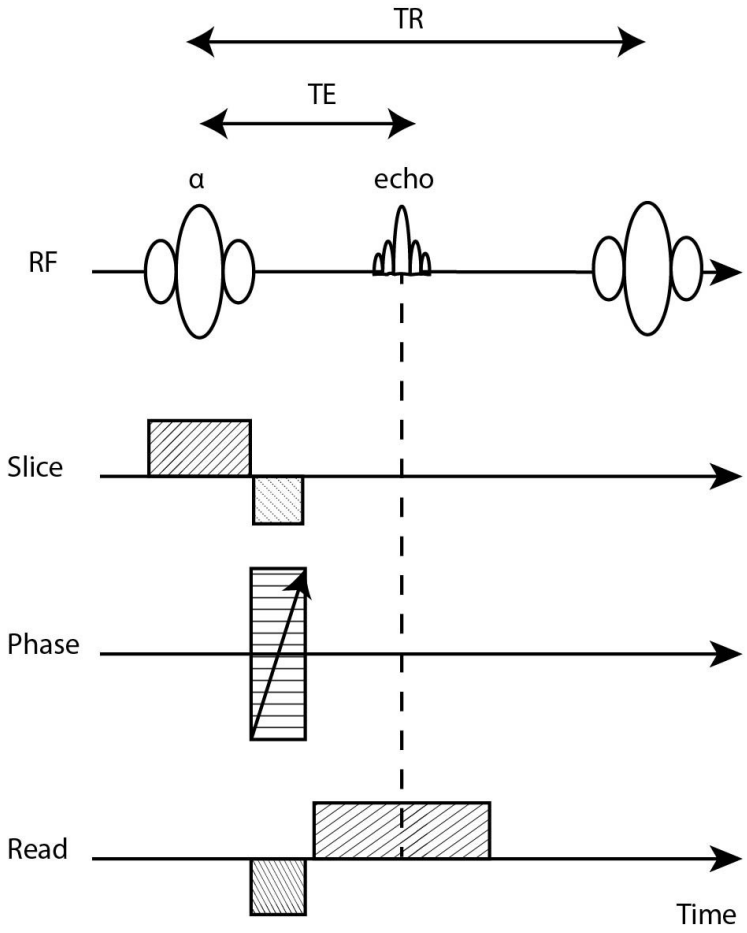

Figure 2.10: Time diagram of the basic gradient-echo sequence produced by a single RF pulse in conjunction with a gradient reversal. Adapted from (McRobbie et al., 2006).

In the basic SE sequence (Fig.2.11), a 90^{o} RF pulse is first used to excite the hydrogen nuclei. After a certain period of time, during which the spins dephase naturally, an additional 180^{o} pulse is applied (Westbrook et al., 2011). Such a pulse causes a rephasing of the spins, which produces an echo after a period equal to the time lapse between the two pulses.

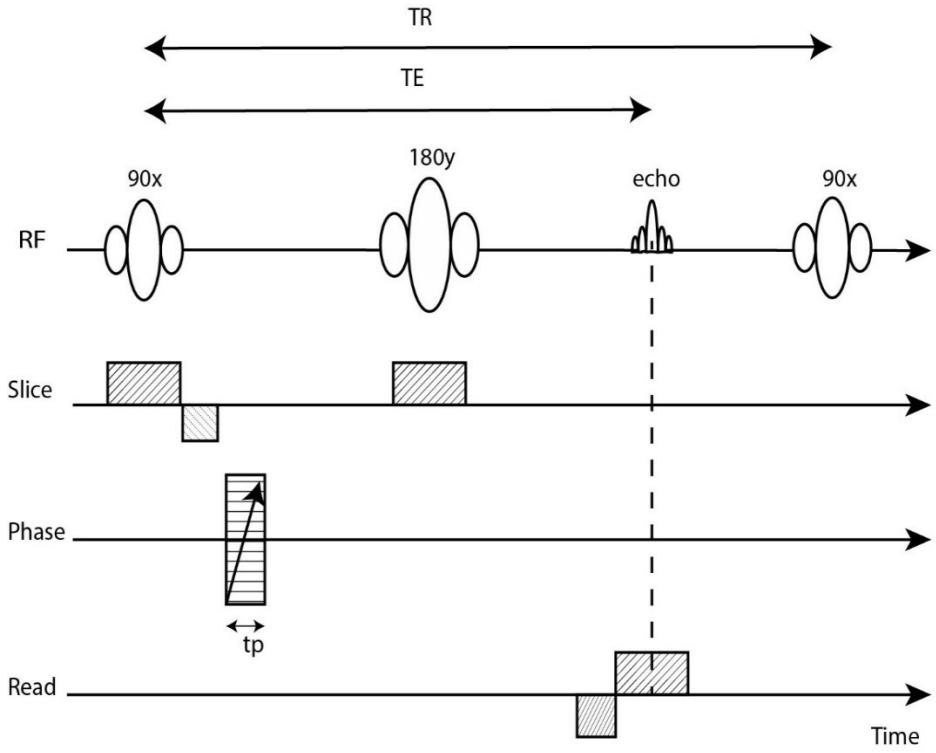

Figure 2.11: Time diagram of the basic spin-echo imaging sequence produced by pairs of radiofrequency pulses 90° and 180°, respectively. Adapted from (McRobbie et al., 2006).

TR is the repetition time (the time between two successive 90° RF pulses). TE is the echo time (the time between the 90° RF pulse and the centre of the spin-echo).

2.6 MR signal

RF excitation creates a net 'in-plane' magnetisation M_{xy}, the precession of which induces a signal in the receiver coil. The MRI signal can be expressed mathematically as follows:

$$s \propto \exp(i\phi) \qquad \text{Equation 2.11}$$

Where ϕ is the spin phase and $\phi = \omega t$, resulting in:

$$s \propto \exp(i\omega t) \qquad \text{Equation 2.12}$$

Inputting equation 2.1 into equation 2.11 resulting in,

$$s \propto \exp(i\gamma Bt) \qquad \text{Equation 2.13}$$

Where B external magnetic field and (t) time. In the rotating frame, while applying a gradient $B_z(x) = G_x.x$, the MRI signal is expressed as,

$$s \propto e^{i(\gamma G_x x)t} \qquad \text{Equation 2.14}$$

2.7 k-space

The Cartesian coordinates of the reciprocal space vector, k, are termed k-space (Fig.2.12). K space is a spatial frequency domain that contains the digitised complex signals received during an MRI scan (Westbrook et al., 2011). Each point in k-space contains both the magnitude and the phase of the measured signal samples recorded in k-space, which can be transformed into a magnetic resonance image by using Fourier transform (Yankeelov et al., 2012). The signal detected by the receiver during an MRI scan is an oscillating circularly polarised magnetic field which can be separated into real and imaginary components. Two different image types can be generated. Magnitude images are most commonly generated by taking the modulus of the real and imaginary data, as in equation 2.15. Phase images are generated by taking the complex argument of the data, as in equation 2.16. Conventional MR is viewed in the magnitude image, while the phase image can be used to investigate flow.

$$\text{Magnitude} = \sqrt{\text{real}^{\,2} + \text{imaginary}^{\,2}} \qquad \text{Equation 2.15}$$

$$\text{Phase} = \arctan(\text{imaginary}/\text{real}) \qquad \text{Equation 2.16}$$

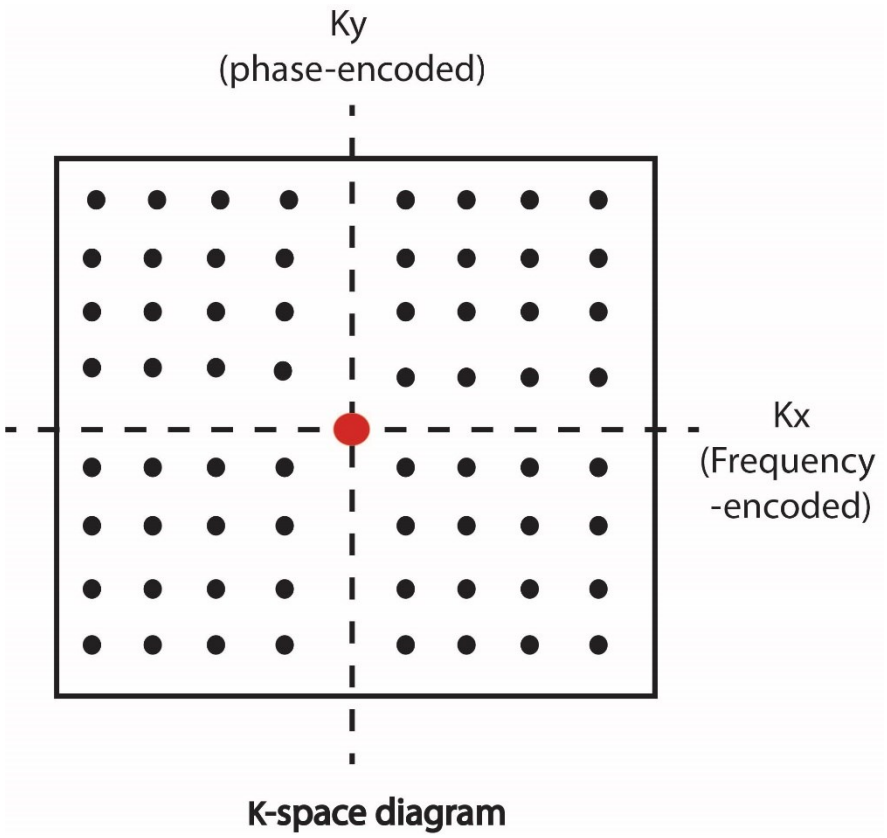

Figure 2.12: The analogue to digital conversion creates complex data points that are stored in a Cartesian grid called k-space, named after the reciprocal space vector k. Magnitude and phase images are generated by manipulation of the real and imaginary parts of the signal.

The frequency encoded (k_x) and phase encoded (k_y) in k-space are expressed as:

$$k_x = \frac{1}{2\pi}\,\gamma G_x . t \qquad \text{Equation 2.17}$$

$$k_y = \frac{1}{2\pi}\,\gamma G_y . t \qquad \text{Equation 2.18}$$

Integrating the signal for the whole sample, gives the total signal S(x,t). Equation 2.19 shows the Fourier relationship between the MRI signal and the spin density (ρ).

$$S(x,t) = \int_{-\infty}^{+\infty} \rho(x)\, e^{i2\pi(k.x)} dx \qquad \text{Equation 2.19}$$

2.8 Main parts of MRI scanner

In general, an MRI scanner includes the flowing elements:

1- The main magnet, which is commonly a coil made of superconducting wire immersed in liquid Helium, which carries a high electric current to generate a strong, stable, spatially uniform magnetic field B_0 ,(Kenneth W. Fishbein).

2- A shim system containing coils carrying a small current that are used to compensate for the inhomogeneity of the main magnetic field (B_0).

3- A gradient system consisting of three separate gradient coils, to produce linear gradients in the magnetic field in the x-, y-, and z-directions. These gradients are driven by powerful Direct Current (DC) amplifiers.

4- RF amplifier and RF transmit coil to produce the RF pulses.

5- Receiver coils (e.g. surface coil, head coil) used to receive signals from the body.

6- Various electrical components are controlling the scanner and the gradients, to create the MR images. For more details see Fig.2.13.

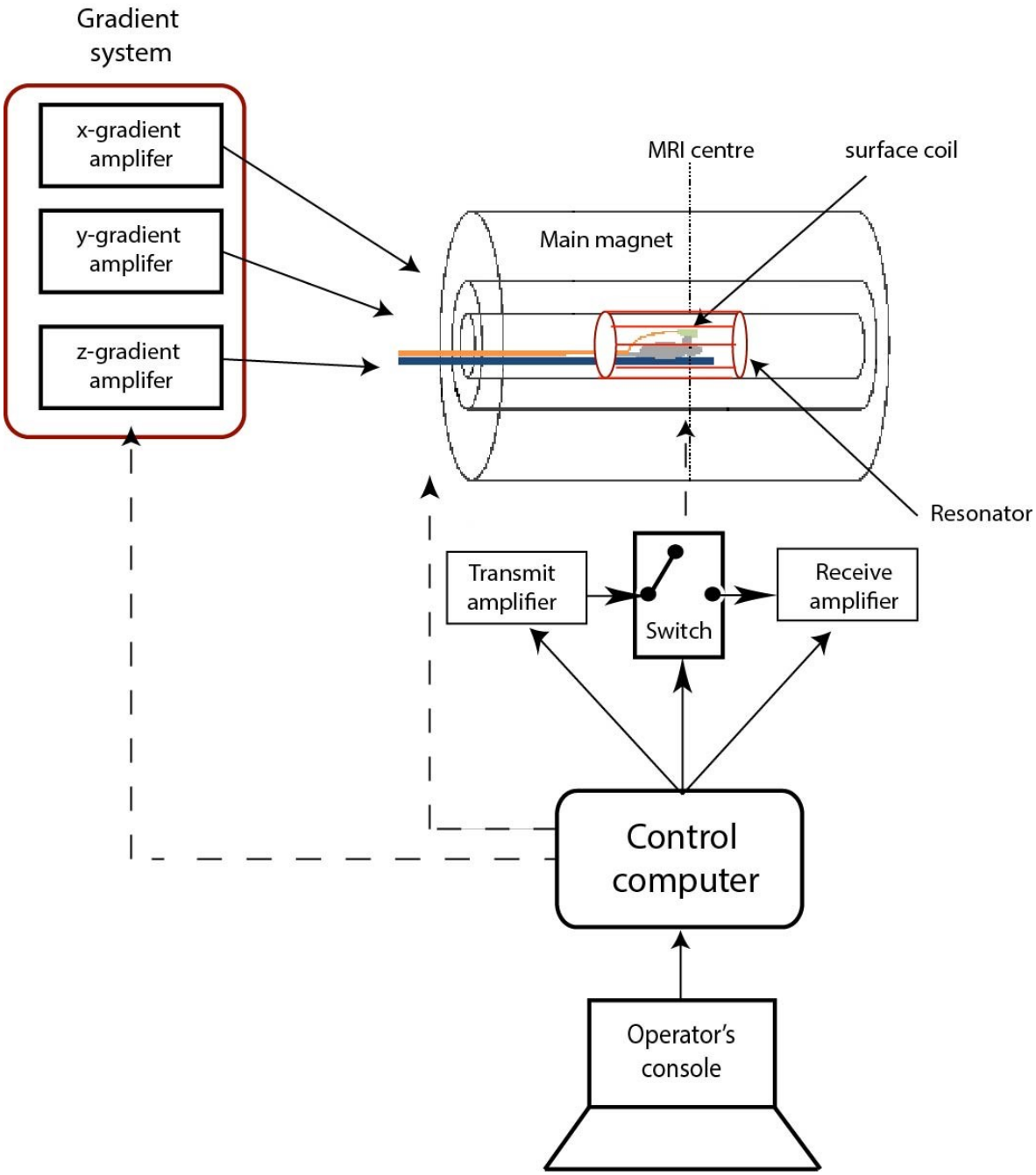

Figure 2.13: The major parts and electrical compounds of an MRI scanner are: the main magnet, gradient coils, shim system, RF transmitter and receiver, and the control computer.

2.9 Applications of relaxation

As discussed in section 2.3, the main relaxation processes are spin-lattice relaxation (T1 relaxation) and spin-spin relaxation (T2 relaxation). Relaxation produces the main form of contrast used in clinical MRI, as different tissues have different relaxation properties (Weishaupt et al., 2006).

2.9.1 T1 Weighted imaging

T1-weighting is obtained when both TE and TR are short. This procedure usually provides excellent contrast between fluids, water-based tissues, and fat-based tissues (McRobbie et al., 2006) . In the case of brain images, it presents a poor contrast between grey matter and white matter at 7 Tesla. In a T1W image, the CSF appears hypointense, while the brain tissues (GM and WM) appear with medium intensity, and fat has considerable hyper-intense values (Fig.2.14). Contrast agents can be intravenously injected, which alter the T1 of the tissue they perfuse (this is explained further in section 2.14.1).

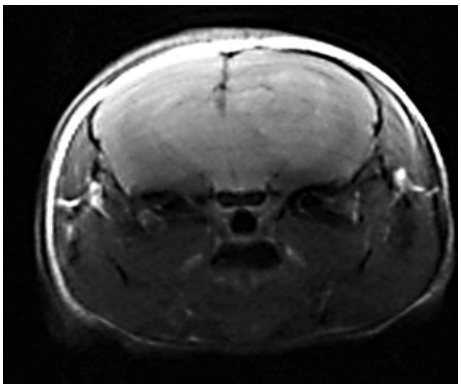

Figure 2.14: Example of T1W image of mice with a G7 tumour model at 7 Tesla. Image parameters are TE=12.28 ms, TR=800 ms at a resolution of 176x176 pixels.

2.9.2 T2 Weighted imaging

Spin-spin relaxation is a much more rapid process, which refers to the time taken for coherent nuclei to dephase. Spin-spin relaxation is also known as transverse relaxation or T2 relaxation, it describes the reduction in the transverse magnetisation vector M_{xy}. Regarding the T2 values of brain tissues, this protocol provides a good distinction between different parts of the brain e.g. GM, WM, CSF, and scalp fat. In regions with cerebrospinal fluid, e.g. the ventricles, the rapid molecular tumbling, results in the spin interactions occurring in shorter times with the slower loss of transverse coherence, which leads to a longer T2 time. Conversely, for more constrained structures such as the dense population of cells in the parenchyma, interaction and exchange with large molecules or solids result in faster loss of transverse coherence, which leads to shorter T2 times. Generally, in T2-Weighted images, fluids appear as hyperintensity, whilst water- and fat-

based tissues are mid-grey. Most tumours damage the microstructures of the brain, which prolong the T2 values of the affected tissue.

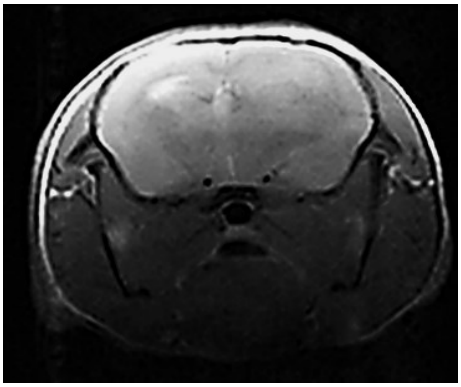

Figure 2.15: Example of T2W image of one nude mouse with G7 tumour type, TE= 47 ms, and TR = 4300 ms.

2.10 Diffusion

Robert Brown was the first to discover the random motion of pollen grains suspended in water while studying them through his microscope. Later, he demonstrated diffusive mixing by adding a few drops of ink to a glass of water, observing the ink spread (diffuse) and mix with the rest of the water (Moritani et al., 2005). This phenomenon is called 'Brownian motion'. Later, Einstein described diffusion statistically by this equation:

$$< x^2 >= 6D\Delta \qquad \text{Equation 2.20}$$

Where ($<x^2>$) is a mean square displacement during free diffusion that is proportional to the observation time (Δ), (Mukherjee et al., 2008) , Fig 2.16, and D is a constant, called the diffusion coefficient.

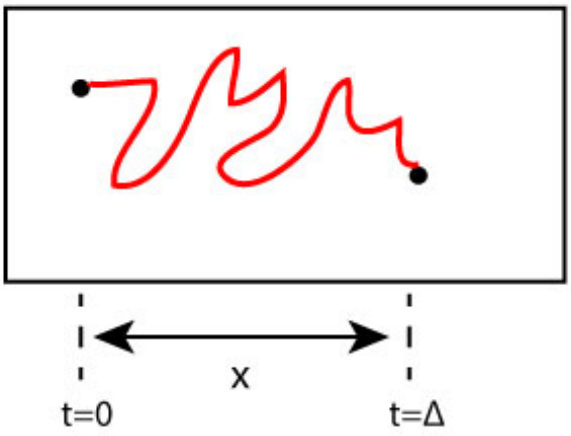

Figure 2.16: Free diffusing particle moving from two points, with displacement x, during observation time Δ.

2.10.1 Diffusion encoding

Stejskal and Tanner (1965) presented an NMR sequence sensitive to Brownian water motion. This sequence (Fig.2.17) is based on two gradients pulses (G) applied (in one spatial direction) on either side of 180º RF pulse. The presence of these gradients affects the spin-echo obtained at the end of the sequence. The greater the displacement of the spin along the gradient direction, the larger the dephasing and the greater the signal attenuation.

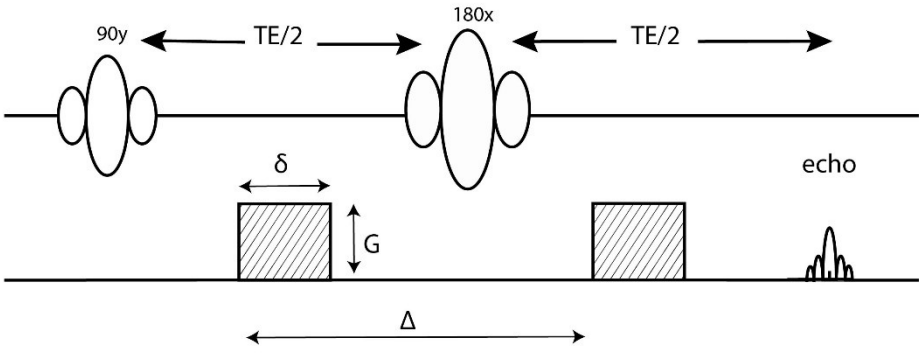

Figure 2.17: The Stejskal-Tanner sequence. The diffusion-encoding gradients are applied in two matched pulses. G gradient amplitude, δ gradient duration, Δ temporal separation of gradients.

During the first diffusion-encoding gradient, the spins accumulate a phase shift. If the spins are static, this phase shift is cancelled out by the second gradient, since

it has an identical magnitude to the first one, but an opposite sign due to the 180° pulse. For the spins that have changed position due to diffusion, the phase shifts are different, resulting in signal loss.

As spins are moving randomly with different displacement, this cause phase dispersion between the individual spins, producing a reduction of net magnetisation (M_0). Conversely, in the case of slow or restricted diffusion (GM or WM), the relative dephasing between spins is more limited, which results in less signal loss. The diffusion sensitivity of a sequence is determined by the (b) factor:

$$S\,(b) = S_o\,\exp^{(-bD)} \qquad \text{Equation 2.21}$$

Where

$$b = \gamma^2.\delta^2.G^2.(\Delta - \frac{\delta}{3}) \qquad \text{Equation 2.22}$$

Where γ is the gyromagnetic ratio (42.57 MHz/T for proton); G represents the gradient amplitude; δ represents application time of the gradient and Δ the observation time, represents the separation between applied gradients.

The MRI signal that shows the diffusion displacement of spins in the direction of the gradient, is called the diffusion weighted signal. DW signals are not quantitative and the image obtained from these signals is called a Diffusion Weighted Image (DWI).

In order to calculate D, signal intensity needs to be measured with at least two b values. In a clinical setting, typically two (b) factors, 0 and 1000 s/mm^2, are used. After performing a linear fit between ln (S_0/S) and b, the diffusion coefficient D can be calculated in a Region Of Interest (ROI) or voxel-by-voxel as the slope of linear regression (Mukherjee et al., 2008). For more detail see Fig.2.18.

$$D = \frac{\ln\left(\frac{S}{S_o}\right)}{b_x - b_o}$$ Equation 2.23

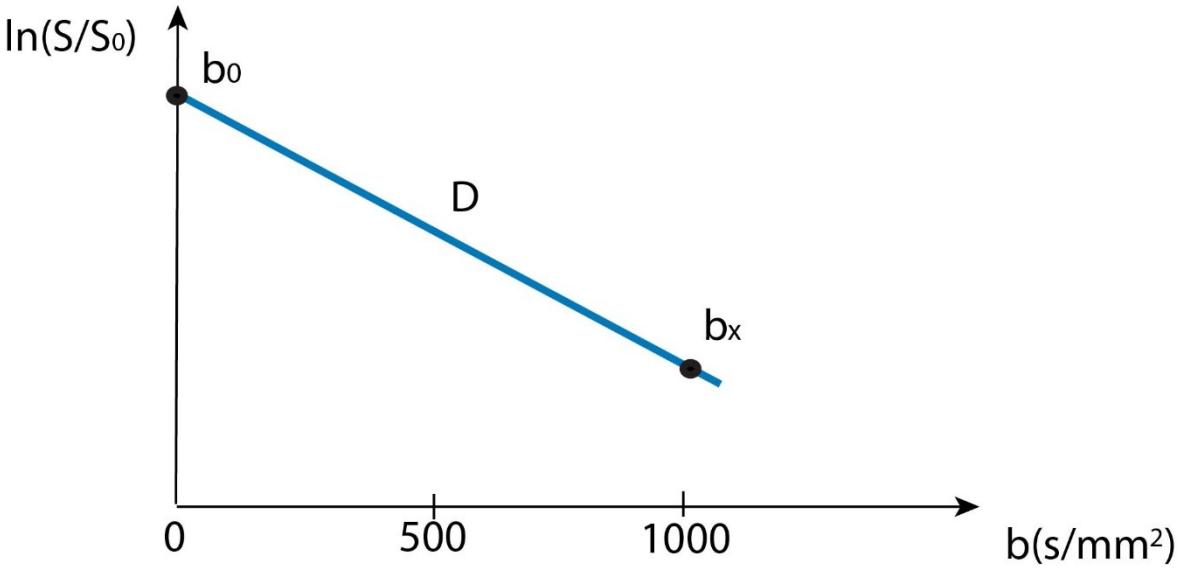

Figure 2.18: **Mono-exponential signal decay curve of water signal in diffusion MR. The natural logarithm of the diffusion MR signal attenuation curve (ln (S/S_0)) is shown against the b-value. The slope of the line represents the diffusion coefficient.**

2.10.2 Apparent diffusion coefficient

The measurement of the diffusion coefficients in three orthogonal directions (D_x, D_y, D_z) can be used to generate an Apparent Diffusion Coefficient (ADC), which is used to represent the quantitative measurement of the diffusion (mm^2/s) in three directions.

$$ADC = \frac{D_x + D_y + D_z}{3}$$ Equation 2.24

2.10.3 Diffusion tensor imaging

When diffusion is unrestricted and water molecules move randomly in all directions, the displacement can be modelled as a sphere and can be described by a single isotropic diffusion coefficient, D,(Mukherjee et al., 2008, Le Bihan et al., 2001). In the case of the molecules being restricted by their surrounding environment, diffusion may be greater in one particular direction than in other directions. Such anisotropic diffusion can be modelled as an ellipsoid (Fig.2.19).

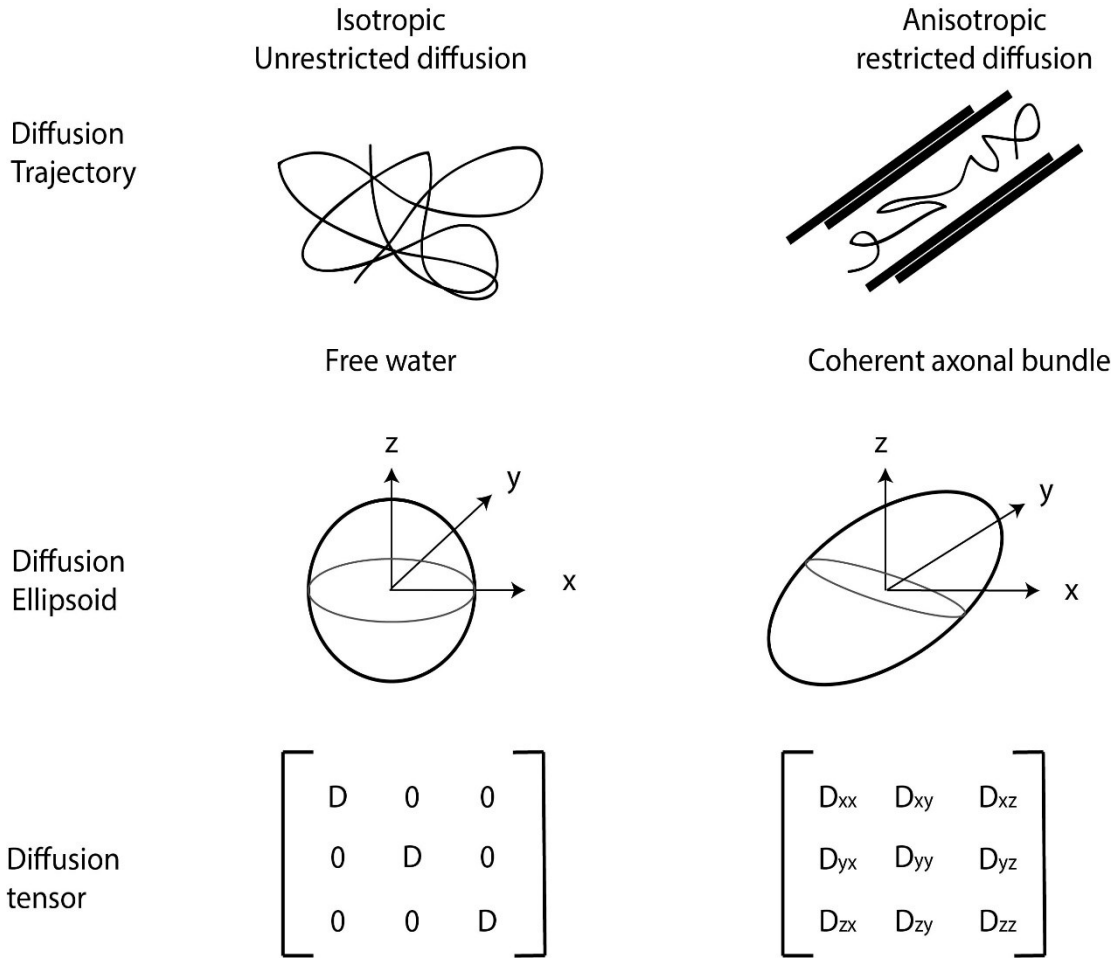

Figure 2.19: Illustration of isotropic diffusion and anisotropic restricted diffusion, with respective diffusion tensors. Adapted from (Mukherjee et al., 2008)

Diffusion tensor imaging (DTI) measurements in multiple directions of space (at least 6) can be used to produce a diffusion tensor for each voxel. The measures that can be extracted from the DTI dataset consist of the three eigenvalues (λ_1, λ_2 and λ_3) that represent the diffusion coefficients measured along the 3 eigenvectors (e_1, e_2, and e_3), (Hecke et al., 2016, Huisman, 2010). If these three

eigenvalues are of similar magnitude ($\lambda_1 \approx \lambda_2 \approx \lambda_3$), Fig.2.20A, the diffusion of water is not limited to any direction. However, restricted diffusion in a certain direction gives rise to diffusion anisotropy, Fig 2.2B, which can be quantified by the fractional anisotropy value (FA).

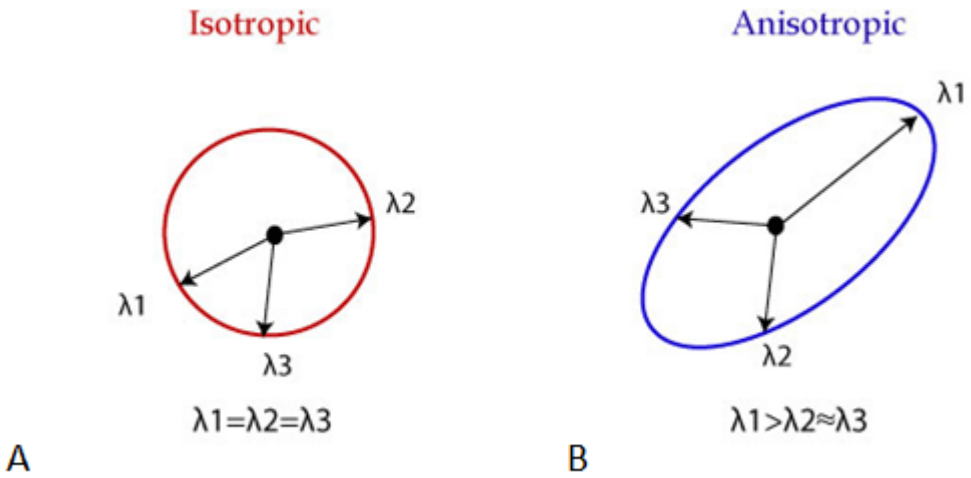

Figure 2.20: Representation of eigenvalues of isotropic and anisotropic diffusion of water.

FA can be computed (equation 2.25) as the ratio of the three eigenvalues, reflects the degree of directionality. FA has values between zero and one. FA=0 represents perfect isotropy (all eigenvalues are equal) and FA=1 corresponds to perfect anisotropy (diffusion in one direction only).

$$\mathrm{FA} = \sqrt{\frac{3}{2}\frac{(\lambda_1 - \mathrm{MD})^2 + (\lambda_2 - \mathrm{MD})^2 + (\lambda_3 - \mathrm{MD})^2}{\lambda_1 + \lambda_2 + \lambda_3}} \qquad \text{Equation 2.25}$$

Where MD is mean diffusivity:

$$\mathrm{MD} = \frac{\lambda_1 + \lambda_2 + \lambda_3}{3} \qquad \text{Equation 2.26}$$

2.11 Applications of diffusion weighted imaging

The microstructural properties of cancerous tissue, such as changes in cellularity or the number of cells in the tumour, can be indirectly measured using DWI and provide a useful contrast difference between normal and tumour regions (White et al., 2014), Fig.2.21. DWI is currently considered a cancer biomarker and has a role in cancer detection staging and follow-up treatment (Villanueva-Meyer et al., 2017, Huisman, 2010).

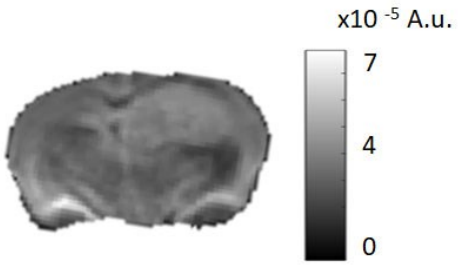

Figure 2.21: Example of DWI with a malignant tumour in a mouse brain. Acquired using b=1000 s/mm^2.

Several researchers have demonstrated the potential use of ADC as a non-invasive probe of tumour microstructure, which has motivated clinical and preclinical research to use ADC mapping to scan tumours (Moritani et al., 2005, Hecke et al., 2016). ADC measurement depends on the two b values, for example, measurements using low b values would be more sensitive to fast diffusion components such as blood, and measurement with high b values would be more sensitive to microstructure of the tissue (Drevelegas, 2011), Fig.2.22.

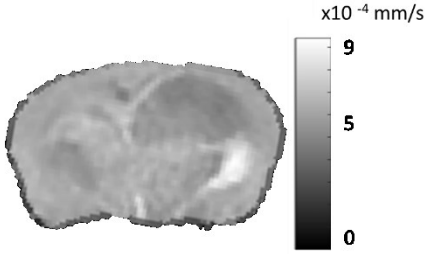

Figure 2.22: Voxel-by voxel calculation of ADC values results in an ADC map.

The magnitude and direction of diffusion of water molecules is determined by the geometry of the environment of the water spins. In grey matter, an FA value close to 0.2 is expected when little diffusion anisotropy is present, while in white matter, anisotropy is high and the FA values are expected to be nearer to 0.6, indicating a preferred direction of water diffusion, Fig.2.23.

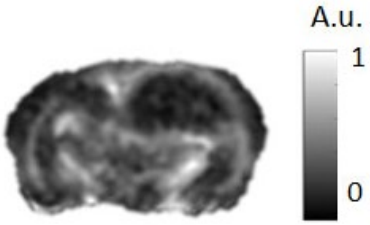

Figure 2.23: Example of FA image map that is a quantitative measure of the micro-structural integrity and cohesion of white matter tracts.

2.12 Blood brain barrier integrity

The Blood–Brain Barrier (BBB) was discovered in the late 19th century by Paul Ehrlich when he injected a dye into the bloodstream of a mouse. The dye infiltrated all tissues except the brain and spinal cord due to the existence of the blood–brain barrier. The blood–brain barrier is formed by endothelial cells of the blood vessel wall, astrocyte end-feet covering more than 90% of the blood vessel surface, pericytes embedded in the blood vessel basement membrane, and tight junctions (Ballabh et al., 2004). For more detail see Fig.2.24.

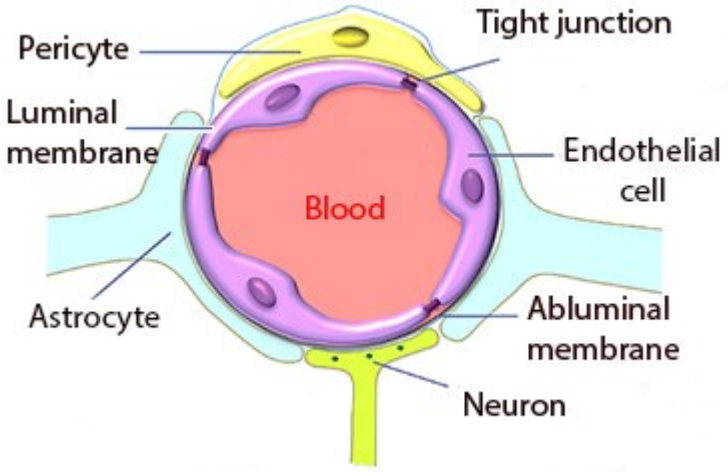

Figure 2.24: The illustration of the blood-brain barrier components. Adapted from (Liu et al., 2012).

This system allows the passage of some molecules by diffusion of substances such as glucose, water, and amino acids that are crucial to neural function. The loss of contact between astrocyte end-feet and blood vessels due to glioblastoma cells leads to disruption of the tight junctions, which allows the BBB to pass harmful materials into the brain (Watkins et al., 2014).

The relationship between BBB breakdown and disease is not fully understood. For example, disruption of the BBB due to tumour cells enables the brain blood vessels to become accessible to low-molecular weight MRI contrast agents (Liu et al., 2012). The disruption of the BBB in the tumour vasculature could play an important role in developing new therapies for gliomas and help to identify a biomarker for early diagnosis.

2.13 Perfusion

Perfusion is a physiological process by which the body delivers blood to the microvasculature, where oxygen and glucose exchange with local tissue. Tumours typically require more oxygen and nutrients than normal tissue to sustain their high rates of growth and development. To meet this higher demand for oxygen and nutrients, tumours create new vascular networks, a process called angiogenesis (Hardee and Zagzag, 2012).

Tumour blood vessels are less regular and organized than those in healthy tissue, which may increase tortuosity as it moves through a tumour due to neovascularization, therefore, perfusion abnormalities are detected not only because of the increased number of vessels (angiogenesis) in a tumour ,but also because of the abnormal reaction of those vessels to the environment (Chen, 2011), Fig.2.25.

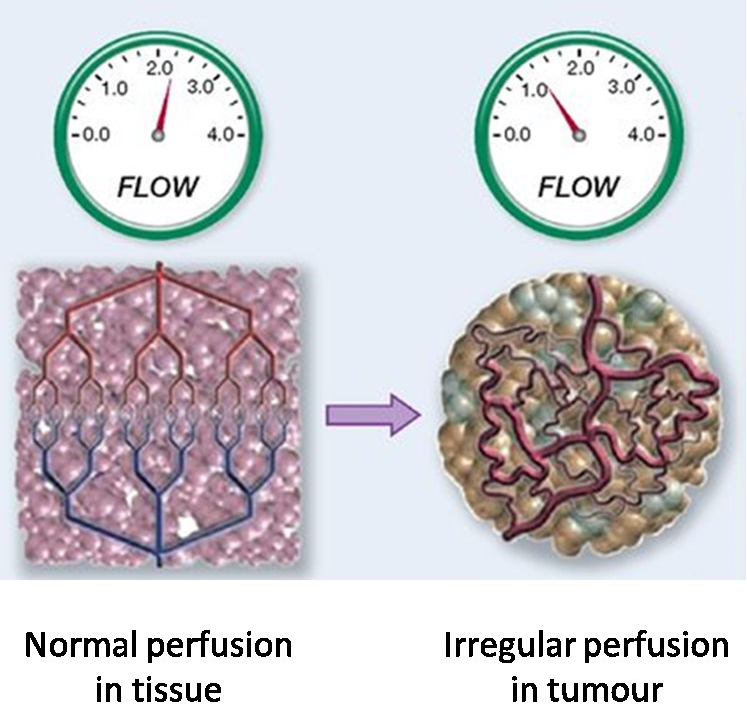

Figure 2.25: Schematic diagram illustrating the difference in flow between normal and abnormal tissue. Adapted from (Kalpathy-Cramer et al., 2014).

Neovascularization, one of the features of glioblastoma pathology, may cause a change in regional cerebral perfusion and vascular permeability. The importance of neovascularisation is nowadays widely accepted in the grading of gliomas. These new abnormal vessels, which grow in the region of the oedema, can be characterized by decreased blood flow and increased permeability. These characteristics can be used as biomarkers for the evaluation of tumour growth (Chen, 2011).

2.14 Perfusion weighted magnetic resonance imaging

Perfusion imaging provides a non-invasive quantitative method for assessing tumour perfusion and vascularization (Prasad, 2006). There are three principal techniques: Dynamic Contrast-Enhanced (DCE) MRI, Dynamic Susceptibility Contrast (DSC) and Arterial Spin Labelling (ASL), (Cuenod and Balvay, 2013). The labelling method can be based either on an exogenous contrast agent, for example, a paramagnetic complex of gadolinium (DCE, DSC), or on the magnetic labelling of the endogenous water molecules (ASL).

2.14.1 Contrast enhanced T1

The contrast of the T1W image can be improved by injecting a contrast agent such as gadolinium (Gd), Fig.2.26. This shortens the T1 relaxation time, thereby causing increased signal intensity on T1W images.

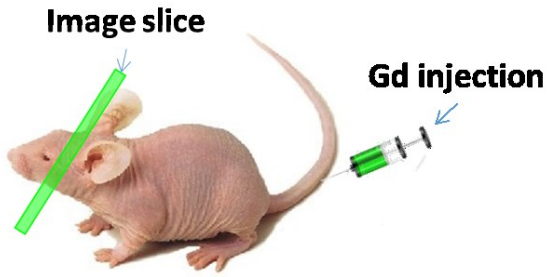

Figure 2.26: The injection of contrast agent (Gd) into mouse tail and image slice location.

The basis for using contrast-agents for brain tumour imaging is that the contrast agent does not pass the blood vessel wall inside healthy brain tissue and remains in the blood vessels. However, malignant brain tumours cause damage (disruption) to the blood brain barrier which allows the contrast agent to leave the vessels and leak into the tissue. The affected region will have a shorter T1 that results in a hyperintense appearance (contrast enhanced area) on the T1W images (Fig.2.27).

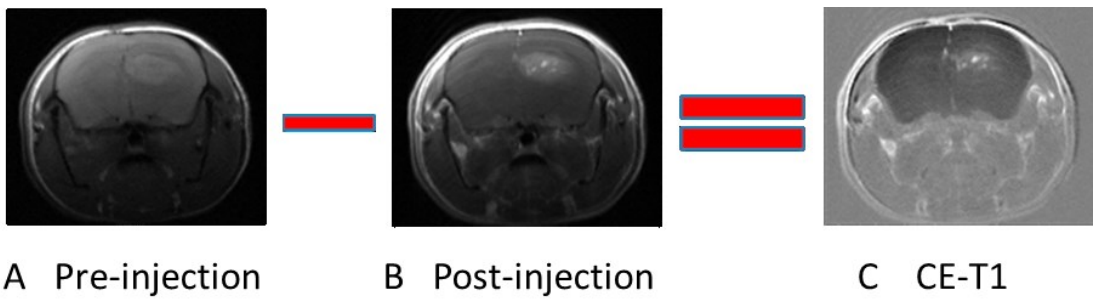

Figure 2.27: T1W brain image (A) before and (B) after injection of Gd contrast. (C) The CE-T1 image shows a necrotic tumour core surrounded by a hyper-intense ring of contrast enhancement caused by a leaky tumour vasculature.

2.14.2 Dynamic contrast enhanced

Dynamic Contrast Enhanced MRI could be used to assess perfusion parameters. The sequence requires the bolus injection of a contrast agent followed by the rapid acquisition of T1W images over time (Kalpathy-Cramer et al., 2014). The dynamic changes in the contrast agent concentration are used to calculate physiological parameters such as blood volume, blood flow, transit time, and blood vessel wall permeability (Chen, 2011). These perfusion parameters are important in order to describe the physiological changes that occur during tumour development or in response to therapy.

2.14.3 Dynamic susceptibility contrast MRI

In dynamic susceptibility Contrast MRI images, the first pass of a bolus of contrast agent through the brain by a series of T2*-Weighted images generates a signal intensity time curve (Chen, 2011). The drop in signal is proportional to the concentration of the contrast agent and to tissue vascularization. From this curve, multiple hemodynamic parameters (for each pixel) can be determined, such as the time to peak, Mean Transit Time (MTT), Cerebral Blood Flow (CBF), Cerebral Blood Volume (CBV) and perfusion maps.

2.14.4 Arterial spin labelling

Arterial Spin Labelling (ASL) is a completely non-invasive method based on the use of blood-water protons as an endogenous tracer to obtain information about blood flow in the tissue (Dai et al., 2008). Flowing blood is inverted (labelled) at the neck of a mouse and its arrival in the tissue of interest is measured (Gregori, 2015). ASL treats the tissue of interest as two compartments: tissue parenchyma and blood. First, parenchyma is considered to consist largely of static (non-inverted) spins, but there is an exchange between the compartments. Second, the blood which comes from the arterial is inverted magnetization and diffuses through the blood–brain barrier to parenchyma,(Yankeelov et al., 2012), Fig.2.28.

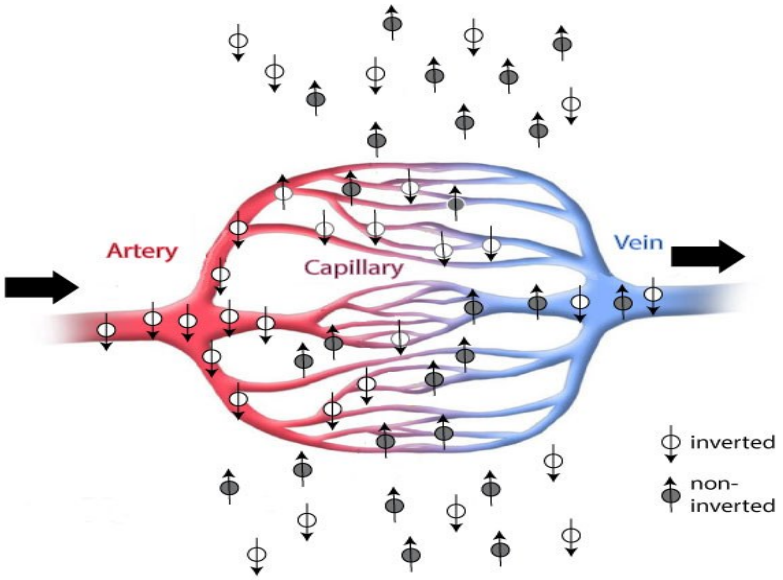

Figure 2.28 : The principles of freely diffusible tracer theory. Inverted magnetization comes from the arterial blood water (white arrow) and diffuses through the blood–brain barrier at the capillary level. Hence, spins are exchanged with the tissue magnetization, and reduce its local intensity. The degree of attenuation is a direct measure of perfusion. Remaining tagged magnetization as well as exchanged water molecules flow out of the voxel of interest through the venous system (grey arrow). Adapted from (Golay et al., 2004).

The application of an RF pulse inverts the net magnetization of the water in the blood. After a certain time (Inversion Time, TI), an image is acquired which is called a labelled or tagged image. The image that is acquired without the inversion of the net magnetization of blood water is called a control image (Fig.2.29A). This perfusion-weighted signal (ASL signal) can be isolated by subtracting a labelled image from the control image in which the arterial blood magnetization is at equilibrium (Fig.29B). Since the blood occupies, on average, ~4% of the brain tissue, the difference in blood signal is relatively small compared with the total brain signal. The disadvantages of ASL are its low signal compared with DSC MRI, longer acquisition times, and a relatively complex acquisition procedure, which may explain its lower use compared with DSC MRI (Detre et al., 2009). There are two ways of tagging arterial blood water: pulsed and continuous ASL (Dai et al., 2008).

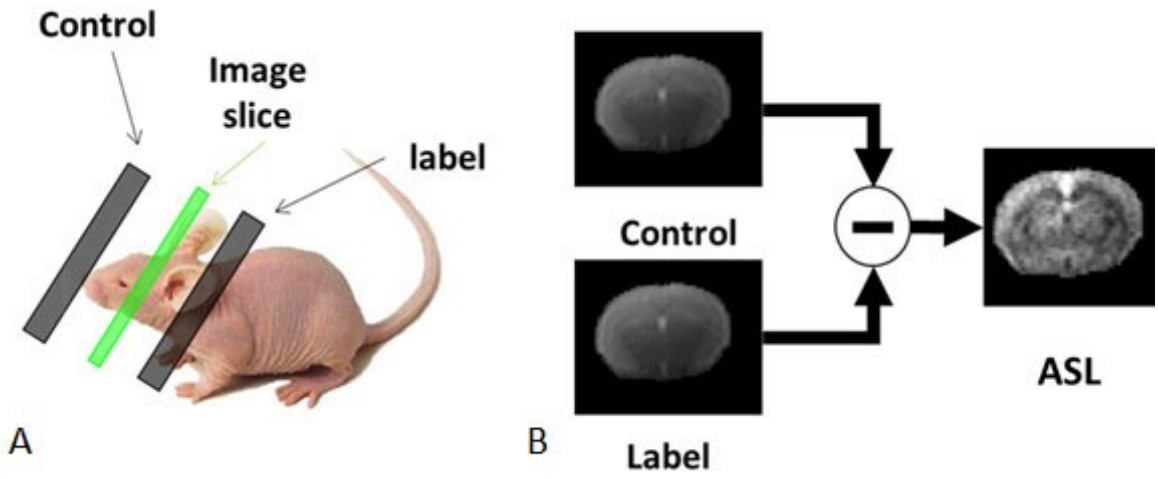

Figure 2.29: (A) Perfusion imaging, showing the control and label slices positioned on a mouse head. (B) Example of a control and label image with the corresponding perfusion weighted ASL subtraction.

2.14.4.1 Multiple boli arterial spin labelling

In this work, a new high-SNR sequence, namely, multiple boli Arterial Spin Labelling (mbASL) is used to measure perfusion (Fig.30A). In this sequence, the train of adiabatic pulses (a hyperbolic secant) is applied to label the thin slice (label slice) in the neck of a mouse, with the spin at the level of the carotid arteries (Fig. 2.30B). To minimize the magnetization Transfer Effect (TE), the adiabatic train is also applied to the control image, but on the opposite of the imaging plane and using a gradient of opposite sign (Vallatos et al., 2018b).

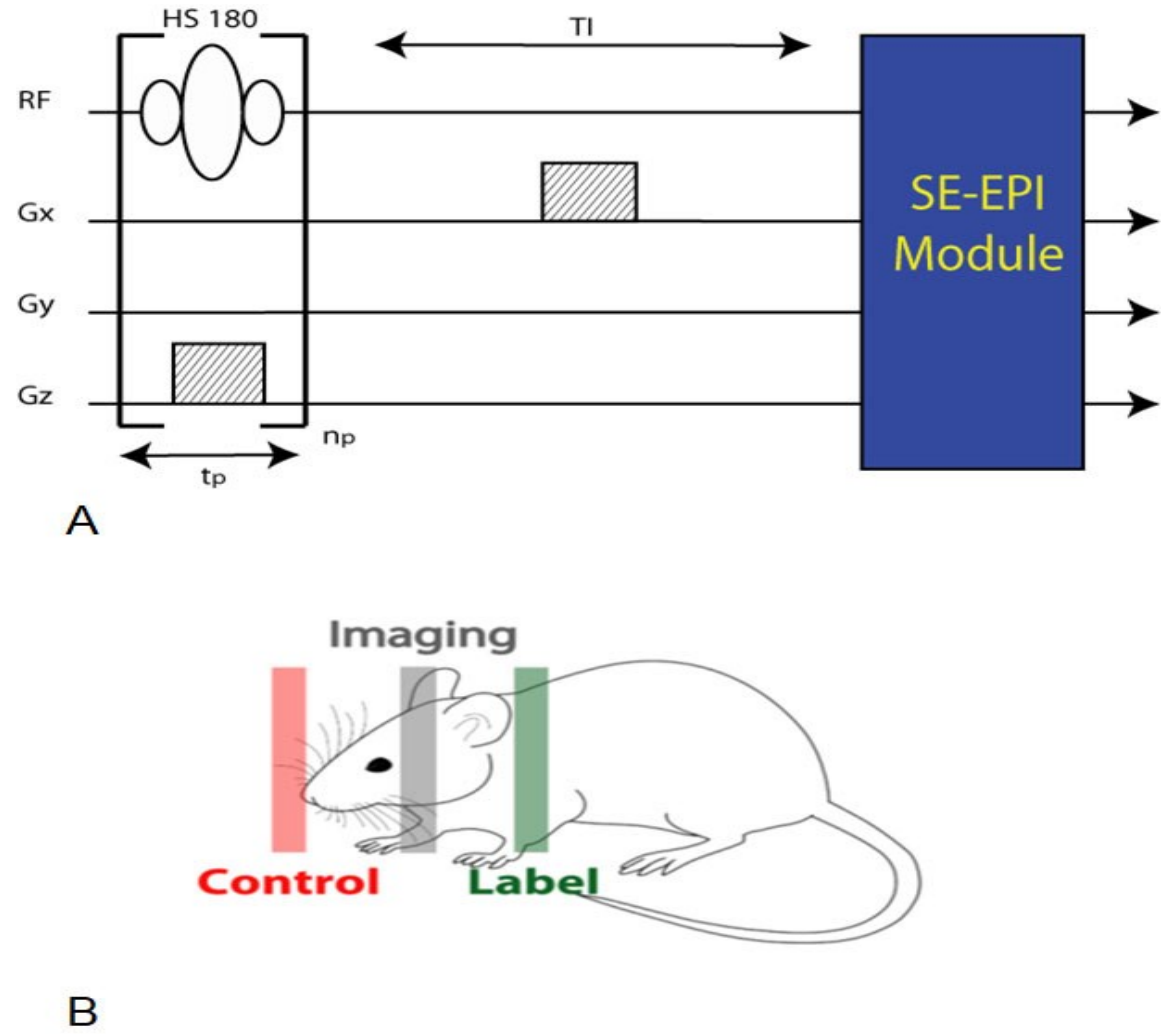

Figure 2.30: (A) Pulse sequence diagram for mbASL, (B) The location of the label, control and imaging slices. Adapted from (Vallatos et al., 2018b).

After a post-labelling delay (inversion time), the acquired image (label image) is subtracted from the control image without labelling to obtain the perfusion weighted image (Fig.2.31).

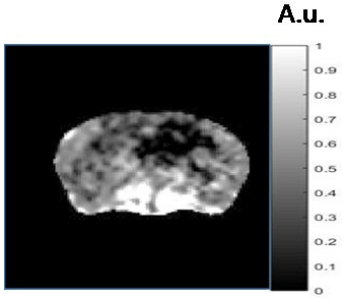

Figure 2.31: Example of perfusion weighted image using mbASL after subtracting label from control image. The GB tumour in the right hemisphere shows clear hypoperfusion.

2.15 Applications of ASL

Measuring blood flow is important for the characterization of tumours for several reasons. For example, aggressive tumours typically have higher blood flow and, hence, blood flow measurement can be an indicator of tumour grade (Yeom et al., 2014) and can aid in the differentiation of GB from brain metastases (Tourdias et al., 2008). Furthermore, treatments that block the development of the tumour's blood supply have become promising approaches to tumour therapy.

ASL offers several important advantages in tumour blood flow assessment. ASL offers absolute quantification that can be used to compare tumour blood flow values measured throughout therapy (Golay et al., 2004). Another key strength of MR blood flow measurement in brain tumours is co-registration with anatomical imaging such as T1W, T2W and DWI, obtained in the same scanning session. The need for such co-registration between anatomical and functional information can be used for interpretation of the functional information with anatomical guidance. In the next chapters, we will co-register mbASL with clinic MRI to obtain complementary information.

Chapter 3

An introduction to Image Analysis Techniques

3.1 Introduction

As soon as MR images are acquired from an MRI scanner, there is a need for further image processing steps. In this study, MR images required one or more image processing steps, such as pre-processing and post-processing, before data analysis. The software used for this processing was MATLAB 2015a, which can easily manipulate data to conduct the necessary measurements and analysis.

3.2 MRI pre-processing

Generally, pre-processing techniques are used to improve image quality. For example, it is necessary to remove small imperfections that arise due to scanning, and noise (discussed later in section 3.2.6) on the image. This involves those operations that are conducted before the main goal of analysis and the extraction of the desired information. For example, normally there is a need for geometric corrections, such as rotation of the original image.

3.2.1 Retrieve data

MR images were acquired as Digital Imaging and Communication in Medicine (DICOM) files by using Paravison 5.1 software (Bruker Biospin). DICOM data were rescaled to retrieve original image intensity values. Each imaging modality must be multiplied by the rescaled value obtained from the DICOM structure file.

3.2.2 Normalisation

Normalisation is a process that changes the range of pixel intensity values in order to keep the image from presenting a specific narrow intensity that is less interesting to the observer (Brody and Zerhouni, 2000). However, this process may result in the loss some of the information in the image. It is very important to ensure that pixel values in all the MR images are in the same range (Demirkaya et al., 2008) to make a comparison amongst images. The first method of normalisation is to divide the whole image pixels by the maximum intensity value of the image to change the image intensity to scale [0-1]. Another way of utilizing normalisation is take to take the pixels' images, subtract them from the mean value and divide by the Standard Deviation (STD) of the entirety of all pixel images according to equation 3.1.

$$z = \frac{x - m}{\sigma}$$ Equation 3.1

Where z is the new value, x is the old pixel value, m is the mean value and σ is the standard deviation of the whole brain image.

Finally, normalized relative perfusion maps (mbASL) are produced by subtracting the control and label images and dividing by the control, $(M_{control}-M_{label})/M_{control}$. Contrast-enhanced images (CE-T1) were produced by subtracting the T1W image acquired before and after Gd-DTPA injection and normalized by using the equation $(M_{post}-M_{pre})/M_{pre}$.

3.2.3 Sensitivity of surface coil

Non-uniform detection sensitivity is associated with the use of a surface receiver coil. This occurs due to the surface coil's signal drop-off with increasing distance from the coil plane (Wallner et al., 1990) ,for more details see Fig.3.1. It can adversely affect the result of image registration.

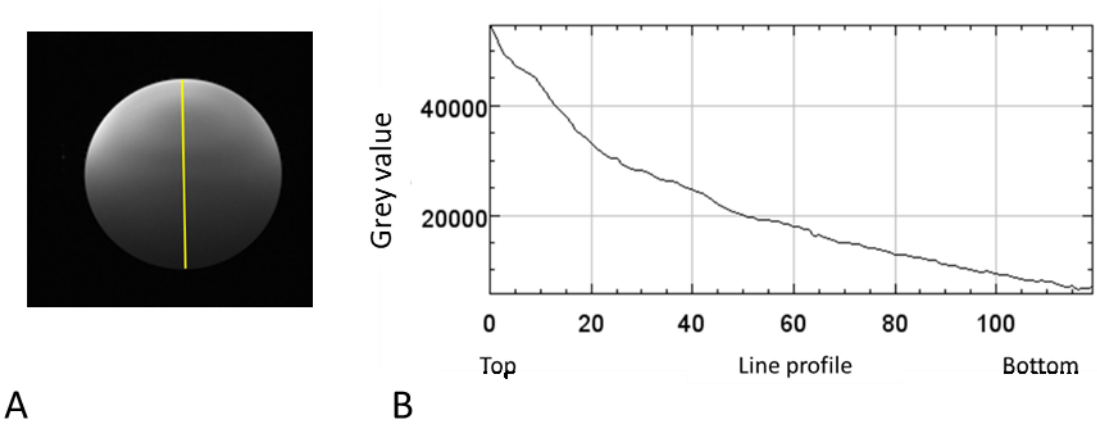

Figure 3.1: (A) Image of a water phantom, with vertical profile line. (B) Plot representing pixels' intensity along the yellow line shown in (A).

A phantom is a specially designed object filled with gelatine or water generally used to evaluate the performance of various imaging devices. In this study, a phantom was used to correct surface coil sensitivity for T1W, T2W and DWI

images, dividing by the corresponding phantom images (Axel et al., 1987). Figure 3.2 shows an example of removing the sensitivity of surface coil from a DW image.

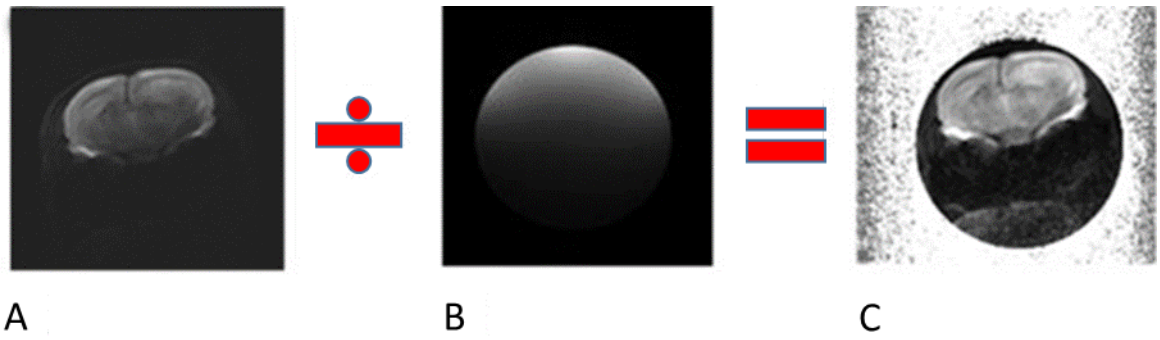

Figure 3.2: (A) DWI before removing sensitivity of surface coil (B) phantom image (C) DWI after removing sensitivity of surface coil.

3.2.4 ADC map calculation

Apparent Diffusion Coefficient (ADC) maps were calculated by fitting the DWI data to the mono-exponential equation of Stejskal and Tanner (Stejskal and Tanner, 1965). DTI data were analysed using Paravison 5.1 software (Bruker biospin), with an emphasis on FA and ADC images. All data were resampled to match the T2W matrix (176x176) by using the cubic-spline method.

3.2.5 Skull stripping

Skull stripping is an essential part of many medical image analysis applications that study the brain. It is the process of removing non-brain tissue (skull and background) from an MR image of the brain. The brain region can be separated from the skull and background. For example, using an active contour method to find, and extract, brain boundaries after manual delineation (Vicent et al., 1997). The background pixel values will be equal to the null value to reduce processing time. Figure 3.3 shows an example of extracting the brain from a T2W image.

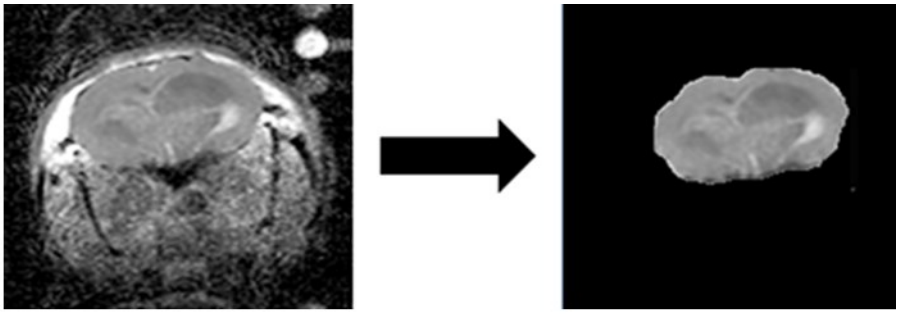

A B

Figure 3.3: (A) T2W image shows whole brain with tumour in the right hemisphere. (B) After skull stripping only the brain remains.

3.2.6 Filter

Noise is a common problem in medical images such as X-rays or MRI. Errors in the image acquisition process result in pixel values that do not reflect the true signal intensities. The purpose of a filter is to reduce noise and improve the visual quality of the image. Despite the existence of many different methods to remove noise, accurate removal of noise from MRI is still a challenge (Roy et al., 2013).

A filter has several disadvantages. For example, it can significantly affect the sharpness and reduce the visibility (blurring) of the image.

An anisotropic diffusion filter was utilized to remove noise from flat regions and retain the edges in the image. This filter depends on the diffusion principle. Diffusion is the movement of particles from high concentration to low concentration and can be described by the equation:

$$j = -D\nabla u \qquad \text{Equation 3.2}$$

Where the j is flux density, D is the diffusion coefficient which is constant and depends on the material, and $\overrightarrow{\nabla u} = \left(\frac{\partial u}{\partial x} + \frac{\partial u}{\partial x} + \frac{\partial u}{\partial x} \right)$ denotes the gradient of the concentration μ.

This equation, known as Fick's first law of diffusion, means the change in concentration is the driving force for the movement (flux):

$$\frac{\partial \mathrm{u}}{\partial t} = -\mathrm{div}\,\mathrm{j} \qquad \text{Equation 3.3}$$

Where div is the divergence and t is time, which is a consequence of the fact that the number of particles remains constant. div is equal to:

$$\mathrm{div} = \frac{\partial}{\partial \mathrm{x}} + \frac{\partial}{\partial \mathrm{y}} + \frac{\partial}{\partial \mathrm{z}} \qquad \text{Equation 3.4}$$

After substituting Fick's first law eq. (3.2) with eq. (3.3), we can obtain Fick's second law of diffusion as follows:

$$\frac{\partial \mathrm{u}}{\partial t} = -\mathrm{div}(-\mathrm{D}\nabla \mathrm{u}) \qquad \text{Equation 3.5}$$

$$\frac{\partial \mathrm{u}}{\partial t} = \mathrm{D}\left(\frac{\partial^2 \mathrm{u}}{\partial \mathrm{x}^2} + \frac{\partial^2 \mathrm{u}}{\partial \mathrm{y}^2} + \frac{\partial^2 \mathrm{u}}{\partial \mathrm{z}^2}\right) \qquad \text{Equation 3.6}$$

$$\frac{\partial \mathrm{u}}{\partial t} = \mathrm{D}\nabla^2 \mathrm{u} \qquad \text{Equation 3.7}$$

Therefore, the traditional nonlinear diffusion filtering method, which was proposed by Perona and Malik (Perona and Malik, 1990), can be described as follows:

$$\begin{cases} \dfrac{\partial \mathrm{u}}{\partial t} = \mathrm{div}(\mathrm{g}|\nabla \mathrm{u}|).\nabla \mathrm{u}] \\ \mathrm{u}(\mathrm{t}=0) = \mathrm{uo} \end{cases} \qquad \text{Equation 3.8}$$

Where $|\nabla|$ is the gradient operator, u is the smoothed image, $|\nabla \mathrm{u}|$ the gradient magnitude of u and $\mathrm{g}|\nabla \mathrm{u}|$ is diffusivity gradient function. Under the control of g ($|\nabla|$), the model can achieve a selective smooth diffusion from the original image based on the gradient. At the edge, the gradient magnitude is large, g($|\nabla|$), and

the model will not perform smoothing to retain the edge details. By contrast, when the gradient magnitude is small, $g(|\nabla|)$ at a flat area, the model will perform smoothing and remove the noise. Figure 3.4 shows an example of applying anisotropic diffusion filter on mouse brain image. The MATLAB code of anisotropic diffusion filter was derived from Demirkaya et al. (2008).

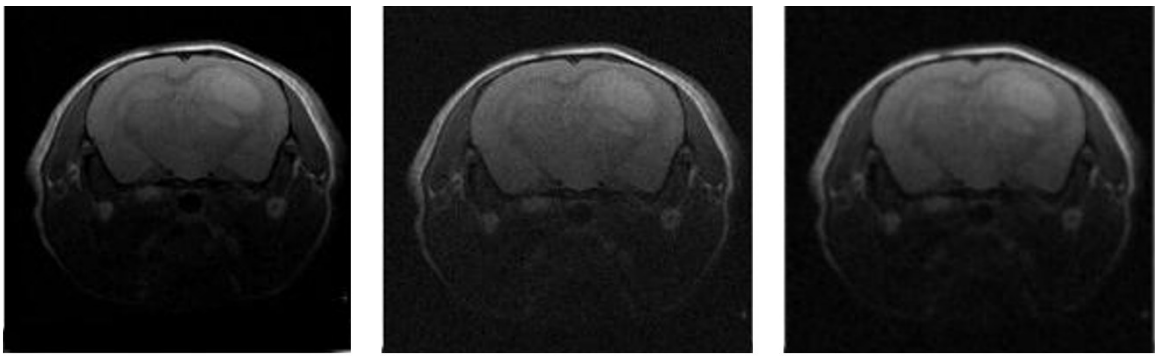

Figure 3.4: (A) Original image of mouse brain tumour. (B) After applying noise. (C) After applying anisotropic diffusion filter.

3.3 MRI Post-processing

The post-processing steps occur only on the remaining brain voxels after pre-processing to reduce processing time. This process includes segmentation and registration.

3.3.1 Segmentation

Image segmentation is one of the most important and active research areas in the medical imaging domain. The purpose of image segmentation is to divide the image into regions based on given criteria which, in medical imaging, may correspond to the tissue type, structure, or function. For example, a brain tumour image can be divided, after segmentation, into white matter, grey matter, cerebral spinal fluid, and the tumour region (Liu et al., 2014).

The segmentation of a brain tumour (glioma high grade) in MRI is a challenging task for several reasons. Tumours may have heterogeneous appearances, have

different textures, have irregular boundaries, or the tumour borders may be unclear and discontinuous due to infiltration.

The main difficulties in segmentation are the noise (Diaz et al., 2011), blur, low contrast, sensitivity of surface coil, and partial volume that a voxel contains to multiple tissue types (Roy et al., 2013). For example, the sensitivity of the surface coil may affect the tumour's appearance in the image and provide different intensities for the same tissue.

Despite extensive and promising work in the tumour segmentation field, obtaining accurate and reliable segmentations of tumours remains a difficult task. Segmentation techniques can be grouped into two main types: supervised and unsupervised.

3.3.1.1 Supervised method

Supervised approaches are based on the extraction of the features from the images such as voxel intensity, histogram, and texture, to create a model based on the relationships between each feature. Generally, the supervised classification procedure is comprised of two main stages: training and testing. In the training stage, the model learns from the information, fed by an expert, to discriminate between different tissue classes. In the testing stage, the dataset being tested is fed to the trained model. The MR image voxels are then assigned to one of the classes.

Supervised methods strongly depend on prior information (training data) to perform the segmentation. This information is generally extracted using an expert's knowledge, (manual selection) which is time consuming, and high (intra- and inter-) observation rate variability might induce errors in the training data. The most common supervised method used in the medical image field is Support Vector Machines (SVM).

3.3.1.2 Unsupervised method

These methods do not require training data to perform segmentation. Most of these methods employ clustering techniques to separate the voxels into different

clusters or classes based on similar features. Some popular unsupervised methods are k-means, Fuzzy c-Means (FCM) and the Gaussian Mixture Model.

3.3.1.3 Gaussian Mixture Model

The Gaussian Mixture Model (GMM) makes an estimation of the Gaussian distribution of each class in the dataset. The GMM for a particular class can be found as follows:

$$f(x) \quad = \sum_{i=1}^{k} P_i N(x/\mu_i, \Sigma_i) \qquad \text{Equation 3.9}$$

Where x is data, k is the number of classes and P_i is the probability of Gaussian component i. N is the probability density function of the Gaussian component of k that can be found from the formula:

$$N(x/\mu_i, \Sigma_i) = \frac{1}{(2\pi)^{\frac{d}{2}} |\sum_i|^{0.5}} e^{-\frac{1}{2}(x-\mu_i)\sum^{-1}(x-\mu_i)} \qquad \text{Equation 3.10}$$

$$= \phi(X; \mu_i, \Sigma_i)$$

Where u_i is the mean and Σ_i is the covariance matrix.

Expectation-Maximization (EM) is a method to find the maximum likelihood or Maximum a Posteriori (MAP) estimator of parameters of the Gaussian mixture φ (u_i, Σ_i and P_i). The EM algorithm is an iterative method to calculate the maximum likelihood or maximum a posteriori estimates of parameters in statistical models, where the model depends on unobserved hidden variables.

EM is demonstrated in the following steps. In the First step, the Mean (m_k) and covariance matrix (Σi) are calculated. The second step, called the E step, calculates the membership probability of the training data. The third step, called the M step, computes the mean and STD of each Gaussian component using the membership probability obtained in the E step. The E and M steps are repeated

until the convergence Gauss mixture vector of each class is obtained by EM and training data for that class (Balafar et al., 2010). Figure 3.5 shows application GMM (built-in MATLAB function) on mouse tumour brain after being selected manually with 2 and 3 clusters.

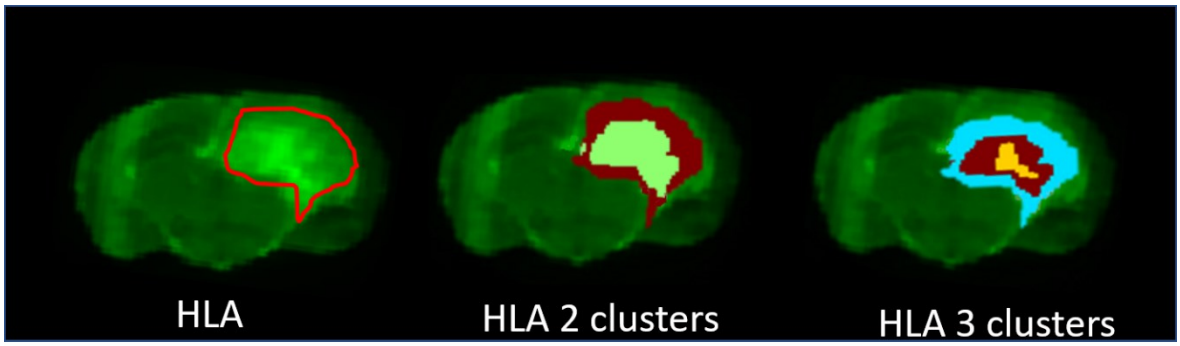

Figure 3.5: (A) HLA section with tumour selection (B) After applying GMM into tumour region with two clusters. (C) After applying GMM into tumour region with three clusters.

3.3.2 Registration

Image registration is a process of aligning several images to ensure corresponding pixels are at the same position in all images. Registration is a necessary step that allows the combination of several images from different modalities to extract more information (Suri et al., 2005). For example, registration can be applied between PET and MRI or CT with PET.

3.3.2.1 Transformation model

The goal of the registration process is to find a Transformation Model (TM). This describes how the image will be deformed and the amount of deformation allowed. It maps the coordinates of a particular pixel from the moving image (B) to be registered to the coordinates of the corresponding pixel in the fixed image (A). It is written as follows:

$$B(x', y') = TM.A(x, y) \qquad \text{Equation 3.11}$$

The most common image transformation models are rigid and affine (Maintz and Viergever, 1998). Figure 3.4 shows different types of these models. The rigid

transformation is the simplest transformation model (Fig.3.6A-B). It allows only rotation and translation. Affine registration allows scaling and shearing in addition to translation and rotation (Fig.3.6C).

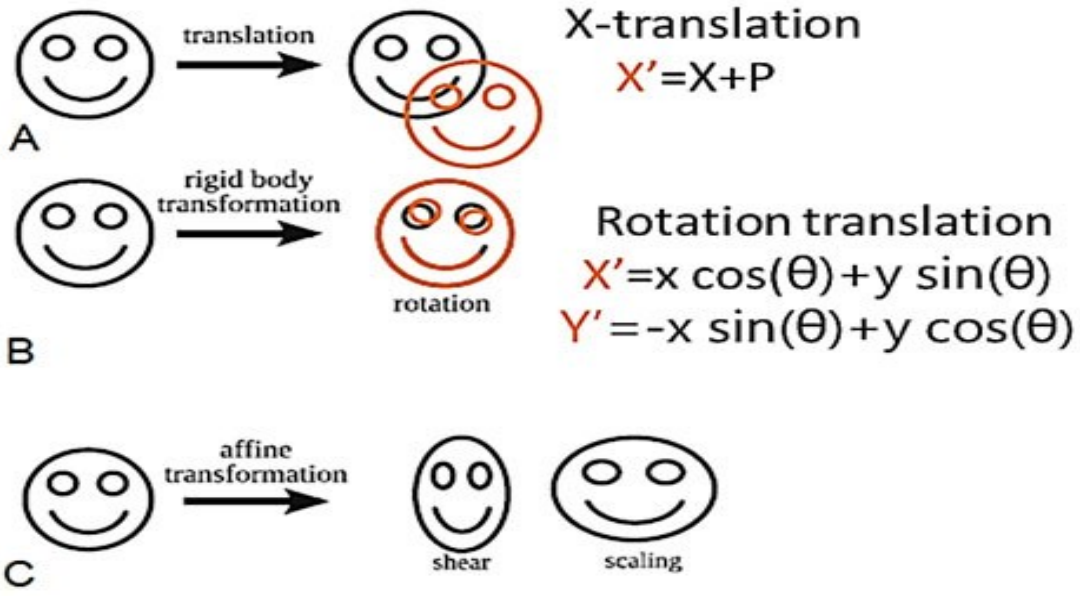

Figure 3.6: (A) Linear translation and P constant parameter, (B) Rigid transformation with rotation (C) Affine transformation. Adapted from (Kiessling and Pichler, 2011).

One example of the translation model is rotation. Let us assume pixel coordinate A(x,y) under geometric distortion produces an image with coordinate B(x',y').

$$TM = \begin{bmatrix} x' = x\cos\theta + y\sin\theta \\ y' = -x\sin\theta + y\cos\theta \end{bmatrix} \quad \text{Equation 3.12}$$

Where B is the image after rotation with angle θ, A is the original image and the translation model is TM.

3.3.2.2 Mutual information method

The relationship between intensities in the two images can be obtained by plotting their 2-D histogram. Plotting this histogram for identical images will generate a straight line. As one image is spatially transformed with respect to the other, the points on the histogram will start to scatter (Fig.3.7).

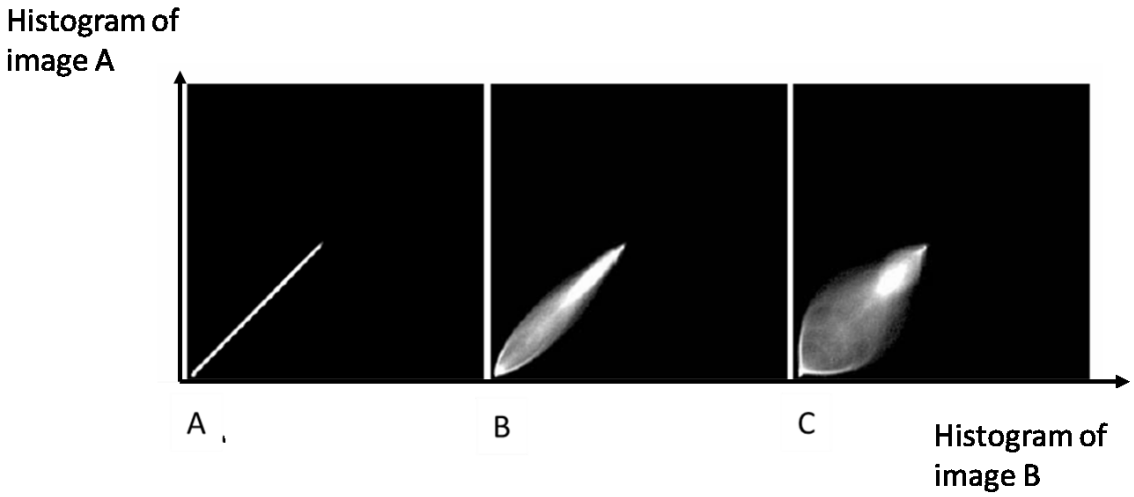

Figure 3.7: 2-D histograms of grey levels for two images are where (A) identical (B-C) with small translation. Adapted from (Hill and Hawkes, 1994).

3.3.2.3 Entropy

Entropy (H) is the measure of uncertainty of a random variable. This uncertainty is related to the probability of the occurrence of the event. If the entropy is high, the events have probability of occurrence, otherwise, the events have a low probability of occurrence. The entropy of variable x is defined as:

$$\mathrm{H(x)} = -\sum_{\mathrm{i}}^{\mathrm{N}} \mathrm{P(i)} \log_2 \mathrm{Px(i)} \qquad \text{Equation 3.13}$$

P_x the probability distribution of x, can be determined by the normalized histogram of the image. Let H (A), H (B) and H (A, B) be the entropy of two images A and B and the joint entropy of two images, respectively. These entropies can be expressed mathematically as (Vergara and Estévez, 2013):

$$H(A) = -\sum_{i}^{N} \mathrm{Pa(i)} \log_2 \mathrm{Pa(i)} \qquad \text{Equation 3.14}$$

$$H(B) = -\sum_{i}^{N} \mathrm{Pb(i)} \log_2 \mathrm{Pb(i)} \qquad \text{Equation 3.15}$$

$$H(A,B) \quad = -\sum_{i}^{N} \sum_{j}^{N} \mathrm{Pab(i,j)} \log_2 \mathrm{Pab(i,j)} \qquad \text{Equation 3.16}$$

Where N is the number of different possible greyscale values that i and j can take ,P_{ab} (i, j) is the joint probability of the MRI and histology.

Here, the entropy of the two images used to compute the joint entropy, is represented as mutual information (MI).

$$\mathrm{MI(A,B)} = \mathrm{H(A)} + \mathrm{H(B)} - \mathrm{H(A,B)} \qquad \text{Equation 3.17}$$

Mutual Information (MI) has been widely used for medical image registration and is the most commonly used multimodal registration criterion. MI based registration begins with the estimation of the joint probability of the pixel intensities of corresponding pixels in the two images.

MI was used as a measure of statistical correlation of two random variables. Given an image A and B, the mutual information of A and B is defined as:

$$\mathrm{MI(A,B)} = \sum_{\mathrm{i,j=1}}^{\mathrm{N}} \mathrm{P(a,b)} \,.\log_2 \frac{\mathrm{Pab(i,j)}}{\mathrm{Pa(i).Pb(j)}} \qquad \text{Equation 3.18}$$

Where P(a,b) marginal probability distribution P_a and P_b.

Registration using the mutual information method depends only on the information contained within the image, which does not need any prior medical knowledge. Also, the value of MI represents the measurement of similarity between image A and B (MI=1 best similarity).

3.4 Histology

The word ‘Histology’ first appears around 1819. It derives from the Greek words ‘hystos’ and ‘logos’, meaning tissue and study or science. Histology is the microscopic inspection of tissue sections, usually on glass slides, which are coloured with different stains to show different functional or physical properties

(McCann, 2015). In fact, histology is considered the gold standard for several diseases, such as GB. The process to make a histology section can be seen in Fig. 3.8.

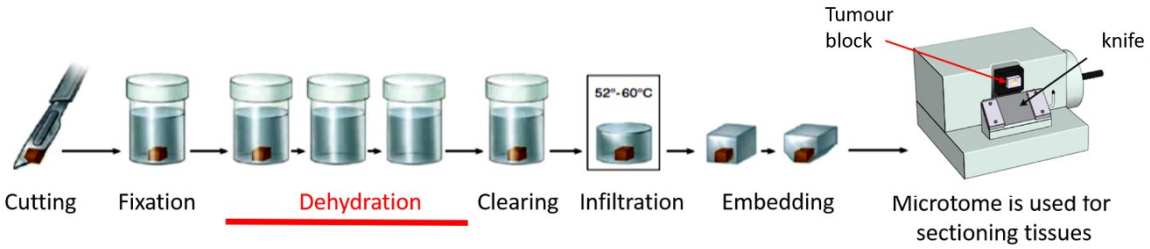

Figure 3.8: Diagram shows the basic steps used in tissue preparation for light microscopy. Adapted from (Mescher, 2016).

In preparation of histological sections for microscopic observation, tissues and organs are too provide sections of reduced thickness to allow the passage of a light beam. Thus, in most of the cases, tissues are sliced into thin sections (from 10-20 μm) and are placed on glass slides before being examined (Szende and Suba, 1999). For better visualization of the cells, pathologists often add stains, such as Haematoxylin and Eosin (H&E), Fig.3.9.

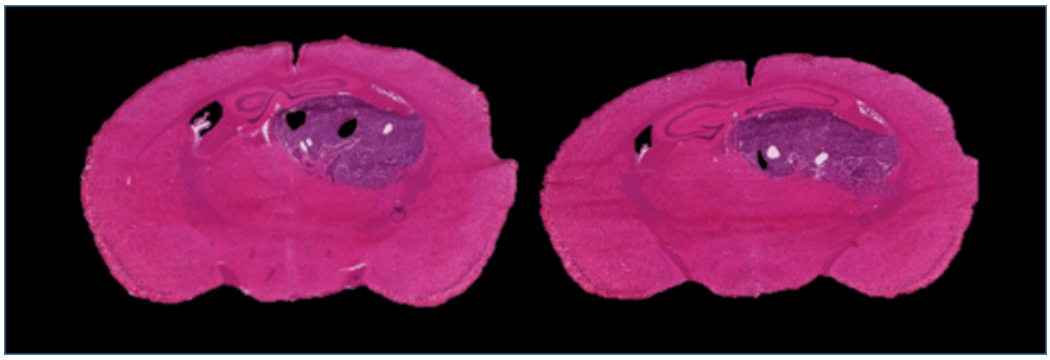

Figure 3.9 Examples of mouse brain histological sections stained with H&E, with tumour in right hemisphere.

Tissue too delicate for direct sectioning by using a vibrating blade, so it is most commonly either embedded in a hardening material such as Paraffin and sectioned using a microtome or frozen and sectioned in a cryostat (a microtome inside a freezer), (Pichat et al., 2018). For the fresh freezing method, the tissues should be frozen as rapidly as possible to avoid ice crystals and formation of amorphous ice. Freezing tissues slowly causes the water molecules during the transition to

form crystals, which results in volume expansion with destruction of cell membranes and disconnection of the tissue, see Fig.3.10.

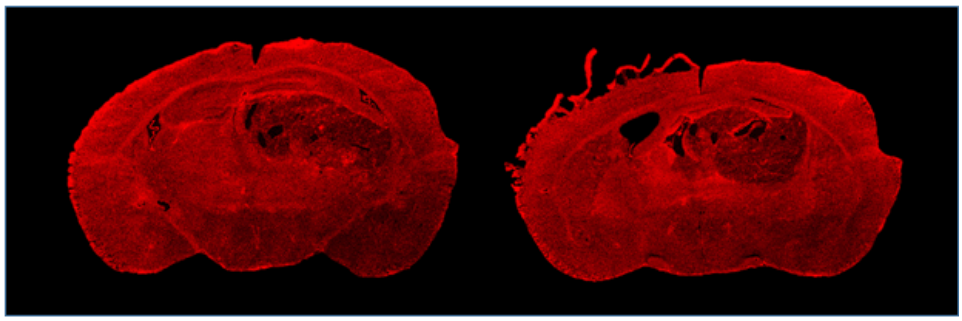

Figure 3.10: Example of sections obtained using the fresh freezing method and stained with Human Leukocyte Antigen (HLA).

3.4.1 Pre-processing histology

Staining variations affect the appearance of histology images. Such variations are problematic for automated analysis because colour is a critical feature in histology (Gurcan et al., 2009). Stain normalization is the process of taking two H&E images that have staining variation between them and removing this variation. This process consists of transforming the discrete distribution of pixel intensities into a discrete distribution of probabilities (histogram), dividing each value of the histogram by the number of pixels, and normalizing each colour according to shapes of specific histograms (Gonzalez and Woods, 2002). This process allows for regions of lower local contrast to gain a higher contrast.

Colour normalisation/correction by histogram has shown improvement of histopathological image quality (Roy et al., 2018, Bhattacharjee et al., 2014). The advantage of this method is that both source and target images are the same brightness. However, this method is not applicable if the source and the target image have large differences in their histograms (Gonzalez and Woods, 2002). Software that corrects colour variation has become a standard package provided by most microscope manufacturers (Gurcan et al., 2009).

3.4.2 Post-processing histology

Registration of a histology image with MR images is typically challenging due to a significant variation in image properties such as resolution, field of view, and contrast (Madabhushi et al., 2005). Registering histology images to MR images could help, for example, train radiologists, improve non-invasive diagnoses, and enable the development of MRI-based Computer-Aided Diagnosis (CAD) tools.

3.5 Validation measurement

The validity of segmentation or registration is an important matter in medical image analysis because it may have a direct impact on diagnosis and therapy plans. There are two types of validation: qualitative and quantitative. In this work, three validation methods, namely, visual assessment (qualitative), Dice Similarity Coefficient and ROC analysis (quantitative) were used.

3.5.1 Visual assessment

One of the quickest validation methods is simple visual inspection of the results. However, such qualitative assessment requires experience in comparing brain structures between MRI and histology. For more details see Fig.3.11.

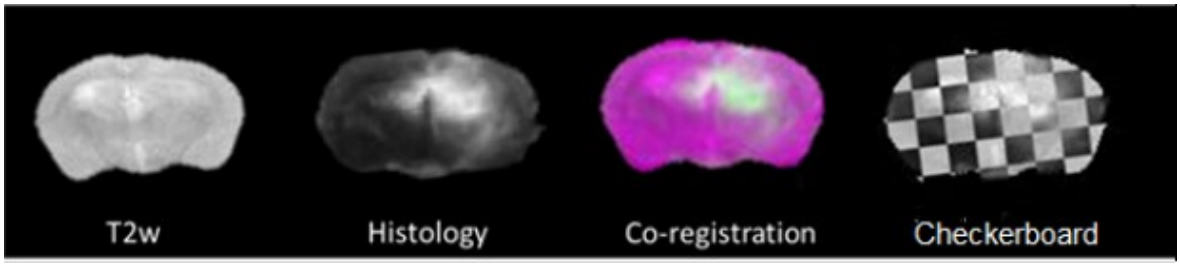

Figure 3.11: Visual assessment by checkerboard after co-registration of MRI with histology.

3.5.2 Dice similarity coefficient

The most widely employed technique to evaluate the accuracy of segmentation is the similarity index or Dice Similarity Coefficient (Dice), (Dice, 1945). The value of Dice varies between 0 and 1 (perfect segmentation), with 0.7 representing the position of good segmentation. However, Dice does not provide information about regions and it is sensitive to the total Region of Interest (ROI) and size distribution of the ROI (Garcia-Lorenzo et al., 2013).

$$\text{Dice} = \frac{2\,A \cap B}{A \cup B} \qquad \text{Equation 3.19}$$

Figure 3.12 where A and B are two regions of interest. For example, MRI and histology,

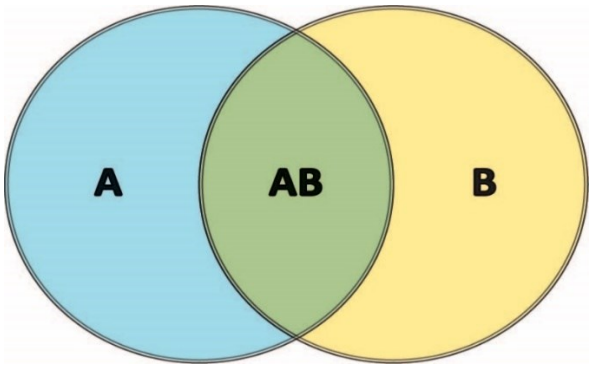

Figure 3.12: The Dice method is used to assess the intersection (overlap) between two regions A and B.

3.5.3 ROC analysis

Receiver Operating Characteristic (ROC) curve analysis is used to compare abnormal regions of interest probed by different modalities, such as MRI and histology, ground truth,(Garcia-Lorenzo et al., 2013). A comparison of abnormal regions gives measurements of True Negative (TN), False Positive (FP), False Negative (FN) and True Positive (TP) used to calculate sensitivity, specificity accuracy, and Dice (see Fig.3.13).

$$\text{Sensitivity} = \frac{TP}{TP + FN} \qquad \text{Equation 3.20}$$

$$\text{Accuracy} = \frac{TP + TN}{TP + +FP + FN + TN} \qquad \text{Equation 3.21}$$

$$\text{Specificity} = \frac{\text{TN}}{\text{TP} + \text{TN}} \qquad \text{Equation 3.22}$$

$$\text{Dice} = \frac{2 * \text{TP}}{\text{FP} + \text{FN} + 2 * \text{TP}} \qquad \text{Equation 3.23}$$

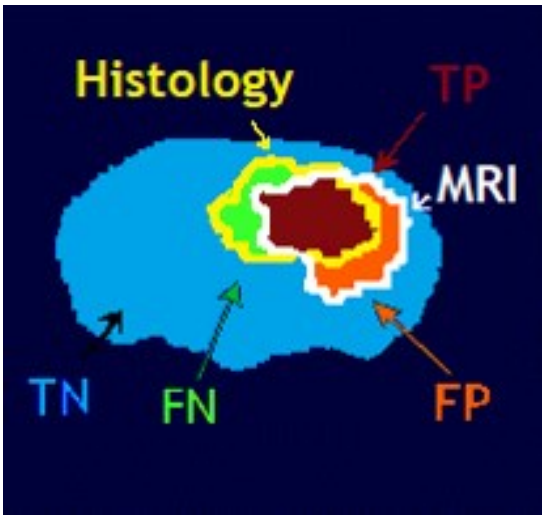

Figure 3.13: Diagram of comparison of two regions. If we consider the region outlined by the yellow contour is histology compared of the region outlined by white contour, which is MRI, the interaction of the two regions divides the space into four regions: true positive (TP), true negative (TN), false positive (FP) and false negative (FN).

3.5.4 Reproducibility

Repeated measurements using a specific method should give identical results. However, variations exist which may be both equipment-dependent and operator-dependent. Reproducibility refers to the ability of a method to be repeated to achieve similar results, and measures the variability that exists between repeated measurements (Garcia-Lorenzo et al., 2013). A reproducible imaging measure should, thus, be independent of scanner, MRI centre and time-point. Reproducibility in this study was measured using the Coefficient of Variation (CV) as follows:

$$CV = \frac{\sigma}{m}$$ Equation 3.24

Where m is the mean σ and is the standard deviation of the different measures of total lesion load. A small value of CV means less variation between two measurements.

Chapter 4

Material and Experimental Methods

4.1 Animal study design

4.1.1 Mice and tumour implantation

Ten CD1 nude mice (20-25 g, Charles River Laboratories) were acclimatized at least 2 weeks prior to any experimental procedure. G7 human glioblastoma cells were cultured in stem-like conditions (Advanced DMEM: F12, containing 20 μM EGF/FGF, 1% B27, 0.5 %N_2, heparin, 1% L-Glut) on matrigel coated plates. The animals were intracranially injected with G7 cells (10^5 cells per mouse) using stereotactic equipment. This model is rich in stem cells and highly infiltrative in the edge of the tumour, see Fig.4.1 (Gomez-Roman et al., 2017).

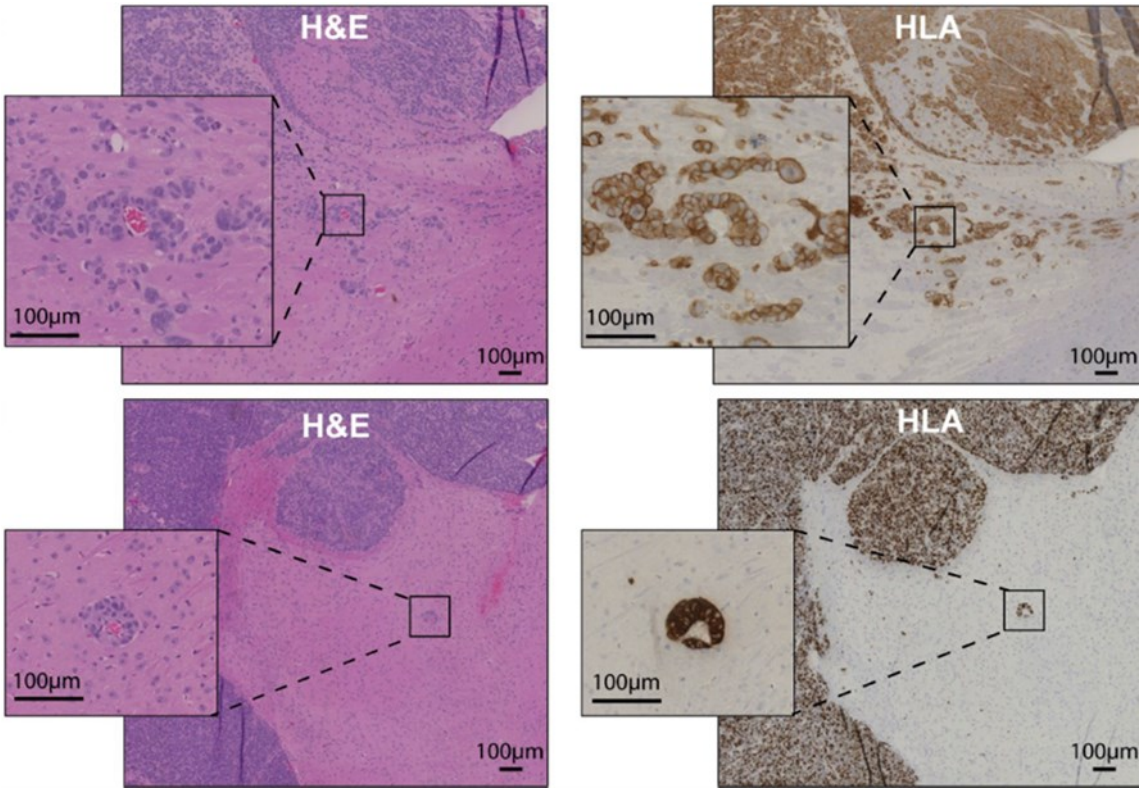

Figure 4.1: Tumour margin of G7 glioblastoma model samples with the brains stained for H&E and HLA. Regions of vascular cuffing by invading tumour cells are enlarged. Reprinted with permission (Vallatos et al., 2018a) .

For an addition group of animals (n=5), anesthetized mice received an intravenous injection of 0.1 ml 7.5 mg/ml 70 kDa Texas red-labelled dextran (Thermo Fisher Scientific, UK) in Phosphate-Buffered Saline (PBS), for subsequent brain perfusion analysis.

4.1.2 Experimental design

The mice were scanned in week 9 and week 12 (Fig.4.2). After the final MRI session, animals were humanely killed and the brains were quickly removed for histology.

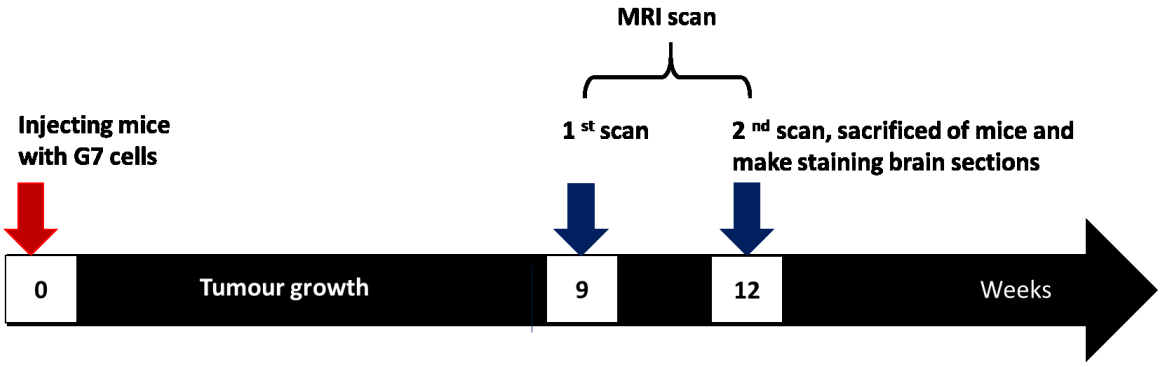

Figure 4.2: Experimental protocol. At week zero, 10 mice were orthotopically implanted with G7 glioblastoma cells. Mice were imaged in week 9 and week12. After the last MRI session, mice were sacrificed and prepared for histology.

Four additional animals were scanned at weeks 12, 15, and 17 to allow the formation of a necrotic core (Fig.4.3). Following MRI, the animals were sacrificed and their brains were freezed to minimize microscopic deformation of cells to allow for histology analysis.

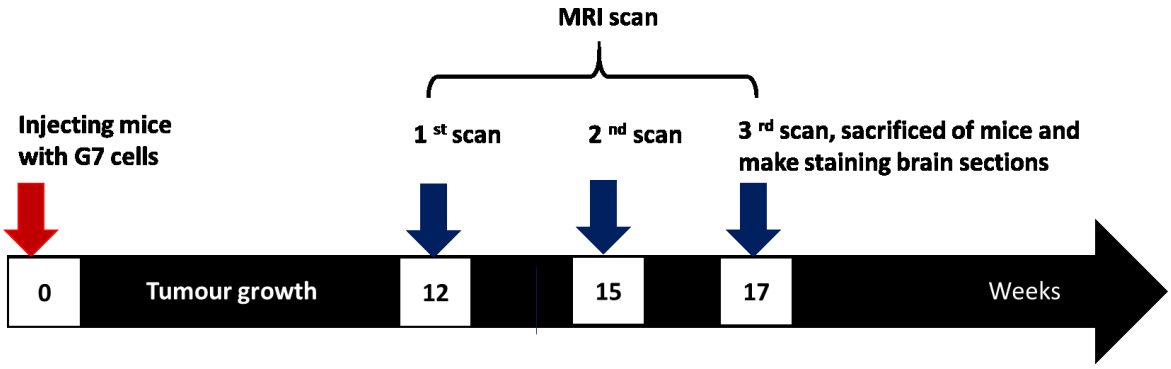

Figure 4.3: Experimental protocol of second study. At week zero, four mice were orthotopically implanted with G7 glioblastomacells. Mice were imaged in week 12, 15 and 17. After the final MRI session, mice were sacrificed and prepared for histology.

All experiments were carried out in accordance with the local ethical review panel, the UK Home Office Animals (Scientific Procedures) Act of 1986, and the

United Kingdom National Cancer Research Institute guidelines for the welfare of animals in cancer research (Workman, 2010).

4.1.3 MRI acquisition

MRI experiments were performed on a Bruker Biospec Avance 7 T imaging system with a 30 cm horizontal bore (Bruker, Ettlingen,Germany), Fig.4.4. Homogeneous RF excitation was achieved using a birdcage volume resonator (diameter = 72 mm, length = 110 mm). An actively decoupled 4-channel phased array receive-only head surface coil was used for signal detection (Rapid Biomedical, Wurzburg, Germany). The system was equipped with shielded magnetic field gradients producing up to 400 mT/m. The animals were anaesthetized using 5% isoflurane and a 30:70 O_2/N_2O ratio before being positioned prone on an MRI animal cradle. A hot water circulation jacket was used to regulate physiological temperature (37 ± 1 °C) and body temperature was monitored using a rectal probe. The head was secured laterally by conical ear rods and longitudinally by the nose cone used for anesthetic gas delivery. The animals breathed through a face mask, with isoflurane delivered at a constant flow mixed in a 40:60 ratio of O_2/N_2O (1 L/min). Isoflurane concentration was varied (1.5–3%) in order to maintain stable respiration rates within normal physiological ranges (40–70 bpm). Respiration was monitored using a pressure sensor connected to an air-filled balloon placed under the animal abdomen (Biotrig Software, Bruker).

Figure 4.4: Bruker Biospec 7 Tesla MRI scanner with a 30 cm horizontal bore and the equipment used for preclinical experiment in GEMRIC.

Following a geometry-locater, a series of MRI experiments were performed (field of view 2 × 2 cm, five 1.5 mm coronal imaging slices centred at 4 mm posterior from rhinal fissure).

T2-Weighted imaging was performed using an acquisition with Multi Slice Multi Echo (MSME) sequence (echo time TE = 47 ms, repetition time TR = 4,300 ms, matrix = 176 × 176, NA=4, 15 echoes, slice thickness = 1.5 mm, scan time 9 min), Rare factor=8. Higher-resolution $T2W_{histology}$ images (slice thickness = 0.5 mm) were acquired during the final scanning session with MSME sequence (echo time TE = 46 ms, repetition time TR = 4,314 ms, matrix = 176 × 176), Rare factor=8.

Diffusion weighted imaging (DWI) was performed using a 4-shot spin-echo planar imaging DW scan (TE = 37 ms, TR = 4,500 ms, matrix = 128 × 128, 1.5 mm slice thickness, 6 directions, b-values = 0, 1000 s mm^{-2}, scan time 10 min).

Perfusion weighted imaging (PWI) was performed using an optimized multiple boli arterial spin labelling sequence (mbASL), (Vallatos et al., 2018b), labelling with a train of 20 hyperbolic-secant inversion pulses (duration = 3.3 ms, dimensionless amplitude parameter μ = 8, angular modulation β = 760 s^{-1}) evenly distributed over 5 seconds with a post labelling delay of 50 ms. The inversion slice width was 8.5 mm and the offset from the imaging slice was 15 mm. Image acquisition was achieved with a 4-shot EPI module (TE = 12 ms, TR = 7 s, matrix = 96 × 96, partial FT = 1.4, 12 averages, scan time 9 min).

Contrast-Enhanced T1 imaging (CE-T1) was performed using a RARE acquisition (TE = 12.3 ms, TR = 800 ms, NA=4, Rare Factor=4, ms, matrix = 176 × 176, 8 min). A catheter was inserted into the tail vein, allowing the injection of a contrast agent without removing the mouse from the magnet. Images were acquired before and 5 minutes after gadolinium-DTPA injection). Following *in vivo* scanning, a doped water phantom was scanned, for use in correcting the receiver coil bias (Rapid Acquisition with Relaxation Enhance), RARE, acquisition, TR=7000 ms, TE=46 ms, 18 slices, slice thickness=0.5 mm, matrix size=176x176, 128x128 and 96x96, NA=20). For more details see Fig.4.5 and Fig.4.6.

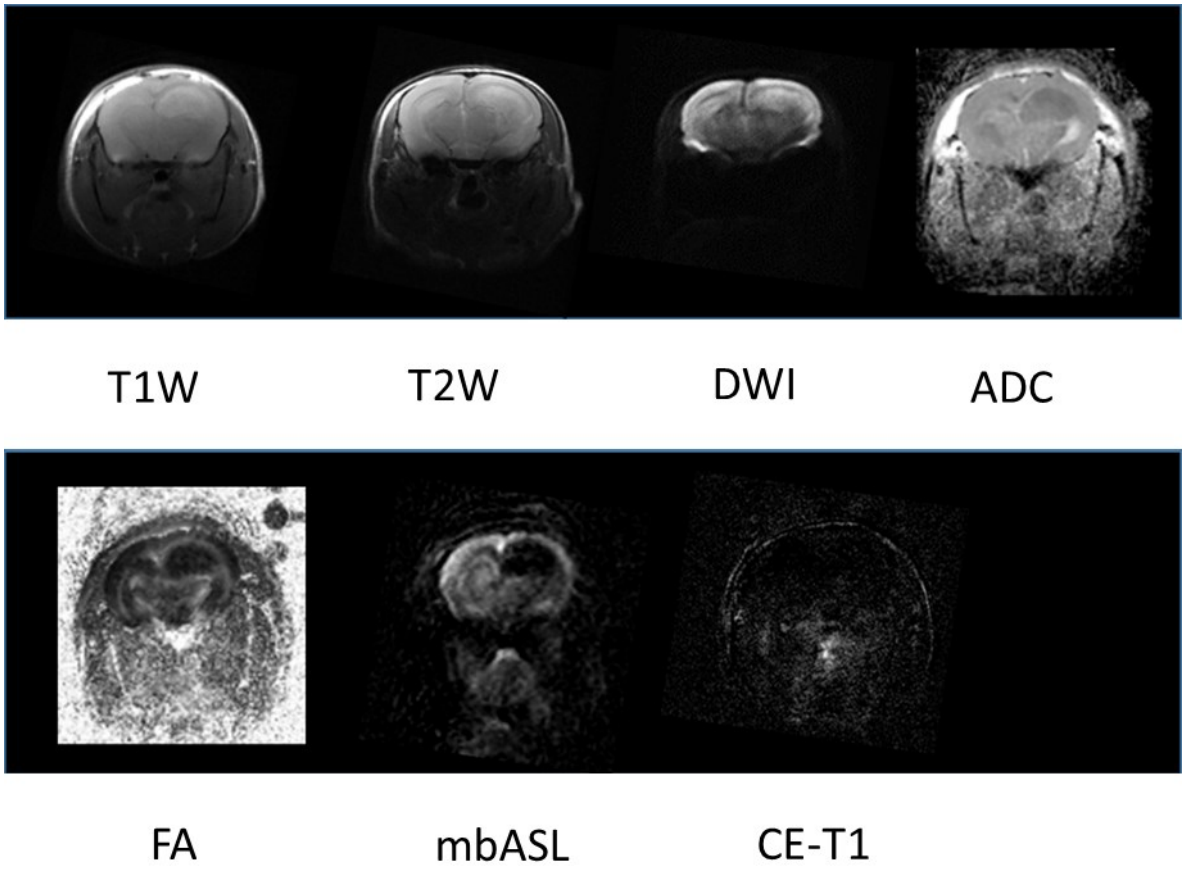

Figure 4.5 Examples of different MRI modalities from first experiment on GB infected mice at week 12. The tumour appears to not have a necrotic core nor a contrast enhance rim.

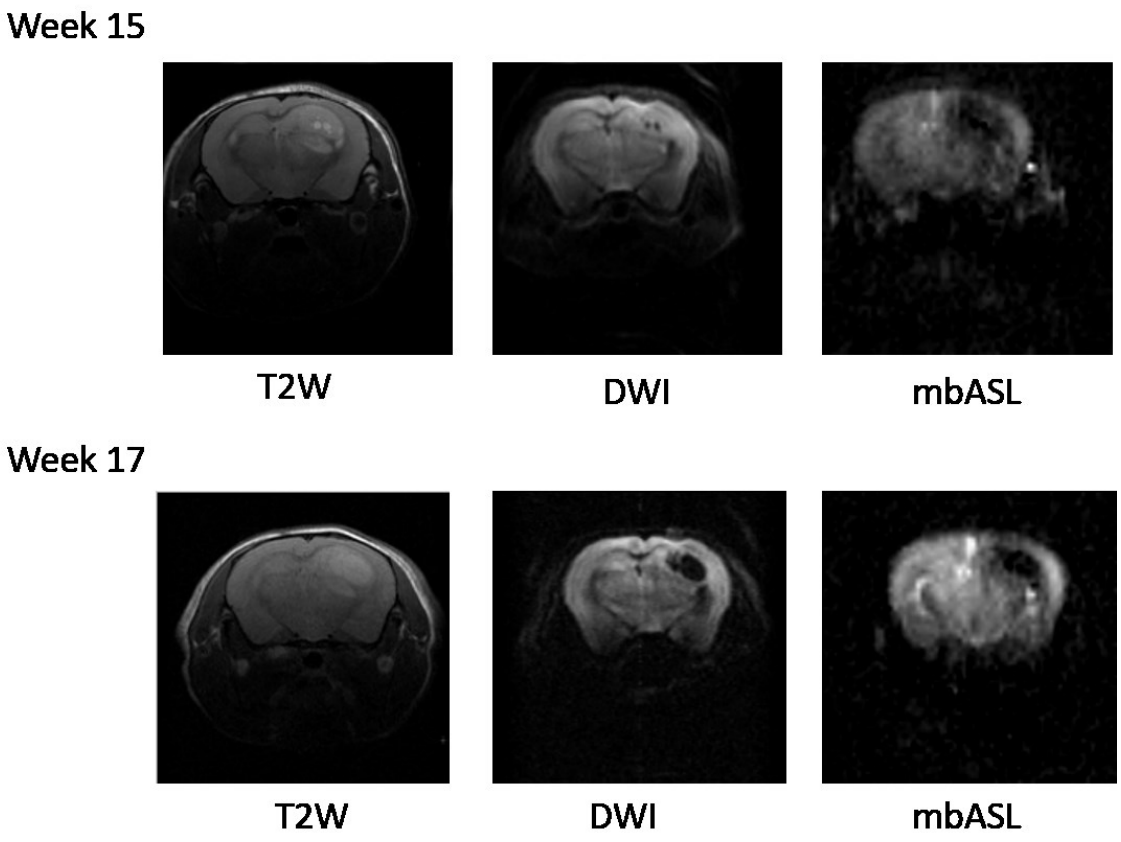

Figure 4.6: Example of MR images of second experiment on GB mice at week 15 and 17 post infection. The tumour has a necrotic core.

4.1.4 Histology protocols

Following the final MRI last session, anesthetized mice received an intravenous injection of 0.1 ml 7.5 mg/ml 70 KDa Texas red-labeled dextran (Thermo Fisher Scientific, UK) in phosphate-buffered saline (PBS), for subsequent brain perfusion analysis. Two minutes after injection, mice were sacrificed and their brains were removed and fresh-frozen in liquid N_2. Brain slicing was performed manually on an OTF 5000 Bright cryostat, guided by the high-resolution $T2W_{histology}$ images. The identification of common anatomical features by an experienced neuroscience research technician (L.G., 20 years' experience) allowed positioning the sectioning plane parallel to the MRI plane. Interleaved 20 µm and 60 µm sections were cut. The 20 µm cryosections were fixed in ice-cold acetone and washed in PBS before blocking in 3% BSA/TBS/0.05% Tween for 30 minutes at room temperature. A 1:500 dilution HLA antibody (Abcam, Cambridge, MA; ab70328) in blocking buffer was added and incubated for 2 hours at room temperature. Sections were washed three times with TBS-Tween before addition of 1:1000 antimouse Alexa 647-conjugated secondary antibody (A-21236, Thermo Fisher

Scientific) for 1 hour incubation in the dark. Sections were washed three times with TBS-Tween and mounted in ProLong Diamond Antifade mount with DAPI (P36966, Thermo Fisher Scientific). Eiess 710 upright confocal microscope at x10 magnification (Far red filters 638-747 nm, Beam splitters-MBS: MBS 488/561/633, MBS_InVis:plate, DBS1:Mirror).

Sections were stained for hematoxylin and eosin (H&E), Ki67, or incubated with 1:500 dilution HLA antibody (Abcam ab70328) and visualized using DAB staining (Dako EnVision + System HRP [DAB] K4007) followed by counterstaining and mounting. Sections were imaged using a Hamamatsu (Bridgewater, NJ) Nanozoomer Slide scanner with Leica Slide Path imaging Software (J.B., 8 years' experience) or tiling at ×10 on a Zeiss (Thornwood, NY) 710 upright confocal microscope. For dextran imaging, unfixed 60-μm cryosections were imaged by zstack tile scanning on a Zeiss 710 upright confocal microscope. Images were exported as '.tiff'.

Chapter 5

Stacked In-plane Histology for Quantitative Validation Application to an infiltrative Brain Tumour Model

5.1 Introduction

The use of non-invasive imaging modalities for clinical diagnosis continues to advance rapidly. A variety of methods are now available including Magnetic Resonance Imaging, Positron Emission Tomography (PET), Single Photon Emission Computerised Tomography (SPECT), Ultrasound (US), and X-ray Computed Tomography (X-ray CT). Often, the source of image contrast is related only indirectly to the underlying biology. This is especially true for MRI, where the signal intensity can depend upon many physical parameters including water content, local structure, tumbling rates, diffusion, and hypoxia (Dominietto et al., 2015). There has been considerable interest in identifying whether such biologically indirect image contrasts can be used as non-invasive imaging biomarkers, either for normal biological functions, pathogenic processes or pharmacological responses to therapeutic interventions (Atkinson et al., 2001).

Histopathology is generally considered to be the ground truth when considering the characterisation of diseased tissue (Kiessling and Pichler, 2011). For histology, a post mortem or biopsy specimen is cut into thin sections to reveal its internal morphology and then stained to observe complex differentiated structures at the cellular level (Kiessling and Pichler, 2011). The cutting process inherently yields 2D sections, which is the manner by which most histology is analysed. However, considerable work has been undertaken to reconstruct 3D histological volumes from serial 2D sections (Pichat et al., 2018). Though difficult, this allows knowledge of the 3D environment to be regained, while still accessing microscopic information (Stille et al., 2013).

When new imaging modalities are proposed as imaging biomarkers for particular diseases (Price and Gillard, 2011), it is difficult or impossible to validate them in human patients for ethical reasons. Validation against histopathology is limited to biopsy (Madabhushi et al., 2005) and later post-mortem comparisons (Kimt et al., 2000). In the case of biopsy, the size and number of samples taken is very limited and difficult to localise on images. Comparison of *in vivo* non-invasive imaging and later post-mortem histology would be compromised by disease progression between imaging and death. Further, comparison of post-mortem imaging and post-mortem histology, would be compromised by the *ex vivo* state of the tissue (Fagan et al., 2008).

Nevertheless, biomarker validation can be performed in preclinical disease models, where the animal can be terminated immediately following imaging for histological analysis. In principle, co-registration of imaging biomarkers with histopathology would allow direct validation. Indeed, there is a considerable literature describing such image registration algorithms and their application (Dauguet et al., 2007, Pichat et al., 2018). However, in practice, most preclinical validation is qualitative, limited to visual comparisons with sample histology sections, with little attempt made to match these to the corresponding imaging slice (Henning et al., 2007, Langer et al., 2009, Coquery et al., 2014). The reason for this is that accurate co-registration of non-invasive images with histology sections is challenging. The processing, cutting and staining of histology sections can result in complex deformations such as fixation shrinkage, tears and cutting artefacts (Stille et al., 2013, Agarwal et al., 2016), which are difficult for registration algorithms to handle.

Examples of quantitative comparison of imaging biomarkers with histology include Stille et al. (2013), which used rigid registration and selected anatomical landmarks with a rodent stroke model. This approach requires an expert to identify the control points, which can be a difficult task due to internal distortions. Similarly, Ou et al. (2009) used non-rigid registration with selected anatomical landmarks to register histology to MRI of prostate tumours, using two criteria: maximization of landmark similarities and maximization of cancer region overlap. Jardim-Perassi et al. (2019) used MRI-guided 3D printed tumour moulds to facilitate registration in a murine breast tumour model. However, the accuracy of these approaches was limited by not accounting for imaging slice thickness and often slice orientation too.

In this chapter, we have tried to achieve high quality registration of histology with non-invasive imaging data, not by improving on current image registration algorithms, but by focusing on improving the quality of the histology used. This was done in five ways:

1. The use of a ‘flash-freeze’ method for fixation instead of transcardial fixation with paraffin embedding. With care and experience this helps to preserve tissue morphology, reducing macroscopic distortions associated with extracting, cutting, and staining (Peters, 2003, Ou et al., 2009).

2. Histology was cut in relatively thick 20 µm sections, to reduce the risk of tears/distortions.

3. Histology sections were carefully cut in the image acquisition plane (e.g. the MRI plane), guided by high resolution thin slice (Thickness=0.5 mm) $T2W_{histology}$ MRI. This is particularly important to maximise spatial correlation between MRI and histology (cf. Fig.5.1). Voxels of an MRI scan in this work are not isotropic, meaning the voxel is not equidistance in all three directions, when there is a different voxel resolution within the MRI slices and there is a gap size between the slices. It is not possible to use a standard histology section as guidance for MRI slice selection.

4. A protocol was developed to register and stack multiple in-plane histology sections in order to reflect the imaging slice thickness. For example, the thickness of an MRI slice (~1-2 mm) is approximately 100 times thicker than a histology section (~10 to 20 µm) (cf. Fig.5.2). This is crucial where the pathology is heterogeneous, with variations occurring on the length scale of the imaging slice thickness.

5. The use of histological stains that exhibit signal intensities proportional to the observed phenomenon, in order to produce semi-quantitative maps. This facilitates intensity based registration, thus avoiding overfitting limitations of commonly used affine transformations (Wells et al., 1996).

To evaluate the ability of this overall approach to provide a quantitative histopathologic assessment of *in vivo* imaging biomarkers, we applied it to a patient-derived mouse model of glioblastoma. In GB, a major factor contributing to treatment failure is the ability of tumour cells to infiltrate adjacent normal brain tissue (Price, 2007), with low tumour cell density extending far beyond the bulk of the tumour. Identifying the full extent of infiltration is important for both radiotherapy planning and to achieve complete surgical resection. Here, we present the different steps leading to the production of a 3D data matrix, from co-registration of multiple MRI modalities with stacked in-plane histology. We show how the resulting matrix allows MRI modalities to be assessed, both in terms of tumour volume detection and via direct voxel-wise comparison. Such an

approach should become the accepted gold standard for validating non-invasive imaging biomarkers.

5.2 Experimental protocol

All mice brains were scanned *in vivo* on week (9 and 12) respectively. Following the experiment, a phantom image was acquired that was used for correcting the sensitivity bias of the RF surface receiver coil. At the end of the MRI session, animals were sacrificed immediately following the last scan and stored frozen at -20 ˚C to enable *ex vivo* studies later.

Following MRI, animal brains were removed and fresh-frozen for 2 minutes at -45 ˚C using an isopentane solution tube immersed into dry ice. The frozen brain was then removed from the isopentane, embedded in Cryomatrix and protected in M-1 embedding matrix to prevent dehydration (Thermo Fisher Scientific, UK). Freezing was favoured in order to avoid the unpredictable macroscopic tissue deformation related to perfusion-fixation and paraffin embedding (Petersen et al., 2001). Brain slicing was performed manually on an OTF 5000 Bright cryostat (-16 ˚C) equipped with a rotary knife (Bright, Criostato-OTF-5000). A relatively thick section thickness of 20 μm was chosen, to reduce the risk of tears or distortions. Care was taken to cut the sections in planes parallel to the MRI image ones. For this, sectioning was guided by high resolution T2W images (slice thickness = 0.5 mm, $T2W_{histology}$) Common brain structures identified by an experienced neuroscience research technician (L. Gallagher) were used to iteratively orientate the sectioning plane, so as to be parallel to the MRI plane (Fig.5.1). Five sections within the MRI thickness were cut at 300 μm intervals and then lifted onto to poly-L-lysine slides. Then, the sections were stained using either haematoxylin and eosin (H&E) or Human Leukocyte Antigen (HLA) stain to identify the human tumour cells (Fig.5.2). The 20 μm cryosections were fixed in ice cold acetone and washed in PBS 226 before blocking in 3% BSA/TBS-tween for 30 mins at room temperature. A 1:500 dilution HLA antibody (abcam ab70328) in blocking buffer was added and incubated for 2 hours at room temperature. Sections were washed three times with TBS-Tween before addition of 1:1000 anti-mouse Alexa Fluor 647-conjugated secondary antibody (Thermo Fisher Scientific, UK - A21236) for 1hour incubation in the dark. Sections were washed 3 times with TBS-Tween and mounted in 231 ProLong Diamond Antifade mount with DAPI (Thermo Fisher Scientific, UK -

P36966). Whole brain section tile scans were conducted using a Zeiss 710 upright confocal microscope at x10 magnification.

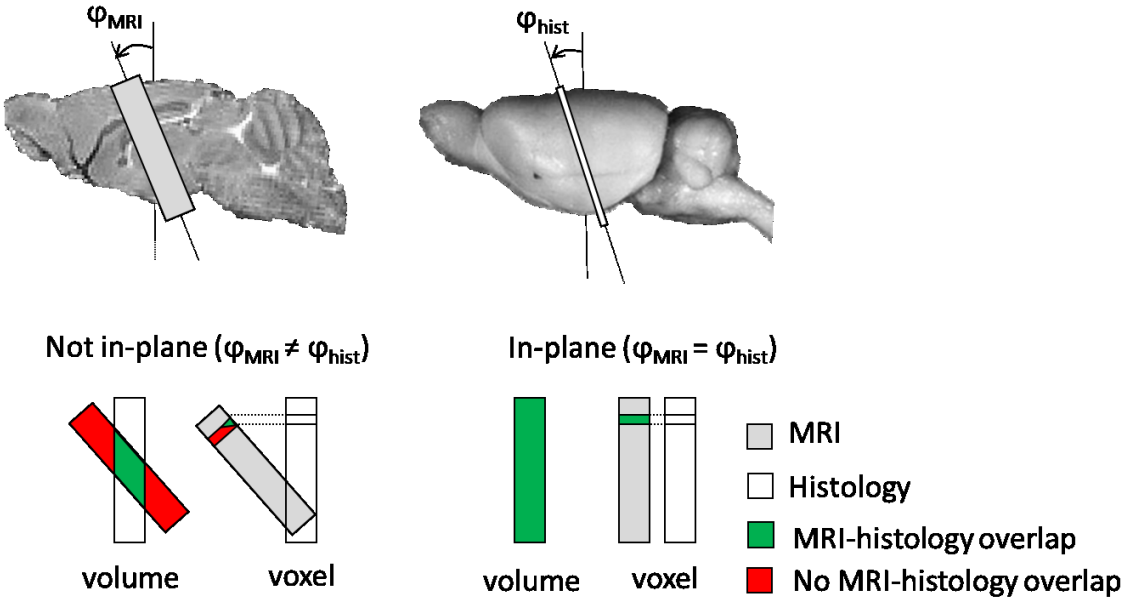

Figure 5.1: Effect of cutting angle (φ) on MRI to histology comparison: (A) MRI (1.5 mm thickness) and histology (20 μm thickness) cutting angles. (B) The effect of cutting angle discrepancies on the overall volume and voxel-wise overlaps between MRI and stacked histology. Reprinted with permission (Al-mubarak et al., 2019).

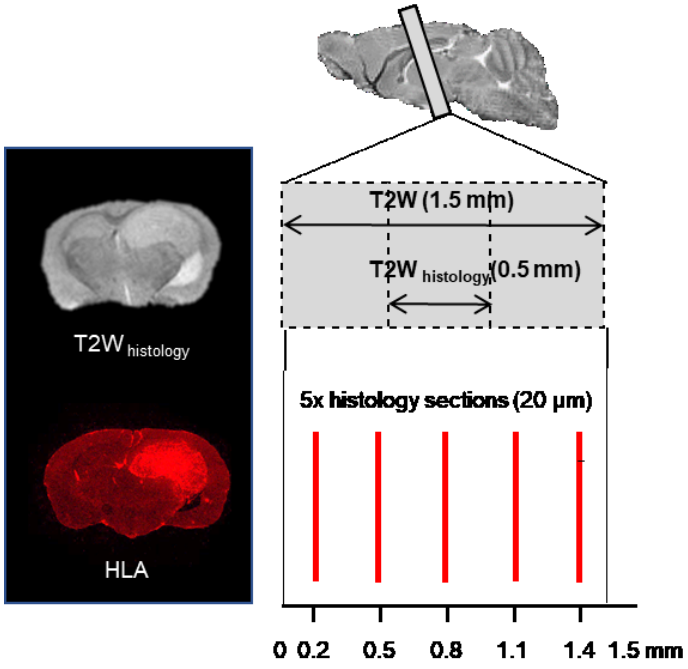

Figure 5.2: The cutting of histology section was guided by 0.5 mm thick T2-Weighted images ($T2W_{Histology}$), matching the cryo-section plane to the MRI acquisition plane. Five evenly distributed histology sections (20 μm) were cut (red) to cover the 1.5 mm thickness of the T2W scans. . Reprinted with permission (Al-mubarak et al., 2019).

5.3 Data processing pipeline

Both MRI and histology data were processed using MATLAB code developed in-house (MATLAB R2015a , MathWorks Ltd., U.K.). The overall processing pipeline is summarised in Fig.5.3.

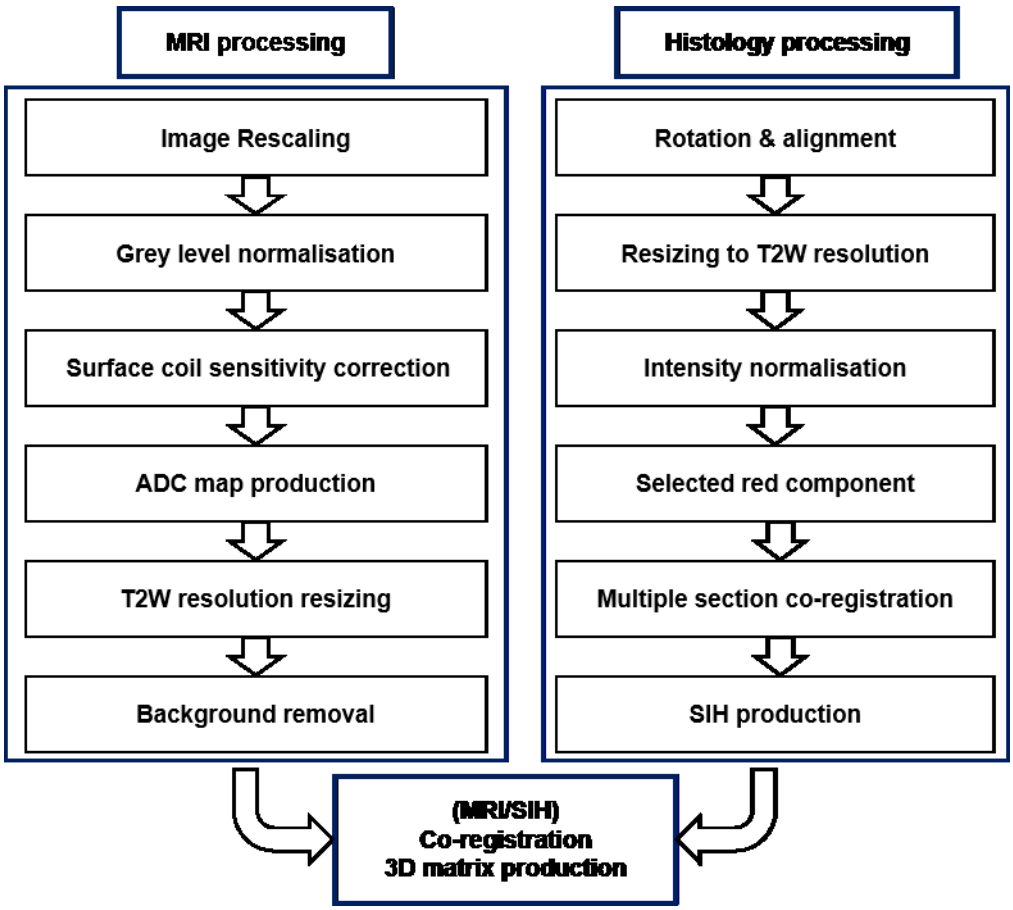

Figure 5.3: Simplified diagram of the image processing pipeline leading to the production of a 3D data matrix, combining both different MRI modalities and the SIH data. Reprinted with permission (Al-mubarak et al., 2019).

5.4 MRI data analysis

To remove any bias that could arise due to differences in the image intensity values for the different modalities, the DICOM images were normalised (0-1 range). Furthermore, non-uniform detection sensitivity associated with the use of a surface receiver coil was corrected, as it can adversely affect the registration processes: T1W, T2W and DW images were divided by phantom MRI images acquired using the same parameters to remove the sensitivity of the surface coil. (Axel et al., 1987). ADC maps were calculated by fitting the DWI data to the mono-

exponential equation of the Stejskal and Tanner model (Stejskal and Tanner, 1965). Normalized relative perfusion maps were produced from the MRI signal of the control image ($M_{control}$) and labelled image (M_{label}), using the equation ($M_{control}$-M_{label})/$M_{control}$. Prior to comparison, all data (DWI, ADC, ASL, and SIH) were resized to the T2W in-plane resolution (176 x 176). To reduce processing time, the brain region was separated from the background by the application of an active contour method following manual delineation (Caselles et al., 1997).

5.5 Histology data analysis

Following digital scanning of whole brain histology sections, the histology images were rotated by a small angle to remove differences in orientation of the brain caused by the placement on glass microscope slides. Histology images were then downsampled from their original resolution (approximately 1400x1200 pixels) using the cubic spline method (MATHLAB built-in function) to match the resolution of the T2W images (176x176 pixels). Signal intensity inhomogeneity, as a results of difference in staining across the image, were automatically corrected for each section by using a histogram equalization method (Belsare, 2012). Further, a threshold value was selected, creating a brain mask to remove the background signal. SIH maps were generated by a co-registration of multiple histology sections register using non-rigid Mutual Information method (MATHLAB built-in function) and by taking a voxel-wise average of the signal intensities. Registration used Mutual Information based transformation with global translation, rotation, scaling and shearing for optimal registration. In one histology section with greater tissue deformations, a B-spline method was applied to improve the registration.

5.5.1 Histology to MRI co-registration and production of 3D matrices

Registration of histology sections with MR images is typically challenging due to a significant variation of image properties, such as resolution, field of view and contrast (Madabhushi et al., 2005). Here, the SIH maps, allowed intensity based registration with MRI images to be undertaken using the Mutual Information registration method. For consistent registration, the histology sections were transformed so they had the same resolution and dimensions as the MR images.

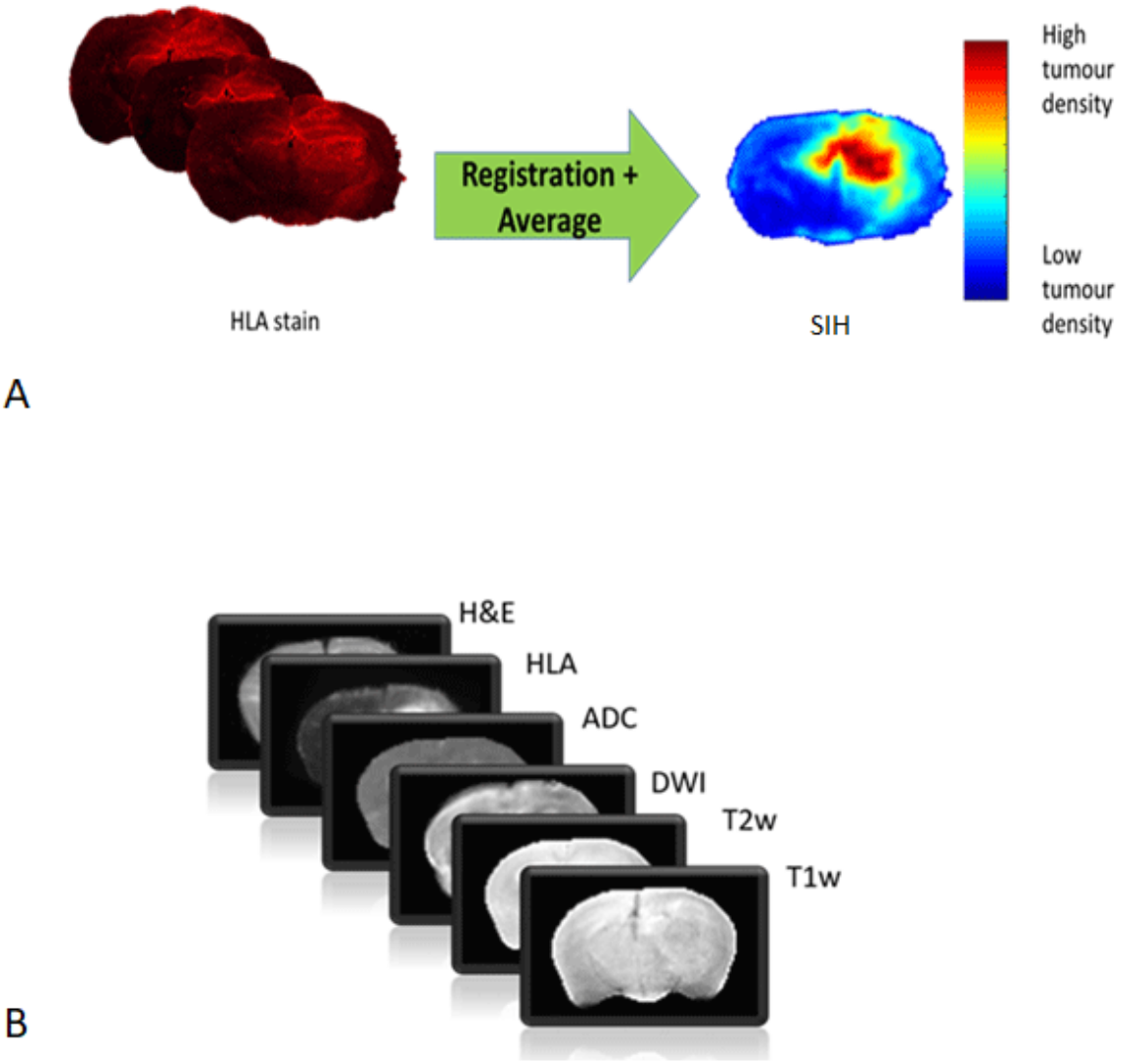

Figure 5.4: (A) Co-registration after three HLA sections and construction of a SIH map. (B) 3D matrix consisting of different MRI modalities and SIH.

5.5.2 Segmentation protocol

For both histology and MRI, tumour related abnormal Regions of Interest (ROI) were manually drawn by 3 observers (with more than 3 years' experience). Histology ROIs were selected based on HLA stain intensity on SIH maps. MRI ROI delineation was performed without prior knowledge of the histology data, to avoid selection bias. Care was taken not to include non-infiltration related enhancement (e.g. ventricle compression). Inter-observer reproducibility of ROI selection was evaluated using the coefficient of variation (100×standard deviation/mean), resulting in 10% for histology and 12-21% for the different MRI modalities.

5.5.3 Statistical analysis

The two-tailed Student's *t*-test was used for comparisons between MR measurements of tumour volume and histology measurements of tumour volume (SSH or SIH), using a Bonferroni correction (Graph Pad prism 6, Ver.6.01, 2012). All values are reported as means ± standard deviation. * Statistically significant $p<0.01$, ** statistically significant $p<0.001$, *** statistically significant $p<0.0001$ and NS not statistically significant. Statistical power analysis was performed using G-Power (version 3.1) software (Erdfelder et al., 1996).

5.6 Results & Discussion

We present a quantitative method for validating imaging-based biomarkers by registration with stacks of in-plane histology.

While it is generally agreed that histopathology is the gold standard for assessment, in practice most preclinical validation is limited to visual comparisons with sample histology sections, with little attempt made to spatially match the histology section to the corresponding imaging slice. By improving the quality of the histology processing and analysis, we have been able to produce stacked in-plane histology maps. These high quality SIH maps can then be co-registered with non-invasive imaging modalities, allowing more direct and quantitative validation of imaging biomarkers than has previously been possible.

To demonstrate this methodology, we applied it to a patient-derived mouse model of glioblastoma. In the case of GB patients, an imaging biomarker capable of identifying the full extent of GB cell infiltration would be valuable for both radiotherapy planning and in achieving complete surgical resection. Below, we assess the optimal number of histology sections need to produce SIH maps and the quality of SIH with MRI registration. Finally, potential MRI biomarkers are assessed, both by volumetric and voxel-wise comparison with SIH maps.

5.6.1 Tumour volume measurement via single-section histology (SSH)

Figure 5.5A shows exemplary H&E and HLA stained sections, obtained from within the 1.5 mm MRI slice. The heterogeneity in tumour shape and size is readily apparent at this length scale. The commonly applied method of arbitrarily selecting a single-section of histology (SSH) to estimate tumour volume inevitably leads to significant measurement variation. For example, the percentage difference between the minimum tumour volume (V_{min}) and maximum tumour volume (V_{max}) for each series of sections was found to be 46% for H&E and 50% for HLA (Fig.5.5B). While tumours can be identified on H&E sections due to a much higher density of cell nuclei, there is less sensitivity in detecting regions of low-density GB infiltration. However, Human Leukocyte Antigen staining is very specific in the mouse model, as it only stains cells that originated from the implanted human tumour cells. Hence, in the following analysis we define tumour volume as the maximum extent of GB cell infiltration identified using the HLA sections.

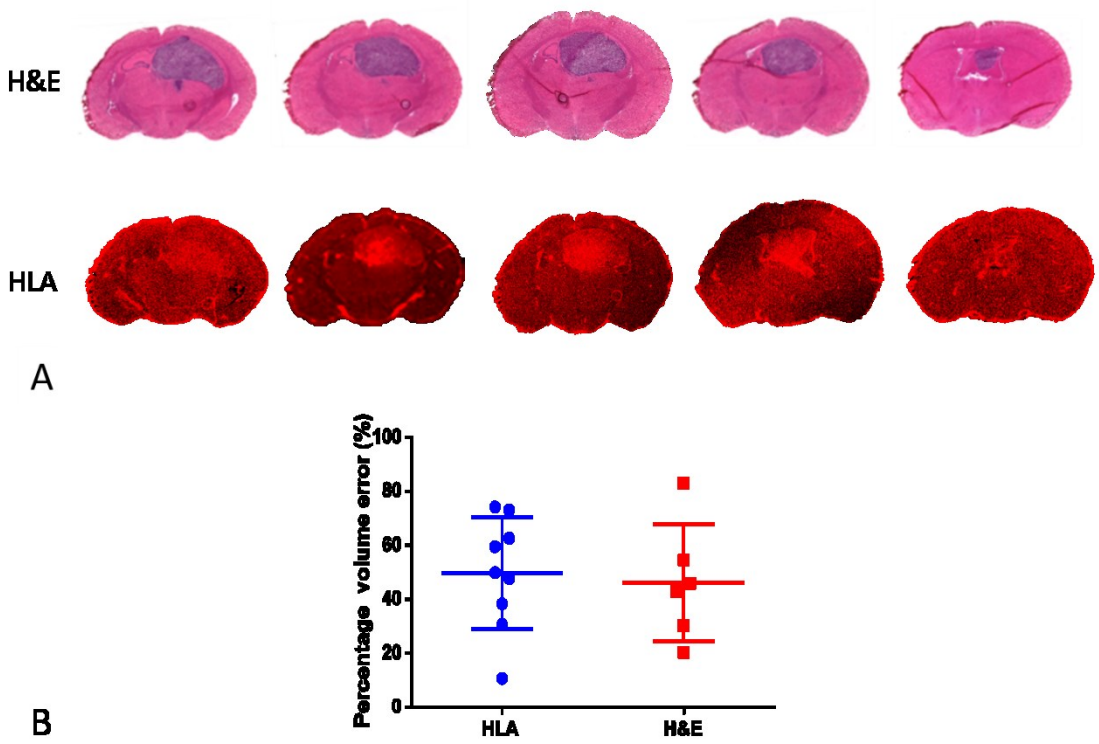

Figure 5.5: Examples of histology sections for a GB mouse and volume error comparison: (A) Five corresponding histology sections (H&E and HLA) cut within the 1.5 mm thickness of one MRI slice (B) Percentage volume error between maximum and minimum tumour volumes (V_{max} and V_{min} respectively), derived from in the five sections for each animal, calculated using $(V_{max} - V_{min})/V_{max})x100$. Reprinted with permission (Al-mubarak et al., 2019).

5.6.2 Determining optimal number of histology sections for SIH maps

It is clear that increasing the number of histology sections (20 μm thick) used to generate a SIH map will make the SIH map more representative of the corresponding imaging slice (1500 μm thick). However, this comes at the expense of longer processing time (histology preparation / analysis time). In applying the SIH method, the optimal number of sections will be disease specific, depending on the length scale of heterogeneities and the corresponding imaging slice thickness.

For the GB tumours, we assessed how tumour volume measurements were improved by using more HLA sections to generate the SIH maps. In 6 out of 9 mice, where five quality HLA sections were available, SIH maps were produced with one, two, three, four and five sections (Fig.5.6A-E), using all possible combinations of the sections. The measured tumour volume reaches a plateau when 3 or more sections are used to produce the SIH map, with no significant difference found between using 3, 4 or 5 sections (Fig.5.6F). These volume measurements are analogous to numerical integration where the more sections used to calculate a volume, the more accurate the result will be, eventually converging at the true value. To further investigate the effect of using multiple histology sections, we performed a ROC curve analysis (Garcia-Lorenzo et al., 2013) comparing SIH maps produced with 1, 2, 3 and 4 HLA sections to maps produced with 5 HLA sections. This assumed the 5-section map was the 'ground truth' for the assessment of the other maps, to avoid bias in the selection of sections, maps were produced from all possible combinations of sections for each mouse. It should be noted that the values of Dice, sensitivity, and accuracy indices will be dependent on the number of sections used in the gold standard. However, Fig.5.6G-J does show a diminishing increase of these indices with the number of sections used, and their standard deviation decreases markedly. As expected, specificity measures were not affected by this evaluation, as smaller numbers of sections tended to underestimate the tumour region.

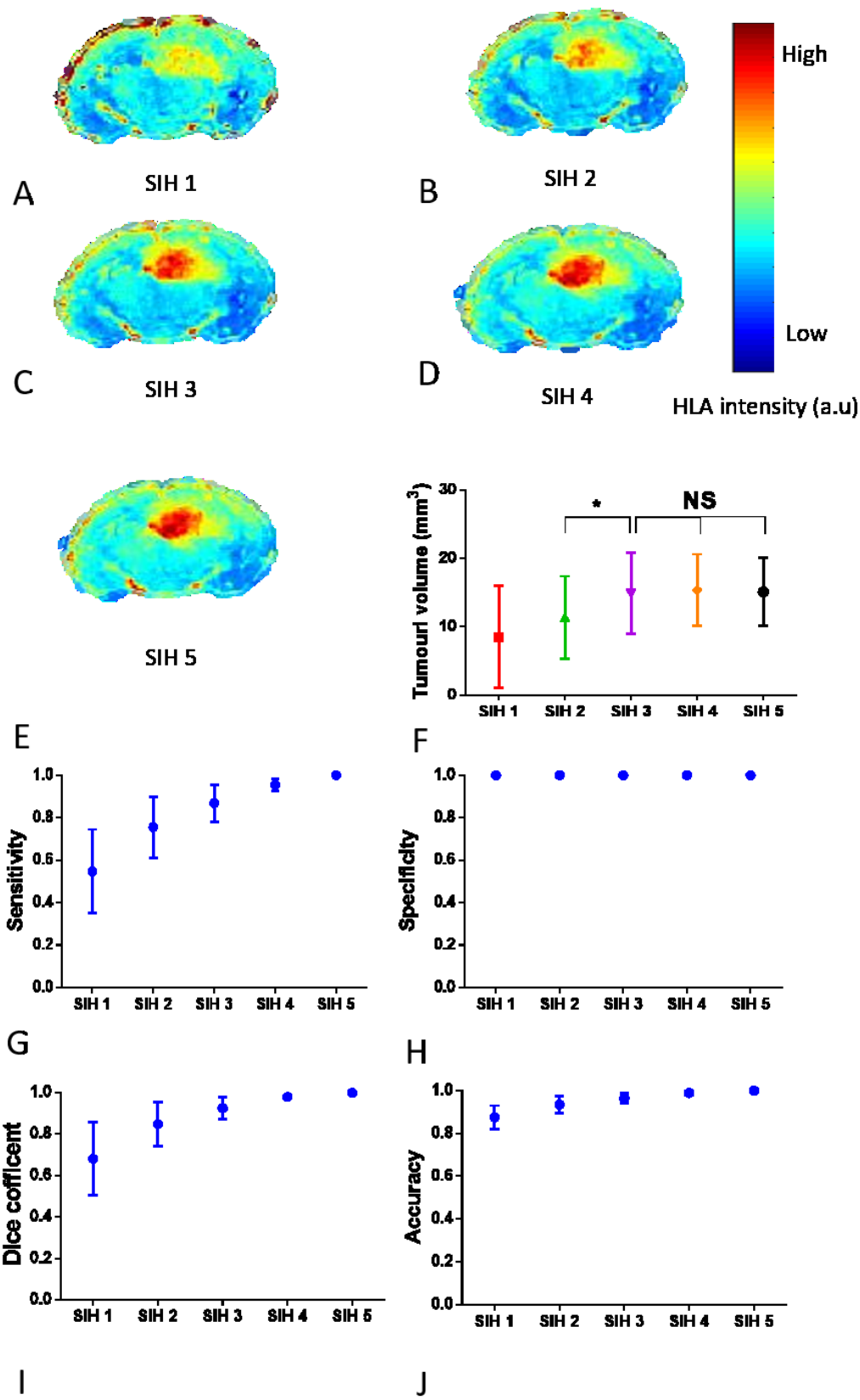

Figure 5.6: (A) One section (SIH1), (B) Two sections (SIH2), (C) Three sections (SIH3), (D) Four sections (SIH4) and (E) Five sections of HLA (SIH5). (F) Measured tumour volume against number of sections used to produce the SIH map (n=6). Evaluation of the ability of SIH maps to probe the tumour related abnormal area in comparison with the 5-section SIH map: (G) S ensitivity, (H) Specificity, (I) Dice similarity coefficient and (J) Accuracy indices. Reprinted with permission (Al-mubarak et al., 2019).

Given the above analysis, as a trade-off between improved accuracy and expanded processing time, we settled on using three histology sections for the remaining analysis. After excluding poor quality sections, the three sections with the largest tumour area were selected. It is crucial to note that the choice of three sections is very specific to this particular disease model (mouse model of glioblastoma). If the SIH method is to be applied to different disease models or different species, then the optimum number of slices will be different and will need to be assessed.

5.6.3 SIH to MRI registration quality

Registration of histology with MRI was qualitatively and quantitatively evaluated at each stage of the process. The qualitative evaluation consisted of a visual inspection of the overlay of the inner and outer contours of the T2W image and histology section (Fig.5.7). Accurate alignment was observed between borders and internal structures. Excellent post-registration overlays were found; with Dice values above (0.96±0.011). The resized and co-registered data were used to create a 3-dimensional data matrix, which allowed the MRI modalities to be assessed against histology, both in terms of tumour volume detection and via direct voxel-wise comparison.

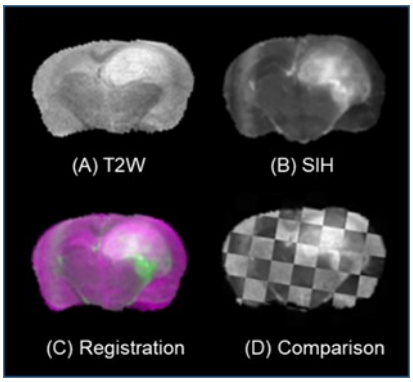

Figure 5.7: Example of non-rigid co-registration of histology with MRI using the Mutual Information method: (A) a T2Weighted image (T2W) (B) Stacked in-plane histology. (C) co-registration fusion image with false colour showing similarities (purple) and difference (green). (D) Checkerboard comparison between registered MRI and SIH maps. Reprinted with permission (Al-mubarak et al., 2019).

5.6.4 Volumetric assessment of SIH maps

The proposed SIH approach was used to quantitatively validate different MRI modalities as imaging biomarkers of GB infiltration, this is discussed in full in chapter 6. In this section, we focus on the comparison between tumour volume measurements made using single section histology (SSH) and volume measurements made using stacked in-plane histology (SIH) maps. For this, both the SSH and SIH approaches were used to measure the 'ground truth' tumour volume (i.e. the volume of GB infiltrated tissue) for the same dataset. Given the analysis in section 5.3.3, as a trade-off between improved accuracy and expanded processing time, we settled on using three HLA sections to produce the SIH maps. In all 9 mice, after excluding poor quality sections, the three sections with the largest tumour area were selected.

Fig.5.8A shows representative manual ROI selections for T2W, SSH1, SSH2, SHH3, SSH4, SSH5, and SIH in the same animal. Figure 5.8B shows tumour volumes obtained from manual delineation of the T2W, compared with tumour volumes measured from five individual single sections of histology (SSH). Clearly, the large standard deviation of the SSH tumour volume measurements (±6 mm^3) makes it a poor 'ground truth' for validating the T2W tumour volume measurements, with no significant differences found between any of the T2W and the SSH measurements.

However, tumour volume measurements made using SIH maps show a much lower standard deviation (±0.8 mm^3), Fig.5.8C, allowing better validation of the MRI modalities. A statistically significant difference was found between the SIH measured tumour volume and T2W which is considered as standard in MRI.

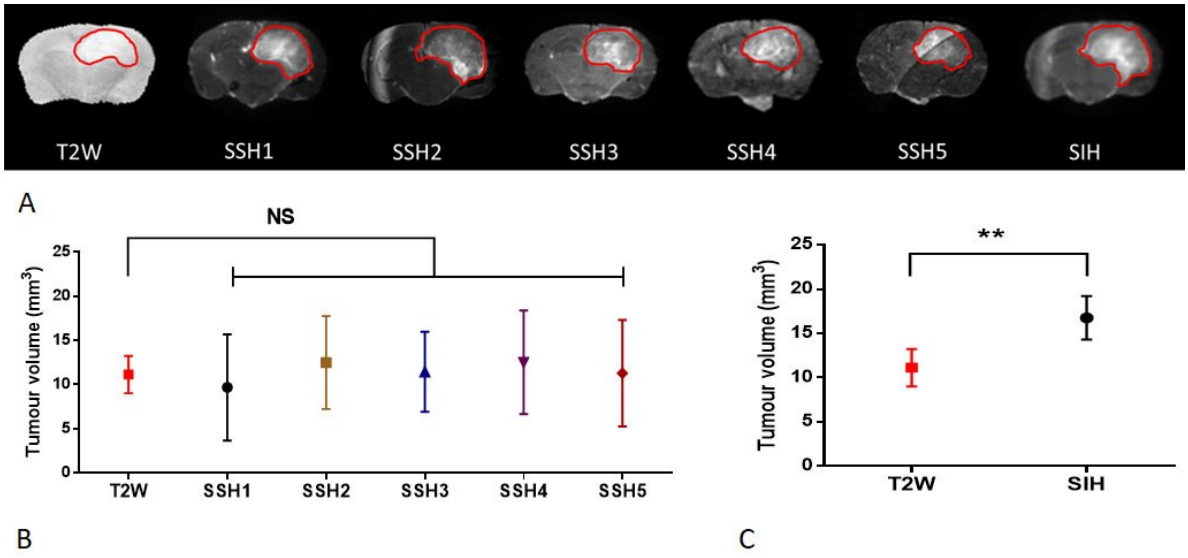

Figure 5.8: Volumetric analysis: (A) Examples of Regions of interest for T2W, individual histology sections (SSH), and SIH from the same animal. (B) Comparison of tumour volume measurements made using T2W and single sections of histology (SSH). (C) Comparison of tumour volume measurements made using T2W and stacked in-plane histology (SIH) maps generated using 3 sections. The volumes obtained for all animals as the mean ± standard deviation. Adapted from (Al-mubarak et al., 2019).

The lower standard deviation of SIH tumour volume measurements has important implications, as it allows statistical significance to be achieved without requiring an increase in the number of animals used. To further examine this, we performed power analysis using the results presented in Fig.5.8. For example, to achieve a statistically significant difference ($p<0.05$) between T2W and SSH tumour volume measurements, would require between 72 and 800 mice. By contrast, using SIH maps as the ground truth, required only 9 mice to achieve $p<0.01$, Fig.5.9. Such an impressive reduction in animal usage is a stated aim of the UK government, via its policy of Replacement, Refinement, and Reduction of Animals in Research (NC3Rs) and should arguably feature in future guidelines for reporting *in vivo* experiments (Kilkenny et al., 2010).

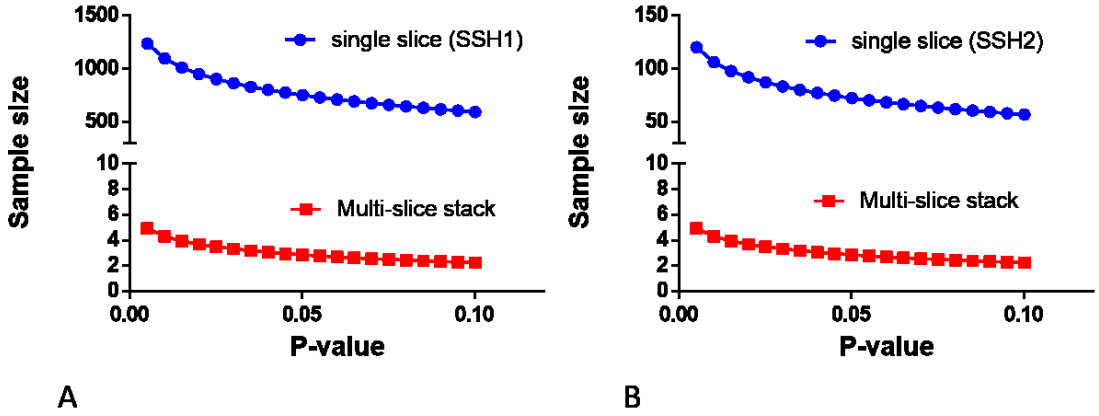

Figure 5.9: Power calculation of number of animals that would have been required for achieving a given significance with the single-slice or the SIH approach for two different single slice groups (A) section SSH1 (B) section SSH2. Reprinted with permission (Al-mubarak et al., 2019).

5.6.5 Towards voxel-by-voxel assessment

A new application can be envisioned for the validation of *in vivo* imaging modalities with 2D histopathology. The *in vivo* imaging signal and histopathology could quantitatively assess how sensitive and how specific are the signal detected *in vivo*. Another perspective concerns the analysis of imaging biomarker is voxel by voxel which providing the opportunity to gain deeper insight into neuroanatomy and to improve our knowledge of mechanisms involved in disease states.

The ideal approach to validating imaging biomarkers would involve voxel-by-voxel comparison with co-registered histology. To date, the difficulties involved in accurately co-registering histology sections with imaging slices have prevented this. However, we believe that the methodological pipeline we have outlined overcomes many of these difficulties, yielding a co-registered multi-dimensional data matrix (T2W, DWI, ADC, ASL and SIH map).

In the case of HLA, the staining intensity is proportional to the density of tumour cell membranes. Therefore, by averaging multiple histology sections, the resulting SIH maps represent a semi-quantitative measure of tumour cell density in the MRI slice. This allows the MRI modalities to be more accurately evaluated against histology in a direct voxel-by-voxel analysis. For example, Fig.5.10A-C shows scatter plots of different MRI modalities against SIH intensity. Here the pathogenic

regions identified by the 'ground truth' histology ROIs can be highlighted, allowing the relationship between the MRI signal and the underlying histopathology to be assessed. Furthermore, it enables the assessment of multi-spectral analysis approaches on a voxel-by-voxel basis, investigating and validating combinations of MRI parameters against histology.

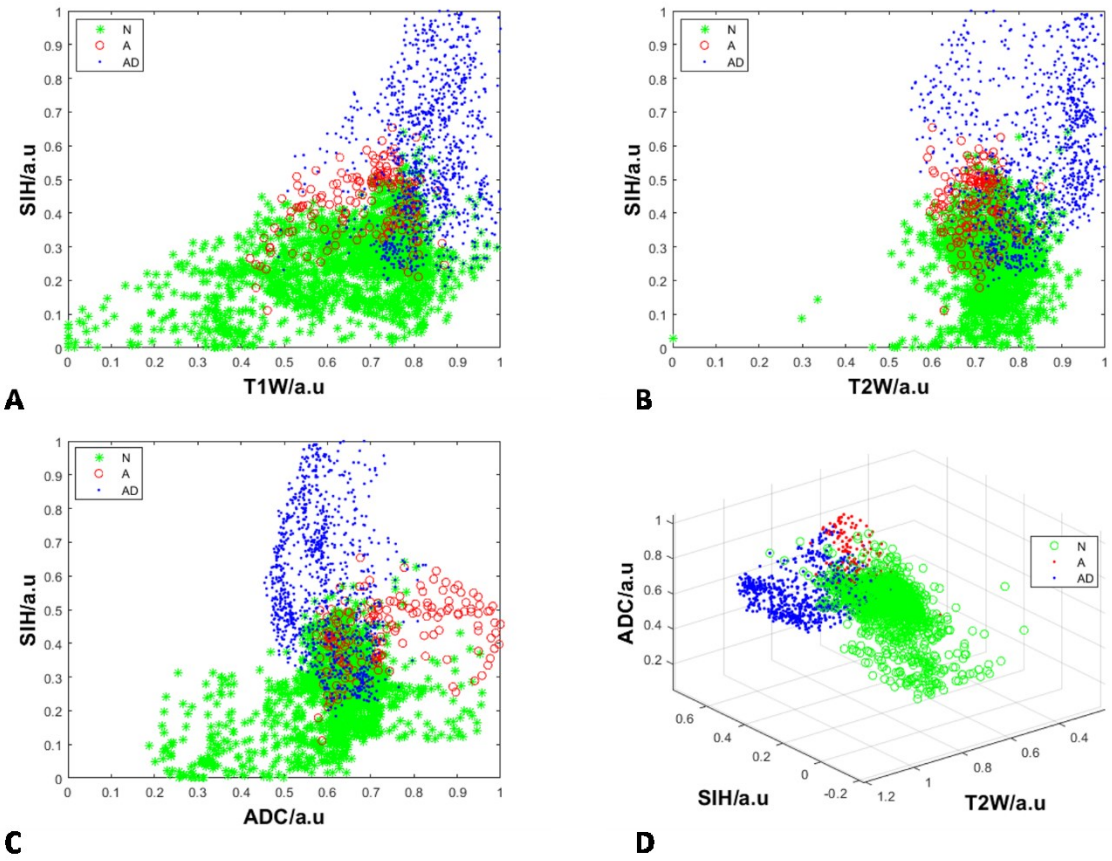

Figure 5.10 Comparison scatter plots between different MRI modalities and histology. Highlighting the pathogenic regions identified by the "ground truth" histology ROIs allows the relationship between the MRI signal and the underlying histopathology to be assessed. Where N is a pixel of normal tissue, A is a pixel of abnormal region and AD a pixel of abnormal region that cannot detect by MRI.

Figure 5.10 shows three types of voxels' regions. The first region is green (N) and it represents normal tissue. The second region is red (A) and represent an abnormal tissue that can be detected by MRI. Finally, the blue region (AD), represents abnormal tissue that cannot detected by MRI. The interface between these regions makes it difficult to distinguish amongst them by using MRI. More research is needed to find the relationship between MRI modalities the tissue being scanned that may allow improvement in tumour diagnosis and therapy planning.

5.7 Conclusion

We have introduced a novel methodological pipeline to improve the validation of non-invasive imaging biomarkers. In contrast to most previous studies, which focus on improving the registration algorithms, we have taken the approach of improving the quality of the histology processing and analysis. In an infiltrative brain tumour model we have demonstrated how stacked in-plane histology maps, co-registered with multiple MRI modalities, provide a 'ground truth' for quantitative comparisons. Our results demonstrate that, in cases of small and heterogeneous tumours the use of this multi-section approach is crucial, as conventional assessment using single-section histology is prone to significant errors.

In chapter 6, this new methodology is used to validate the use of perfusion MRI as a marker of glioblastoma cell infiltration. Finally, achieving robust three-dimensional registration with non-invasive imaging modalities, the development of this method could lead to voxel to voxel histopathologic assessment of new imaging biomarkers, we discuss this possibility further in Chapter 7.

Chapter 6

Quantitative Histopathological Assessment of Perfusion MRI as an Imaging Biomarker of GB Infiltration

6.1 Introduction

Of all primary brain tumours with a poor prognosis, glioblastoma is the most common and aggressive. Patients who are receiving the currently accepted standard of care (surgery, radiotherapy, and chemotherapy) survive, on average, 12-15 months after diagnosis (Johnson et al., 2018) and face a high probability of tumour recurrence. A major limitation of successful treatment is the ability of tumour cells to infiltrate into normal brain tissue (Price and Gillard, 2011), potentially extending several centimetres from the tumour bulk.

Neuroimaging has been become vital for the management of high-grade gliomas. It is used for the detection and localisation of tumours, for the planning of neurosurgery and radiotherapy and to assess treatment efficacy. One of these techniques is MRI. It has been used to provide information on brain tumour growth, structure, function, vasculature, and metabolism (Dominietto, 2014). T2W imaging is usually used to obtain an anatomical view of the brain. Tumours typically appear hyperintense relative to normal brain tissue in the T2W image. However, oedema, huge vessels, haemorrhage, and necrosis have different T2 relaxation times and contribute to the heterogeneity of the T2W. T1W imaging is generally used to highlight the presence of tumours before and after the injection of contrast agents such as Gd (Earnest et al., 1988). Tumour vessels have a disrupted blood-brain barrier, allowing the contrast agent to leak out and accumulate in the tumour's tissue. Consequently, the tumour becomes brighter than surrounding tissue due to the shortening of the T1 relaxation time. FLAIR sequences are like T2W acquisitions, except that the signal of the cerebrospinal fluid is eliminated. They can be used to delineate the boundaries of peritumoural oedema.

Several studies have shown the extension of tumour cells beyond the contrast enhancement region. For example, (Swanson et al., 2003) proved that theoretically and by using invasion models accounting for MRI sensitivity that infiltration may often extend beyond abnormal T2W regions. Watkins et al. (2014) have showed the presence of tumour cells outside the CE-T1 enhancement region. However, most cMRI sequences are limited in their ability to adequately probe infiltration of tumour cells, typically adjacent to the CE-T1 abnormal region (Kelly et al., 1987). There is no single study which has been validated by histology which

demonstrates infiltration of tumour cells beyond the oedema region. The infiltration of tumour cells may decrease the accuracy of target volume delineation for radiotherapy planning (Niyazi et al., 2016). Therefore, it is important to develop imaging modalities that enable better tumour delineation which, in turn, allow increased efficiency in therapy planning.

However, advanced MRI techniques show promising results in the detection of the invasion of tumour cells. Jarnum et al. (2010) state in their study that perfusion measurements beyond the contrast enhanced region tend to show increased values due to early angiogenesis. Another study by (Swanson et al., 2003) investigated the effect of invasion into white matter and tracts by DTI using infiltration patterns. The metabolic behaviour of tumour cells can also be used as a biomarker of tumour infiltration. For example, (Holash et al., 1999) found increases in both choline peaks using magnetic resonance spectroscopy. Further, positron emission tomography has been used to measure abnormal uptake of ^{11} C-methionine in regions with low tumour cell density.

The ability to detect the infiltration of tumours in their early stage is challenging. One MRI method with the potential to detect tumour infiltration is perfusion imaging. Perfusion measurements are performed either by using exogenous contrast agents, such as in DSC and DCE, or by using endogenous blood water, as in ASL (Jarnum et al., 2010). DSC and DCE are widely used in brain tumour imaging (Shiroishi et al., 2015). However, there are relatively low SNRs in infiltrated healthy tissue regions which make subtle perfusion perturbation studies challenging.

ASL has been shown to provide similar results to DSC in brain tumour studies and it has been used to improve GB delineation and facilitate clinical decision-making (Geer et al., 2012). The SNR achieved by ASL may be more sensitive to subtle perfusion perturbations in the infiltration zone than other methods, making ASL a suitable candidate for probing infiltration beyond the CE-T1 enhancement region.

Preclinical studies provide an opportunity for more quantitative histopathologic assessment of MRI. However, most studies to date have used qualitative approaches, probably due to difficulties with MRI and histology registration (Cha et al., 2003). Frequently, histological sections are not cut in the MRI plane and

the enormous difference in slice thickness compared with MRI is ignored (histology~20 μm, MRI~1000 μm). The development of new methods of quantitative histopathologic assessment of MRI modalities is crucial in order to analyse infiltrative glioblastoma models where heterogeneous tumour distributions can vary considerably within the MRI slice thickness.

In Chapter 5, a new method was described for producing high quality registration of MRI and histology. In this chapter we describe the use of this method to quantitatively evaluate the ability of several MRI techniques to probe infiltration of tumour cells. For this, we used a realistic GB model presenting both a tumour bulk region and highly infiltrative edges. Research focussed on regions of low tumour cell infiltration, not easily detected by standard clinical imaging techniques. We also focussed on the interrogation of MRI sensitivity limits compared with perfusion weighted images (PWI) provided by a recently developed high SNR multi boli ASL sequence (mbASL). The relation between perfusion and GB cell density at the tumour edges was also evaluated. Registering MRI with histology data allows voxel-wise analysis, giving a deeper insight into the relation between local tumour infiltration and MRI signal variation. The data gathered suggest a negative correlation between perfusion and marginal infiltration of GB cells.

6.2 Tumour region of interest selection

Tumour regions of interest (ROIs) were manually selected for each imaging modality (T1W, T2W, DWI, ADC and mbASL) and SIH was mapped by three persons (with 3, 3 and 5-years' experience, respectively). To avoid selection bias, the delineation of MRI ROIs was done without prior knowledge of the histology data (SIH). Moreover, care was taken not to include non-invasion related enhancement (e.g., ventricle compression). One mouse that did not show tumour growth was removed from this study, while two mice showing necrotic regions were not considered for voxel-to-voxel comparison with SIH maps. Histology ROIs were selected based on HLA stain intensity on SIH maps. Independent intensity-based selection was used for manual selection.

6.3 Statistical analysis

As previously mentioned, SIH maps were considered as the 'ground truth' for defining the tumour boundaries and were evaluated against ROIs defined using MRI. The accuracy of inter-observer reproducibility was quantified using the coefficient of variation that was calculated for each region. Sensitivity, specificity, accuracy and dice similarity indices (Garcia-Lorenzo et al., 2013, Zou et al., 2004) were calculated for each animal and imaging modality. A two-tailed student *t*-test (Armstrong, 2014) was performed for comparisons between MRI and SIH ROI measurements. All values are reported as mean ± standard deviation. Statistical significance flags: * $p<0.05$, ** $p<0.01$, *** $p<0.001$, **** $p<0.0001$ and NS (not statistically significant).

6.4 Results

6.4.1 Marginal infiltration of mouse model

In glioblastoma, MRI usually can distinguish three main regions: central regions of necrosis, the active tumour region, and oedema. Figure 6.1A shows T2W and CE-T1 images for week 12 post-injection. While significant abnormal volumes could be measured on T2W, most CE-T1 images showed no significant signal change. Only three cases of CE-T1 contrast were identified at this stage of the tumour development and they displayed only light enhancement and no necrotic core (e.g. Fig. 6.1). Later in the tumour development (week 15), most CE-T1 images showed (Fig. 6.1B) a non-enhanced core (necrotic core) surrounded by a contrast enhanced region. The infiltration of tumour cells in the margins were confirmed by histology with three stains, namely, HLA, Ki67 and H&E (Figure 6.1C). At this stage of the tumour development, T2W abnormal regions appeared to be fairly homogeneous, with the abnormal volume growth being similar for most of the animals studied (Fig. 6.2A-B). It should be noted that after week 12 and the appearance of a necrotic core, a substantial spread of tumour growth was observed in the animals and most began losing weight (Fig. 6.2C).

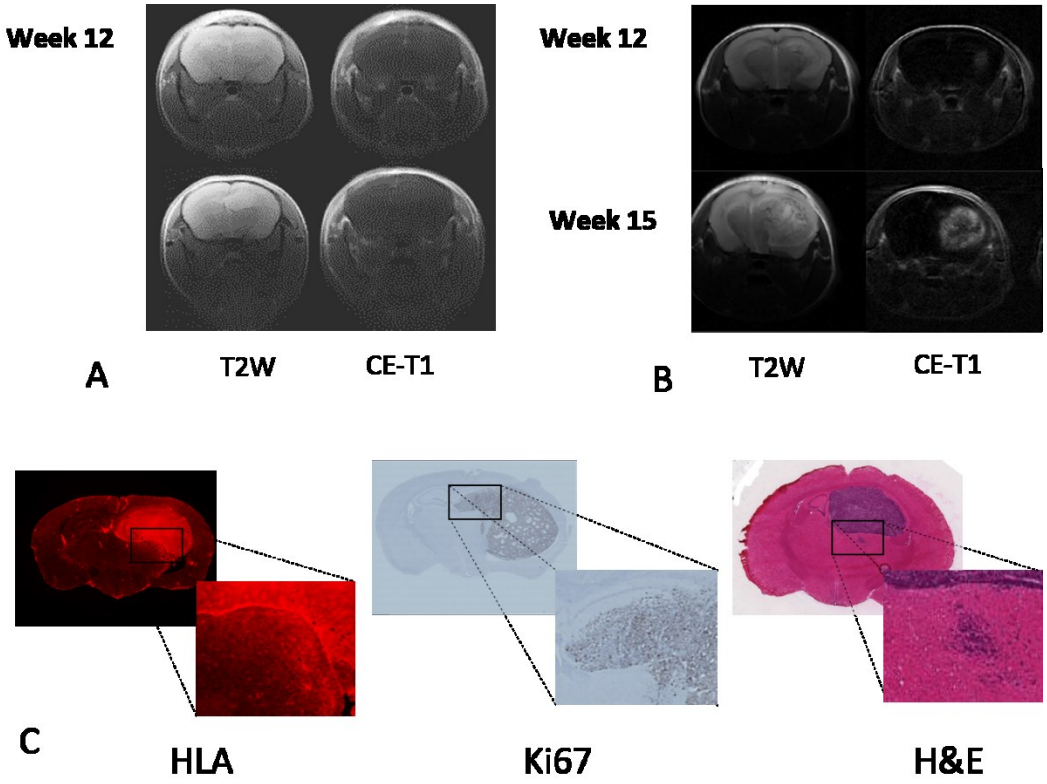

Figure 6.1: (A) T2W and CE-T1 images at week 12 post-injection for the same animal. (B) T2W and CE-T1 images obtained at 12 and week 15 post-injection. (C) HLA, Ki67and H&E stains show infiltration of tumour cell at the margins.

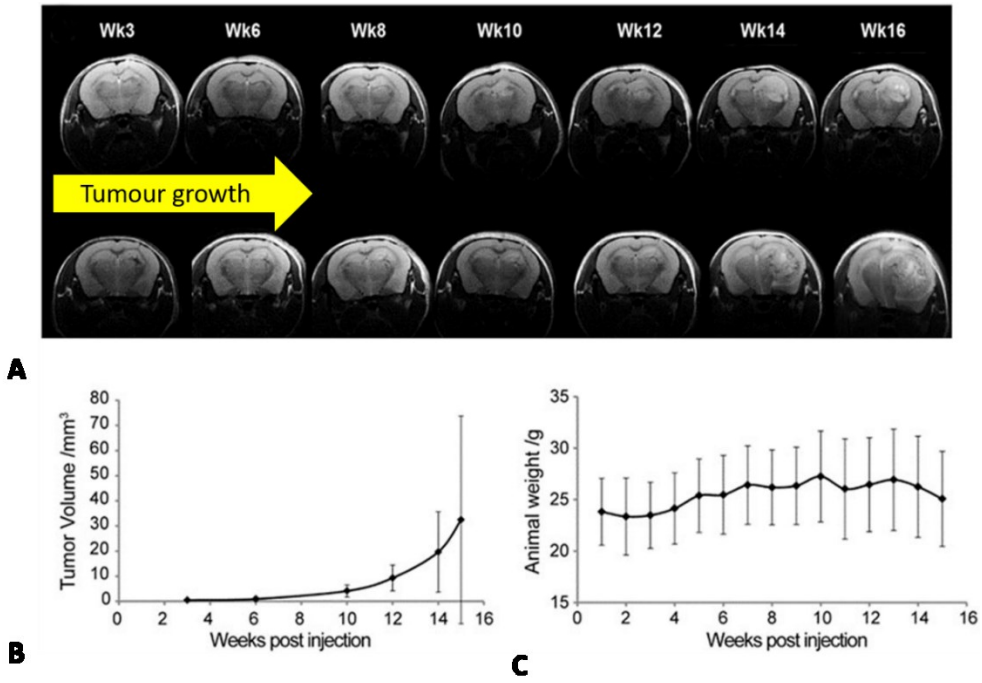

Figure 6.2: (A) T2W images at different time points. (B) Average tumour volume and (C) Average animal weight over a 15-week period post -injection (n=6). Reprinted with permission (Vallatos et al., 2018a).

6.4.2 Perfusion detects more extensive regions of tumour

Figure 6.3 A, B shows images obtained at weeks 9 and 12 during the longitudinal MRI study. Most MRI techniques (T2W, DWI, ADC and mbASL) detected tumour regions by week 9. The tumour region remained homogeneous until week 12, appearing hyperintense on T1W, T2W and DW and hypointense on ADC and mbASL. Only two mice exhibited small necrotic cores at this stage of tumour progression (high ADC in the tumour core). FA values were low in tumour core regions, indicating oedema with high FA values around the margins of the tumour. At week 12, strong similarity was observed between the abnormal regions identified by the different MRI modalities and the regions of high tumour cell concentration identified on tumour cell concentration maps (SIH).

Figure 6.3 A, B shows the corresponding MRI ROIs in weeks 9 and 12. Inter-observer CV at week 9 was 29% for T2W, 12% for DWI and 19% for both ADC and mbASL. At week 12, CV was 20% for T1W and T2W, 21% for DWI, 19% for ADC, 12% for mbASL and 10% for SIH maps.

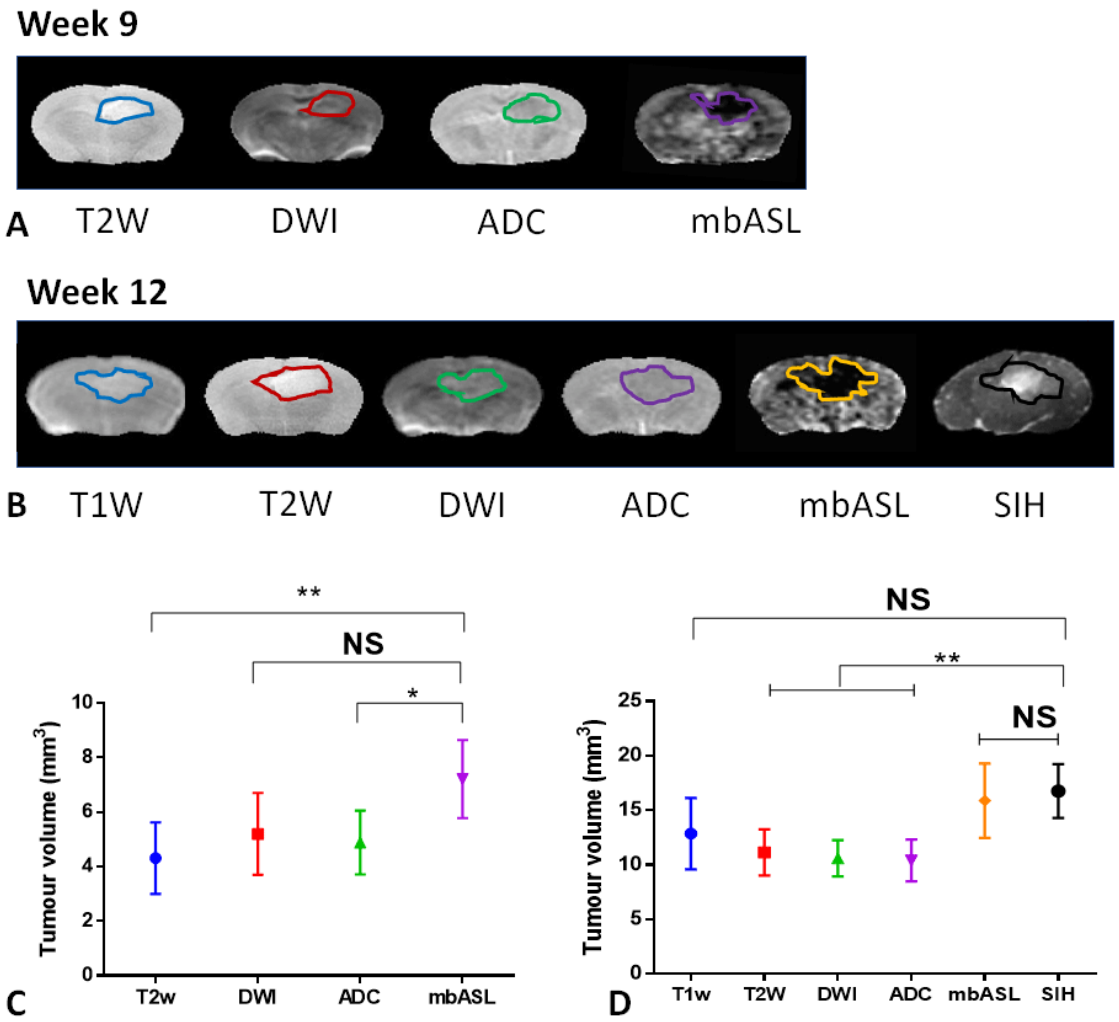

Figure 6.3: (A) (A) Example of manual selection of ROIs in week 9 using different MRI modalities. (B) Example of manual selection of ROIs in week 12 includes the SIH map obtained for the same brain region. (C) Volumetric comparison between different MRI modalities at 9 weeks (D) Volumetric comparison between different MRI modalities and SIH at 12 weeks (n = 9). Two-tailed student's t-test after Bonferroni correction was used for comparison between MRI images and SIH. Statistical significant flags: * P<0.01, **P<0.001 and NS (not statistically significant). Reprinted with permission (Vallatos et al., 2018a).

Figure 6.3 C-D shows the average volumes and ± standard deviation of tumour abnormal regions for the MR imaging modality at 9 and 12 weeks post-injection of G7 cells. Both end points show that perfusion weight imaging exhibited larger abnormal regions than T1W, T2W, DWI and ADC at both time periods. The results in week 9 should be considered with caution, because the abnormal region is relatively small. Hence, resizing of the lower resolution imaging modalities, such as mbASL, can possibly introduce errors into the data. The size of this ROI selection error was estimated by using a coefficient of variation which was found to be 10% for the smaller abnormal regions at week 9 and below 1% for the medium and

abnormal regions at week 12. That error is small compared with the T2W/mbASL abnormal volume ratio (~60% at week 9 and ~75% at week 12).

Due to accurate co-registration of MRI and histology (SIH) it is possible to make a quantitative evaluation (volumetric analysis) of the MRI biomarker with the ground truth histology (SIH). Tumour volume comparison between MRI and SIH revealed no significant (p=0.2) difference between abnormal perfusion volumes and SIH volumes. However, there was a statistically significant difference between MRI (T2W, DWI, and ADC) and SIH.

Figure 6.4 shows the results of ROC curve analysis of abnormal volumes between different MRI modalities and SIH.

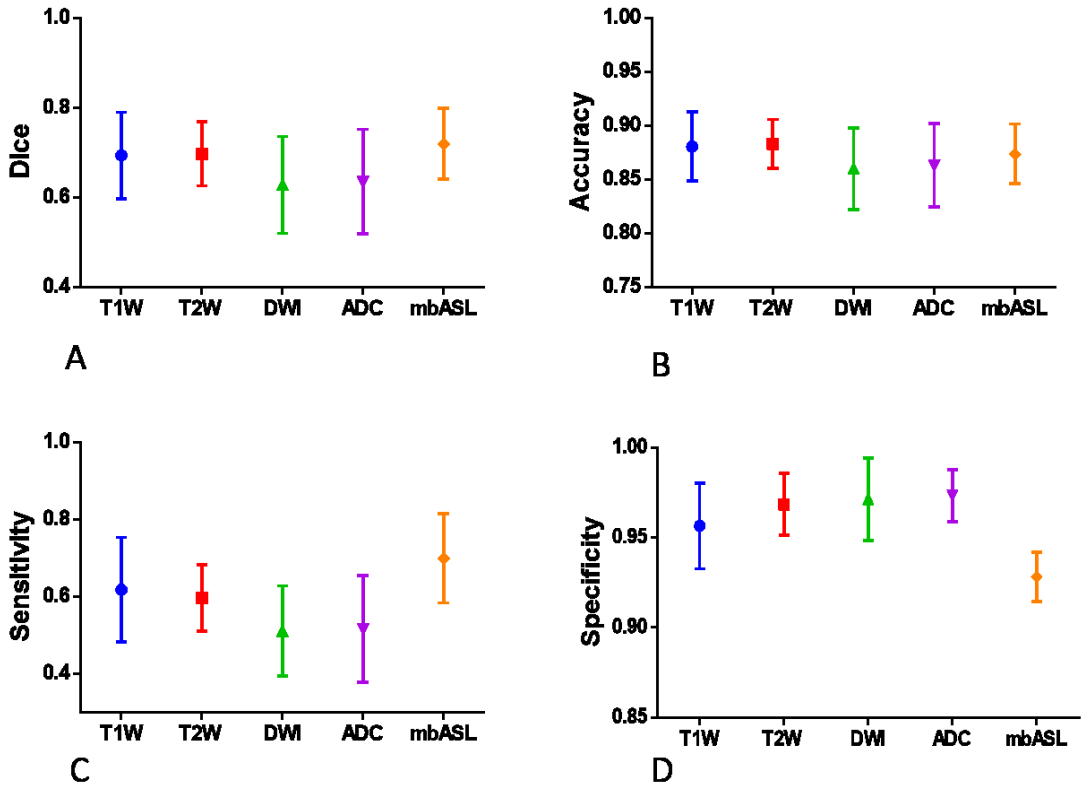

Figure 6.4: (A) Dice, (B) Accuracy (C) Sensitivity (D) Specificity of volumetric analysis segmentation of each imaging modality and SIH of tumour regions at week 12. Reprinted with permission (Vallatos et al., 2018a).

All abnormal regions of MRI obtained high Dice coefficients and approximately similar accuracy compared with SIH (Figure 6.4 A-B). The abnormal perfusion region achieved the highest Dice score compared with T1W, T2W, DWI and ADC. The mbASL showed more abnormal regions compared with the other MRI

modalities and mbASL was associated with higher sensitivity than other MRI techniques (Fig. 6.4C). However, T1W, T2W, DWI, and ADC imaging showed higher specificity than perfusion (Fig. 6.4D) due to the tendency for perfusion to extend outside the tumour region. This demonstrates that, firstly, clinical MRI protocols under-evaluate tumour volume and, secondly, that average mbASL ROI volume (15±3 mm^3) was approximately similar to the average SIH ROI volume (16±2 mm^3), with only three cases of mbASL ROI volumes greater than SIH by 13%, 8%, and 3%.

6.4.3 Relationship between perfusion and invasion in tumour margin regions

Histological analysis was used to find the relationship between perfusion and infiltration of tumour cells. Figure 6.5A shows a comparison between histological slices of FITC-dextran 70kDa that detect perfusion and HLA stained slices for the same animal. The same MRI slice is shown in Fig. 6.5A-B. The regions of hypoperfusion, which are clearly demonstrated by perfusion MRI and dextran histology, show a strong relationship between perfusion imaging (mbASL) and FITC-dextran staining. Furthermore, the region of infiltrative tumour cells showed reduced perfusion in both mbASL and dextran assays.

This relationship between perfusion and infiltration was stronger in the marginal tumour region, which has a low density of tumour cell infiltration. The relationship was highlighted by the dataset from one mouse that developed two distinct tumour regions (Fig. 6.5B). Firstly, the high-density region near the tumour cell injection point is surrounded by a small necrotic core (white spots on T2W and ADC; black spots on HLA). Secondly, the low-density region appeared later in tumour growth. The physical connection between the two regions that occurred at the back of the brain is distinguished by the red arrows on the T2W images (Fig. 6.5B second row). Both mbASL and dextran images show a reduction in perfusion in the infiltrated lower-density region. This relation between dextran delivery and invasion is less clear around the necrotic core of the tumour.

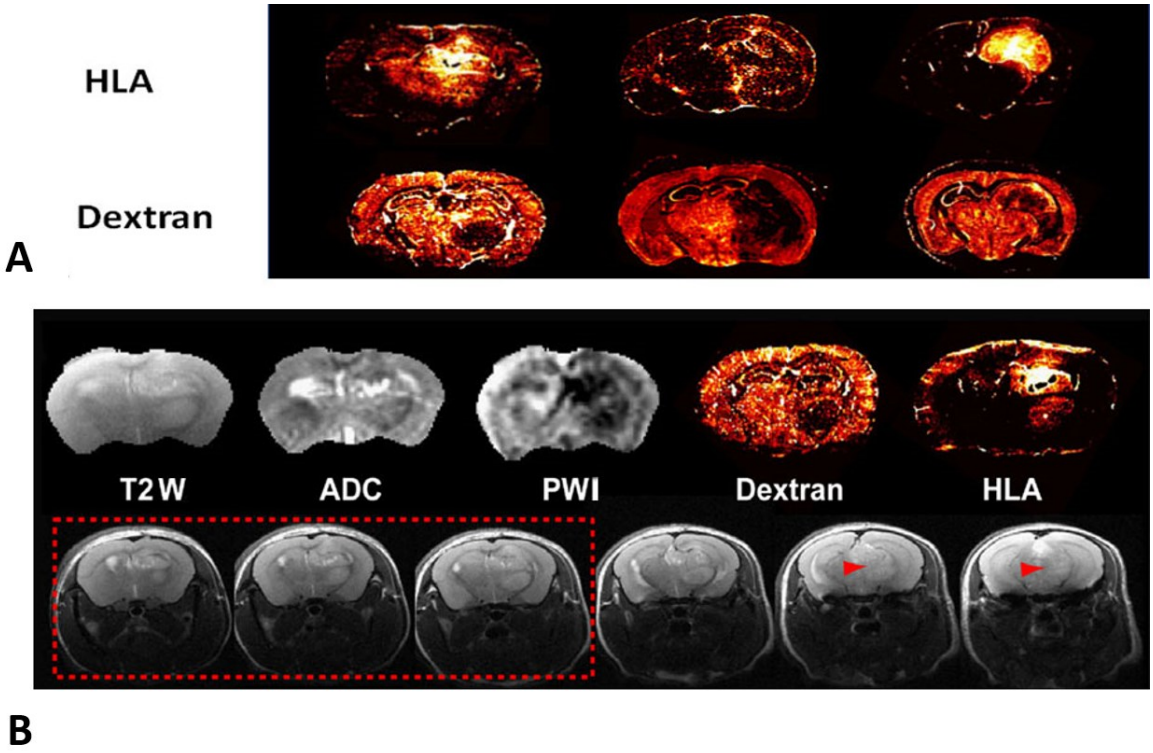

Figure 6.5: (A) Example of fluorescence microscopy images probing HLA and dextran 70kDa for three mice. (B) First row shows different MRI and fluorescence microscopy images (HLA, dextran) from a mouse at 12 weeks. Second row shows T2W images of thickness 0.5 mm acquired at the same time point. The red dotted box highlights the three 0.5 mm thick T2W slices acquired at the same location as the T2W image (shown in the first row). Red arrows display connection points between the upper and the lower tumour lesions. Reprinted with permission (Vallatos et al., 2018a).

6.4.4 Perfusion variation as a marker of tumour cell infiltration

The accurate co-registration of MRI modalities and SIH maps, which are evaluated in Fig. 6.4, allow voxel-to-voxel comparison to be applied. To separate high and low tumour density regions within mbASL and SIH ROIs, the ROIs in both mbASL and SIH were selected manually (Fig.6.6A) using a Gaussian mixture model with two clusters performed.

The scatter plots of perfusion (mbASL) against SIH for one animal are shown in Fig. 6.6B. Voxels identified as tumours on SIH maps are highlighted using red dots and the whole brain is highlighted using grey dots. The voxel-based approach can be used to find the relationship between perfusion and invasion at the tumour's margins (Fig. 6.5C). This analysis shows that the perfusion value was generally higher in low SIH value voxels and decreased with increasing SIH.

In Fig. 6.6C, the marginal voxels (green) of the tumour have lower SIH values than the core voxels (red). In fact, these marginal voxels exhibit higher perfusion values than tumour core voxels (Fig. 6.6D). The relation between perfusion and invasion at the margins of the tumour was evaluated by applying separate linear regression fits to the core and the margins (Fig. 6.6C). The negative correlation between tumour infiltration and perfusion was observed at the tumour margins, whereas no clear relationship was observed within the tumour core region (Fig. 6.6E). Linear regression R2 values were statistically significant between perfusion at the margins and perfusion in the core of tumour (Fig. 6.6F).

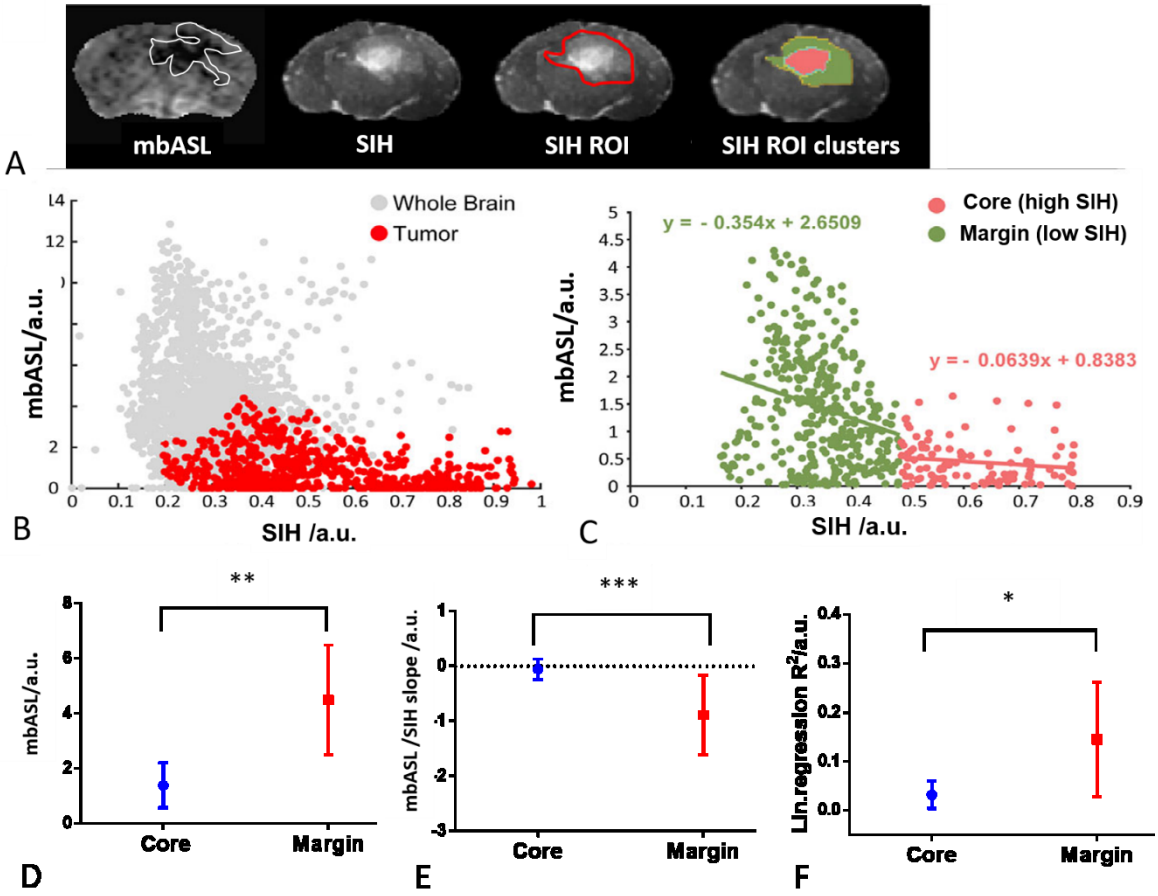

Figure 6.6: (A) Example of mbASL and SIH images from one mouse. SIH ROIs were manually selected (red outline), and SIH ROIs were clustered into two regions. (B) Scatter plots of mbASL signals against SIH for each voxel in the tumour region. (C) Scatter plots of perfusion signals vs. SIH for the tumour voxels only. (D) Comparison of perfusion average signal between core and margin of tumour region shown in (A). (E) Linear regression fit slope comparison between core and margin of tumour region. (F) R^2 of the linear regression fit (n=7). Reprinted with permission (Vallatos et al., 2018a)

6.5 Discussion

This study has proven the existence of a negative relationship between tumour cell infiltration and local perfusion in the tumour margin region of an orthotopic G7 model that replicates features of human glioblastoma. To achieve this, we used an *in vivo* mouse model which exhibits infiltrative tumour margins. In addition, the approach described in Chapter 5 was used to prepare histology sections and register them with mbASL. One of the common models used in preclinical studies is nude mice implanted with brain tumour cells. The deficiency of the immune systems in nude mice allows many tumour models to grow fast. One of the major obstacles to studying tumour invasion is the lack of good preclinical mouse models to accurately replicate tumour cell invasion. In this

work, the G7 infiltration tumour model was selected to replicate glioblastoma behaviour seen in a human. The highly infiltrative G7 model exhibits regions of low tumour density which are not detected by CE-T1. This region usually extends beyond the range of T2W hyperintensity. Moreover, the slow rate of progression of the G7 model, where oedema is larger than the CE-T1 region, allows replication of the clinical scenario. By contrast, other preclinical GB models frequently show poor tumour cell infiltration, exhibiting a sharp transition between tumour bulk and healthy brain tissue, with the size of T2W and CE-T1 regions remaining the same (Cha et al., 2003).

Angiogenesis is a physiological process of the formation new blood vessels from pre-existing vessels in the early stages of a tumour. Generally, angiogenesis requires solid tumour conditions such as significant tumour size, acidity and hypoxia (Gillies et al., 1999). Brain tumours may develop and grow using the vascular system called co-option mechanism (Leenders et al., 2002). The development of neovascularization in the tumour core (G7 model) that induces angiogenesis allows accurate modelling of the invasive of tumour cells in the borders. One of the important chemical signals of growth is Vascular Endothelial Growth Factor (VEGF), which controls angiogenic (including endothelial cell) proliferation and migration (Ghaffari et al., 2017), appears to be involved not only in neovascularization but also in oedema production (Machein and Plate, 2000) through the induction of vascular permeability (Leenders et al., 2002).

The mechanism of angiogenesis is expected to affect perfusion (Blystad et al., 2017). In preclinical situations, decreased perfusion in tumour regions is generally observed in rodent glioblastoma models and can be explained by the early stage of tumour progression and before disruption of the blood-brain barrier which is related to leaky vessels that arise from angiogenesis and increasing distance from the contrast-enhancing region. The infiltrative models typically exhibit a detectable reduction in perfusion within the tumour region (Cha et al., 2003).

Other mechanisms may affect perfusion. The relationship between perfusion and intracranial pressure (ICP), where compression of the brain tissue caused by oedema in combination with increased ICP, can cause reduced local perfusion with increasing distance from the contrast-enhancing region of the tumour (Blystad et al., 2017). ICP effects are expected to be less in the margins of the tumour due

to the relatively small marginal volume. However, infiltration of tumour cells could cause healthy tissue compression that may lead to perfusion drop.

It is challenging to probe and evaluate the infiltration of tumour cells at the margins. The detection power of MRI is limited and often exhibits inhomogeneous spatial distributions that compromise visual validation using histology. Therefore, a new method for quantitative MRI assessment with histology (stack of in-plane histology slices, 'SIH') was used (see Chapter 5). This method allowed for the quantitative evaluation (voxel by voxel) of a range of MRI techniques (T2W, DWI, ADC, and mbASL) with SIH. The high specificity of T2W in comparison with SIH maps shows that most abnormal T2W regions are related to regions of tumour infiltration. This relationship between high T2W signal and infiltration of tumour cells is consistent with clinical results. Furthermore, histological studies show the potential of high infiltration in the high T2W signal region surrounding the CE-T1 enhancement region (Eidel et al., 2017). In addition, analysis of patient survival has shown a negative correlation with abnormal T2W volume (Zhang et al., 2014).

We have shown that perfusion MRI measurements made using mbASL can detect a larger tumour region than the other cMRI sequences. Therefore, it is suggested that perfusion may be used as a marker of infiltration of tumour cells. Clinical studies of MRI perfusion focus on regions beyond CE-T1 enhancement where a higher signal is expected because of angiogenesis. Lin et al. (2016) measured a negative perfusion gradient at the margins of metastatic regions that may be related to co-option or oedema. The significant relationship between the infiltrating tumour region and perfusion could facilitate the characterisation of marginal glioblastoma infiltration into healthy tissue.

The SNR of the perfusion by MRI could strongly affect the sensitivity of the detection. The perfusion gradient calculated from high SNR perfusion images could be used as a direct marker of tumour cell infiltration into the healthy tissue. This approach may lead to improved tumour delineation and might also lead to improved surgery and radiation therapy.

6.6 Limitations

This study has several limitations:

1- The quantitative analysis used a small number of mice as well as data acquisition and histology processing protocols that are expensive and time consuming.

2- There are differences between human gliomas and the G7 mouse model (immunodeficient mice), complicating any direct comparison. The immune status of G7 mice may slow tumour growth. However, it is unlikely to have a significant effect on the analysis of the relationship between local perfusion and tumour burden.

3- Features of MRI equipment in this work should be highlighted. The combination of 7 Tesla instruments with a novel perfusion sequence (mbASL) allowed SNR limitations of clinical perfusion imaging based on ASL sequences to be overcome, thus enabling the investigation of low perfusion regions.

6.7 Conclusion

This work found a negative relationship between tumour cell burden and perfusion MRI signals in infiltrative regions of low tumour cell density distant from CE-T1 enhancement regions. A novel histological protocol was employed to assess the performance of a range of MRI modalities, contributing a significant step toward quantitative and voxel by voxel evaluation of the ability of MRI protocols to probe regions of tumour cell infiltration. The results indicate that the relationship between perfusion gradient and tumour cell density can be used as a marker of tumour infiltration. Future work will concentrate on the application of this study to clinical settings. In addition, the application of machine learning may be useful when identifying the margins of invasive tumours.

Chapter 7

Investigating How to Optimally Combine Multi-parametric MRI Data to Detect GB Infiltration

7.1 Introduction

Glioblastoma is the deadliest, most aggressive, and most heterogeneous category of brain tumour. The invasive nature of glioblastoma, which is difficult to visualize, represents a major obstacle to its successful treatment and may be responsible for tumour recurrence.

Clinically, cMRI techniques (T1W, T2W, FLAIR and CE-T1) followed by qualitative visual evaluation are routinely used in the diagnosis and treatment plans of GB (Dominietto, 2014, Abul-Kasim et al., 2013). These sequences are used to identify the shape and location of the tumour and, possibly, any associated oedema and necrosis. However, these techniques do not have the ability to accurately detect the whole tumour region, which includes infiltration of tumour cells to adjacent tissue (Price and Gillard, 2011, Konukoglu et al., 2010).

Advanced MRI modalities such as Diffusion Tensor Imaging , Perfusion-Weighted Imaging , and MR spectroscopy now allow the detection of additional tumour phenotypes (Nandu et al., 2018), for example, neoangiogenesis, proliferation, cellularity and metabolism (Kalpathy-Cramer et al., 2014). These phenotypes may further support the ability to distinguish tumours from normal tissue that cannot be assessed by clinic MR imaging alone. Therefore, the combination of cMRI and advanced MRI modalities might improve detection of the whole tumour region, including adjacent regions infiltrated by tumour cells.

In recent years, mpMRI has gained renewed interest from the clinical research community. The combination of image data from various MRI modalities (morphological and functional) has the potential to provide the radiologist with a single tumour map, by extracting more information from the individual images (Kazerooni et al., 2015), for more details see Fig.7.1.

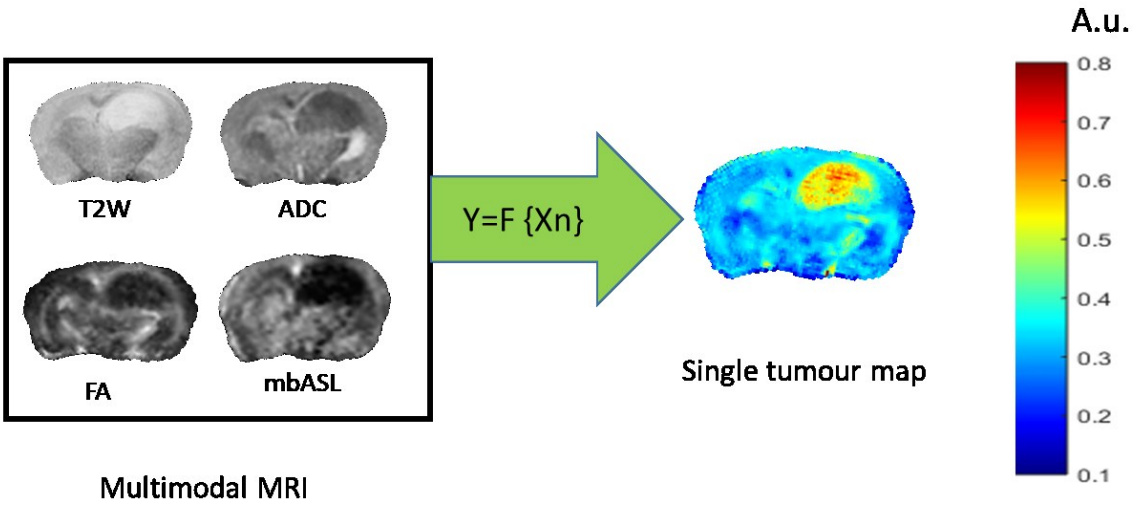

Figure 7.1: Reconstruction of a single tumour map from different MRI modalities (T2W, ADC, FA ,and mbASL).

The selection of which MRI modalities to use to create a single map depends on several factors, including the application and the particular disease. Both weighted and quantitative MR images have been found to detect, with varying degrees of success, the tumour's biological effects (Wu et al., 2010). Weighted images (T1W, T2W, and FLAIR) are not necessarily specific to the underlying biological state. Only qualitative differences in signal intensity can be used to detect pathology. On the other hand, quantitative MRI maps are often used when numeric values of signal intensities are measured, as they may increase the accuracy of the results. The quantitative MRI maps (e.g. ADC, FA, and CBF) are more closely related to the tissue pathophysiology. In this study, using a T2 map did not improve the detection of infiltration of tumour cells. In this work, a combination of weighted and quantitative MR images has been used, as shown in Chapter 4, to identify the whole tumour region, including the infiltration of tumour cells.

There are currently two strategies to analyse mpMRI data. The first involves extracting relevant features such as volume, signal intensity and texture, then applying a model to those factors (Wu et al., 2010). The second strategy is to perform a voxel-wise (voxel by voxel) analysis. The voxel-wise technique transforms voxel values from each imaging modality to create a single image map by applying either a linear or non-linear function (Fig.7.2).

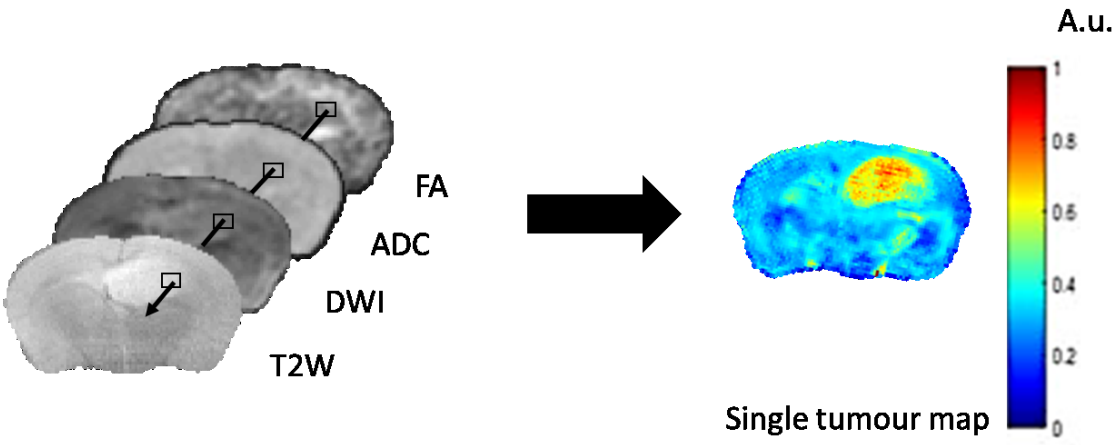

Figure 7.2: Schematic showing the voxel by voxel analysis method used to generate a single tumour map after co-register using MI method.

It has been hypothesised that mpMRI with qualitative evaluation can be used for better detection of the tumour region. However, this is difficult to prove in patients as the histology gold standard is not available, and biopsy is difficult in heterogeneous tumours as only a limited number of samples can be taken.

Kazerooni et al. (2015) proposed that using a combination of MRI images (ADC, PWI and T2W) followed by a segmentation method could find the extension of GB and could help in its delineation before surgery. However, it is difficult, when using this method, to accurately check the delineation of the tumour region. Further, several studies have recommended including additional imaging biomarkers adopted from diffusion and perfusion modalities, which might provide a deeper insight about the physiological behaviour of glial brain tumours (Chen, 2011, Kao et al., 2013). For example, Jensen and Schmainda (2009) stated that by combining several MRI modalities (morphological and functional) with a segmentation algorithm, they were able to distinguish between the invasion of the tumour and the normal tissue inside oedema. However, Vallatos et al. (2018a) found that invasion of tumour cells can be extended beyond the oedematous region by using a perfusion weighted image (ASL) in an infiltrative mouse model.

The purpose of the current study was to quantitatively test, for the first time, the hypothesis that mpMRI can better identify the tumour region than by using individual MR images. As discussed in the previous chapter, we have a unique dataset of co-registered MRI and histology (Al-Mubarak et al., 2019).

7.2 Regression analysis models

Regression is used widely in the medical field. It is a basic tool of medical statisticians to understand the degree of relationship or association between two continuous variables, X (independent) and Y (dependent). The built-in MATLAB function (regress) was used to calculate regression maps. The most common class of regression is linear regression. This function attempts to describe the relationship between Y and X as a straight line, as in Equation 7.1 (Quinn and Keough, 2002).

$$Y = b_{\circ} + b_1 X \qquad \text{Equation 7.1}$$

Equation 7.1 represents a straight line where b_0 is the intercept (y-axis) and b_1 represents the slope of the line (Fig.7.3A).

In many situations, the outcome (Y) does not depend on one variable, but on several variables (X_1, X_2, X_3….). The dependent variable (Y) might well be associated with a number of independent variables X_1,X_2,X_3,…X_n, (Steele et al., 2016) . In this case, multiple linear regression analysis can be performed. This is called interactive regression (Equation 7.2).

$$Y = b_{\circ} + b_1 X_1 + b_2 X_2 + b_3 X_1 X_2 + \cdots \qquad \text{Equation 7.2}$$

Where X_1, X_2, X_3,…X_n are predictor variables, and b_o,b_1,b_2,….b_n are regression coefficients.

Quadratic regression turns a linear regression model into a curved shape. It still qualifies as a linear model because X is squared. A quadratic term creates a parabolic shape, Fig.7.3B. Multiple quadratic regression can be written as follows:

$$Y = b_{\circ} + b_1 X_1 + b_2 X_2 + b_3 X_1 X_2 + b_4 X_1^2 + b_5 X_2^2 + .. \qquad \text{Equation 7.3}$$

Finally, cubic regression is a type of regression analysis where the relationship between the variables (X and Y) is modelled as an nth degree cubic in X (Fig.7.3C). Multiple cubic regression can be written as follows:

$$Y = b_{\circ} + b_1 X_1 + b_2 X_2 + b_3 X_1 X_2 + b_4 X_1^2 + b_5 X_2^2 + b_6 X_1^3 + b_7 X_2^3 + \cdots$$ Equation 7.4

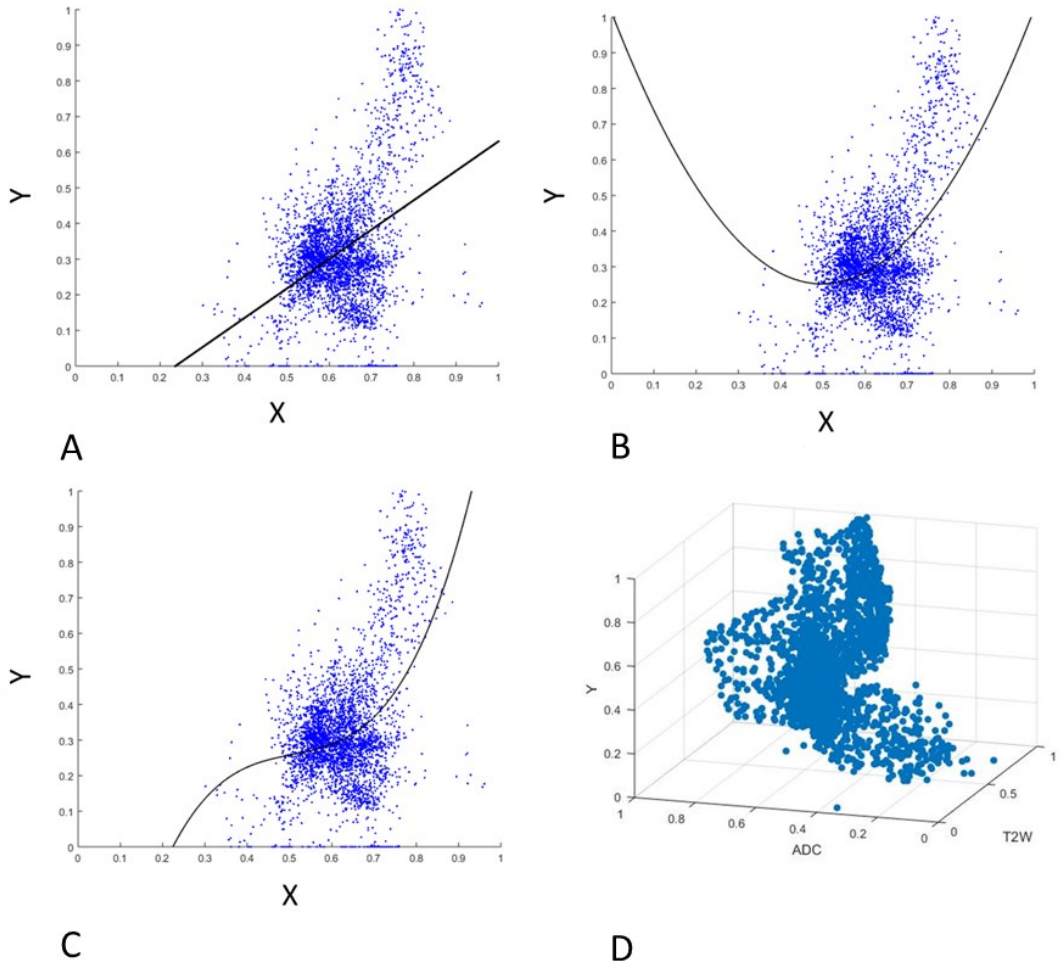

Figure 7.3: Examples of (A) Linear regression. (B) Quadratic regression, (C) Cubic regression with one dependent variable (X) and (D) Independent variable (Y) with two dependent variables (T2W and ADC).

7.3 MRI pre-processing

The first step in pre-processing images in this study was the application of a filter which was used to remove noise and enhance the quality of the image. A nonlinear diffuse filter was applied to reduce the noise and revise the edges in the image (iterations=100, and λ=0.2). The MATHLAB code is adapted from Demirkaya et al. (2008). Image analysis processing requires a standardized intensity range for the

MR images in order to achieve the accuracy and efficiency of measurements. The normalization equation used in this work is:

$$z = \frac{x - m}{\sigma} \qquad \text{Equation 7.5}$$

Where z is the voxel's new value, x is the original value, *m* is the mean value, and σ is the standard deviation of the voxel values in the whole brain section.

The regression models use the histology and mpMRI input data to find the best fitting coefficients to create a regression map. First, the model will calculate a regression map by calculating the regression coefficients (b_i). Where Y=SIH and X_1=T2W, X_2=ADC… X_n. Next, these coefficients (b_i, where i=1,2,3…n) from the previous step are used to generate a regression map (Y). Figure 7.4 summarizes the pre-processing steps in this study.

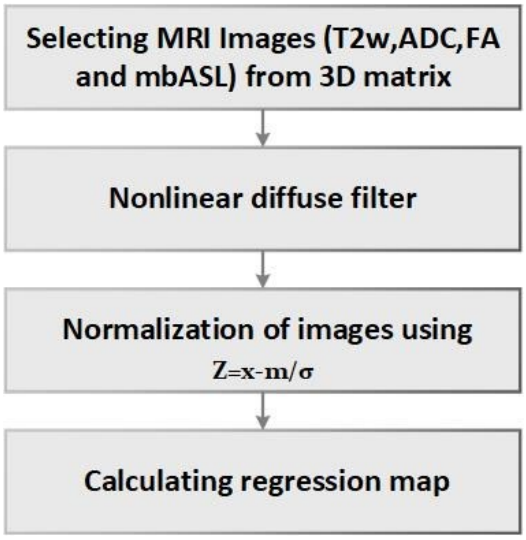

Figure 7.4: Image-processing pipeline to create a regression map after applying nonlinear diffuse filter and image normalization.

Regression equations, such as the linear Regression Method (LRM), equation 7.1, Interactive Regression Method (IRM), equation 7.2, Quadratic Regression Method (QRM), equation 7.3 and Cubic Regression method (CRM), equation 7.4, were used to produce a regression map. These equations are applied to find the best combination between MR data (T2W, ADC, FA and mbASL) to represent the tumour region.

7.4 Statistical analysis

The performance of regression methods was evaluated using three statistical methods:

1. The Pearson coefficient method is useful to identify if two or more variables are related to each another. A correlation coefficient (r) is a numerical assessment of the strength of the relationship between the X and Y values in the data set consisting of (X, Y) pairs, as in equation 7.6.

$$r = \frac{\Sigma XY - (\Sigma X)(\Sigma Y)}{\sqrt{[N\Sigma X^2 - (\Sigma X)^2][N\Sigma Y^2 - (\Sigma Y)^2]}} \qquad \text{Equation 7.6}$$

Where N is the total number of variables.

2. In our study, to test the accuracy of each method, we also compared manually delineated volumes of interest (VOI) selected from the different regression maps with the VOI selected from the corresponding SIH map.

3. The most common method of computing the image texture is the histogram. It can provide quantitative information on momentum (mean, standard deviation, skewness, variance, and kurtosis) that is not visible to the human eye. In this study, the normalized Probability Density Function (PDF) was calculated from the histogram by dividing the PDF by the area under the curve. The mean, variance, skewness, and kurtosis of normalized PDF was then calculated according to the following equations:

$$M_n = \int_{-\infty}^{+\infty} f(x)(x - c)^n \, dx \qquad \text{Equation 7.7}$$

Where f(x) is the normalized variable value and c is grey level values. The first moment is termed the mean of the PDF (n=1), the second moment the variance (n=2), the third moment the skewness (n=3) and the fourth moment the kurtosis (n=4).

$$\text{Variances} = \int_{-\infty}^{+\infty} f(x)(x-c)^2\,dx \qquad \text{Equation 7.8}$$

Skewness refers to the asymmetry of the PDF. If the distribution is symmetric the skewness value is zero. A distribution with an asymmetric tail extending to the right is referred to as being positively skewed, while a distribution with an asymmetric tail extending to the left is referred to as negatively skewed. The skewness of a distribution is defined as follows:

$$\text{skewness} = \int_{-\infty}^{+\infty} f(x)(x-c)^3\,dx \qquad \text{Equation 7.9}$$

Kurtosis is a measure of how flat or peaked a frequency-distribution curve is when compared with the normal distribution. If the distribution is similar to the normal distribution, the kurtosis value is 3.

$$\text{kurtosis} = \int_{-\infty}^{+\infty} f(x)(x-c)^4\,dx \qquad \text{Equation 7.10}$$

GraphPad Prism software (Inc., version 6.0, CA, USA) was used to perform statistical tests and to produce graphs which display mean values' ± standard deviation. Significance was tested using an unpaired Student's *t*-test with Bonferroni correction.

7.5 Results

This study was conducted with the principal aim of finding the best combination of MRI modalities (T2W, ADC, FA, and mbASL) to extract the tumour region after co-registration with stacked in-plane histology (SIH). Regression models were used to analyse these data.

The average of b coefficients for all mice cannot be used to recreate multi-regression maps for each mouse because of big variation of b coefficients (standard deviation) of the b's coefficients average of. The Table 7.1 shows the b coefficients of CRM (T2W, ADC, FA and mbASL), QRM (T2W, ADC, FA and mbASL) and IRM (T2W, ADC).

MRI	b coefficients	CRM T2w,ADC,FA, mbASL	QRM T2w,ADC,FA, mbASL	IRM T2W+ADC
		mean± STD	mean± STD	mean± STD
	b0	-0.03± 0.12	-0.11± 0.36	-0.93± 0.69
T2W	b1	-0.21± 1.61	0.31± 0.94	1.74± 1.00
ADC	b2	0.97±1.26	0.97± 0.59	1.61± 1.08
FA	b3	0.67± 0.96	0.98± 1.01	
mbASL	b4	-1.12± 1.12	-1.18± 1.16	
T2W+ADC	b5	0.46±3.00	0.74± 1.41	-2.07± 1.56
T2W+FA	b6	0.06± 1.44	0.02± 1.13	
T2W+mbASL	b7	-1.66± 1.97	-0.30± 1.02	
ADC+FA	b8	-0.68± 1.75	-1.33± 1.38	
ADC+mbASL	b9	2.06±2.54	1.43± 1.51	
FA+mbASL	b10	0.09±0.63	-0.001± 0.63	
T2W+T2W	b11	2.61±5.03	-0.21± 1.18	
ADC+ADC	b12	-2.20± 5.64	-1.23± 0.72	
FA+FA	b13	-0.26± 1.16	-0.23± 0.34	
mbASL+mbASL	b14	1.77± 1.87	0.55± 0.75	
T2W+T2W+T2W	b15	-2.39± 3.79		
ADC+ADC+ADC	b16	0.97± 3.18		
FA+FA+FA	b17	0.03±0.86		
mbASL+mbASL+mbASL	b18	-1.00± 1.42		

Table 7.1: The multi-regression coefficients (b_i) of IRM, QRM and CRM.

7.5.1 Visual analysis

Figure 7.5 shows a visual comparison between the original images (FA, ADC T2W, and mbASL) and the regression maps, LRM, IRM, QRM and CRM. Visual inspection shows a significant improvement in tumour region detection in both CRM and QRM maps compared with LRM and IRM maps.

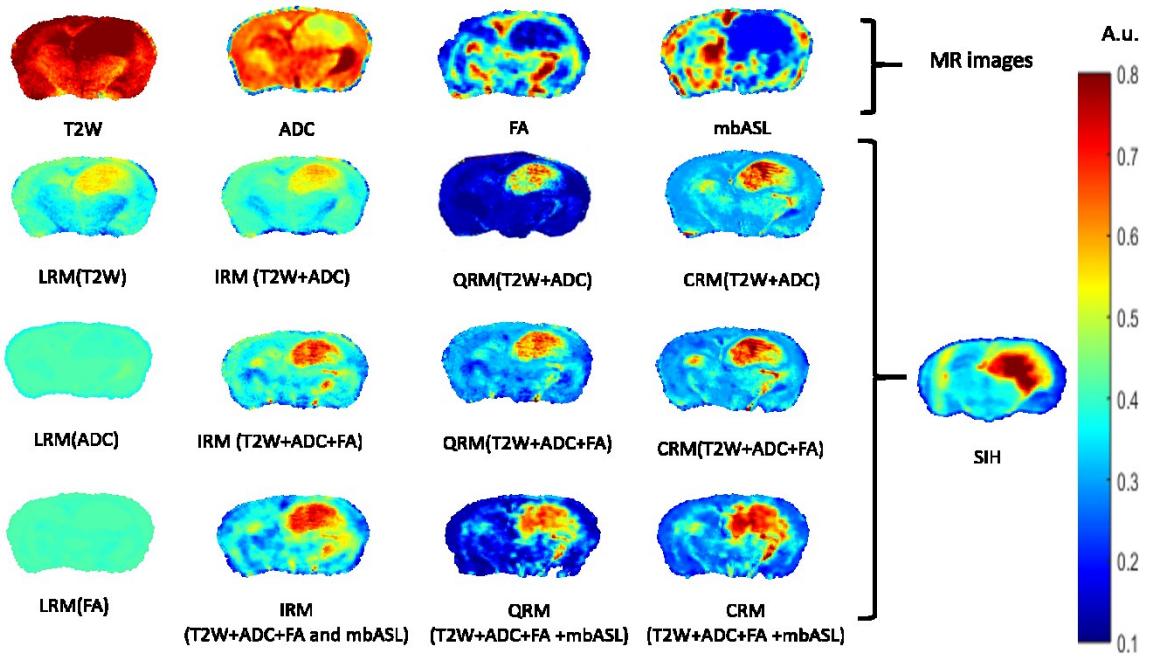

Figure 7.5: Comparison of original MR images (T2W, ADC, FA, and mbASL) and LRM, IRM, QRM, and CRM derived single tumour maps (a.u).

7.5.2 Pearson correlation

Figure 7.6 shows a comparison of correlation coefficients between different regression methods (LRM, IRM, QRM and CRM) and the SIH 'ground truth'. This figure clearly shows that QRM and CRM have higher correlation coefficients ($r>0.5$) than LRM and IRM. According to (Oppo et al., 1998), the following clinically relevant r values were used: an r value less than 0.4 was considered poor, an r value of 0.4-0.59 was considered fair, an r value of 0.6-0.74 was considered good, and an r value greater than 0.74 was considered excellent.

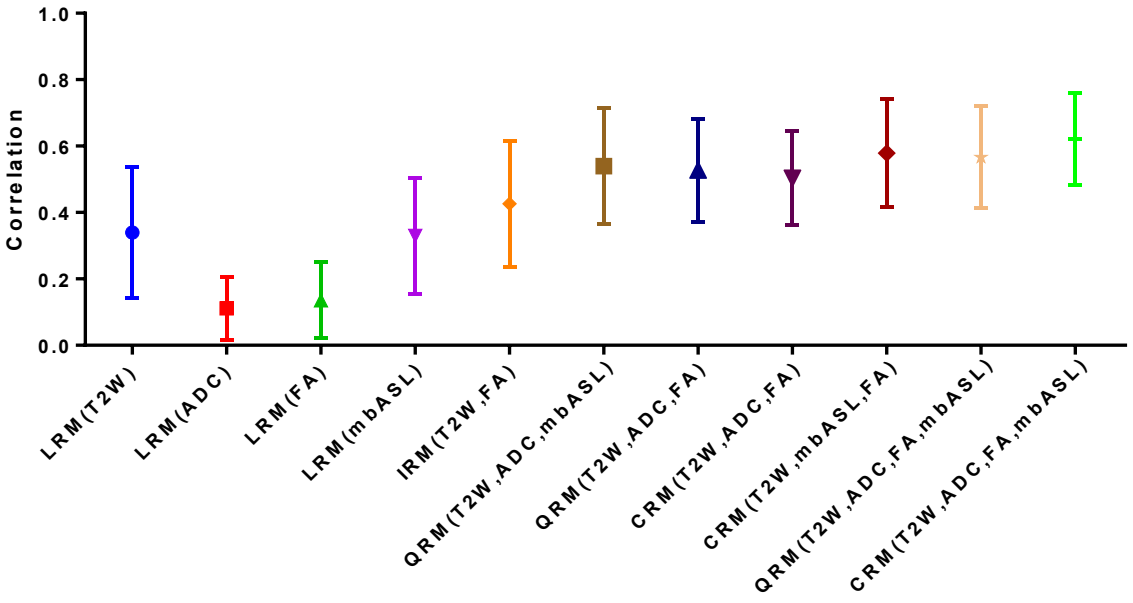

Figure 7.6: Comparison between regression maps and SIH in the brain using the Pearson correlation after discarding the background. This figure shows that QRM and CRM best correlate with the SIH maps (r>0.5).

7.5.3 Volumetric analysis of tumour

The analysis of tumour volume is a powerful tool for studying the effects of cancer treatment. However, in this work, we use tumour volume to compare between multi-regression maps and histology (SIH). The tumour Volume of Interest (VOI) for nine mice was obtained by manual delineation of both regression maps and the corresponding SIH map, by two observers; both with more than 3 years' experience (see Fig.7.7).

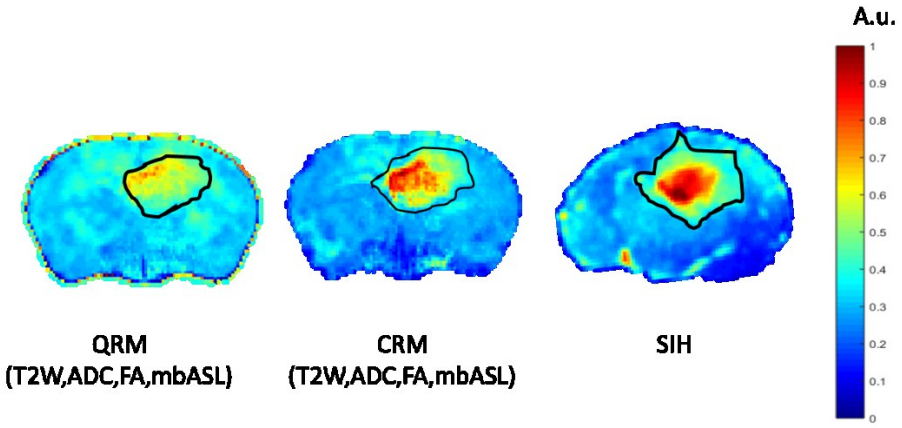

Figure 7.7: Volumetric analysis of tumour. VOIs are manual selections between different regression models (QRM and CRM).

The tumour volumes were calculated after counting the number of pixels within the tumour boundaries for both multi-regression and SIH and multiplying them by the pixel volume to obtain the tumour volume in mm^3.

Figure 7.8 shows the average and STD of tumour volumes manually delineated from the individual MRI maps, multiple regression maps and histology (SIH). The figure demonstrates that multi-regression maps that were created from four MRI modalities with a quadratic or cubic regression map is closer to SIH than other regression types.

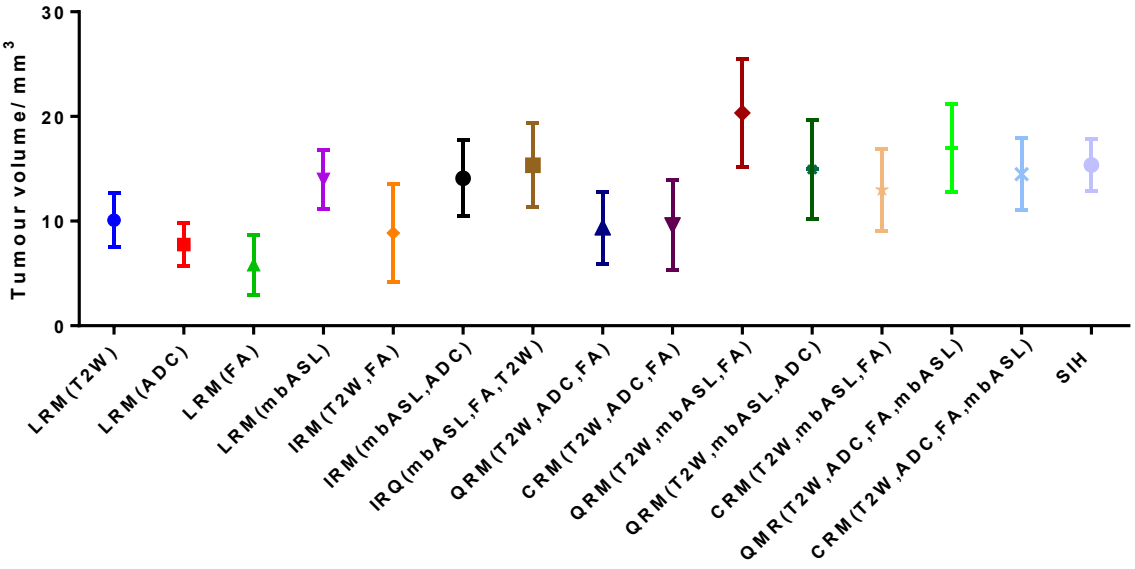

Figure 7.8: Comparison of volumetric analysis between multiple regression maps and SIH.

According to the results in Fig.7.8, we decided to focus on three or four MRI modalities with a quadratic or cubic regression map. Figure 7.9 shows the average and standard deviation of tumour volumes for four MRI modalities with a quadratic or cubic regression map at week 12. The mean tumour volumes selected by QRM (16.98±4.18 mm^3) and CRM (14.49±3.46 mm^3) exhibited no statistically significant difference, except for QRM (T2W, ADC and FA) when compared with SIH average volume (14.2±2.89 mm^3). This comparison proves statistically that both QRM and CRM are suitable to describe SIH.

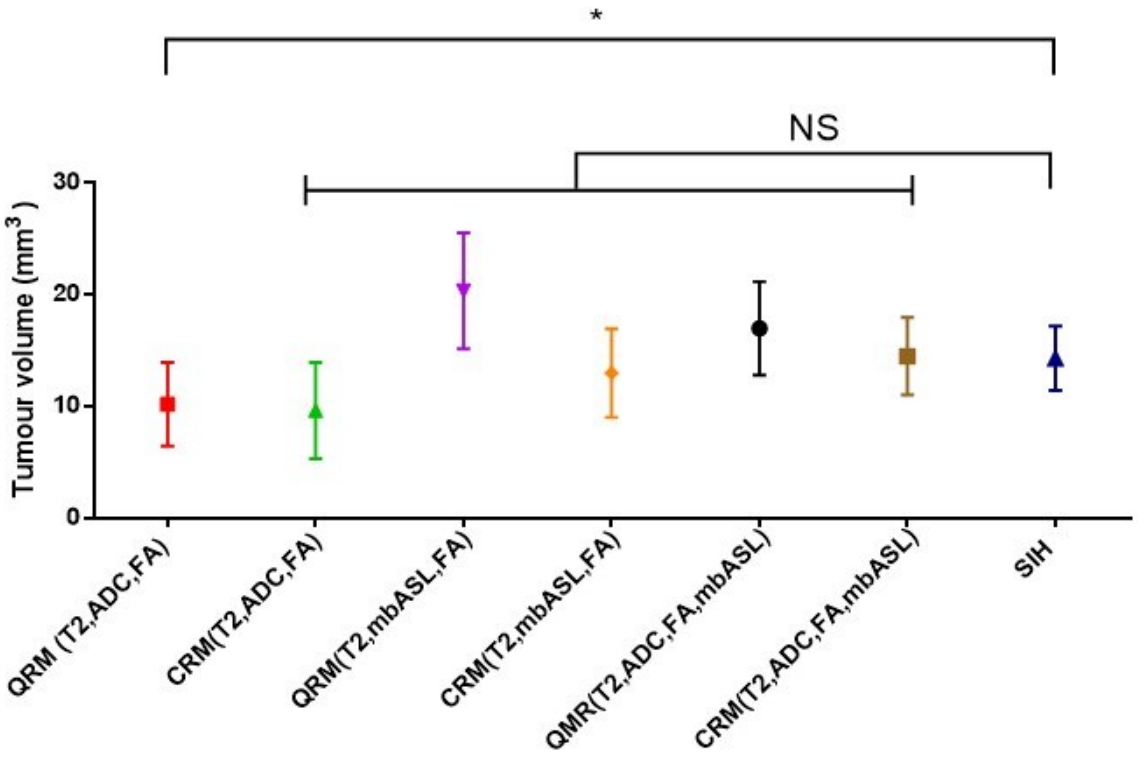

Figure 7.9: Statistical analysis using Student's t-test with Bonferroni correction shows that there is no statistical significance between QRM, CRM and SIH determined tumour volumes (p> 0.008). * Statistical significance (p<0.0083); NS = no statistical significance.

7.5.4 Probability density function analysis

The statistical approach of texture analysis using grey-level distribution within an image is the most widely used method in medical applications. Statistical methods can be used to analyse the spatial distribution of pixel grey values in medical imaging. Figure 7.10 shows a comparison between the PDFs of CRM and SIH for two mice.

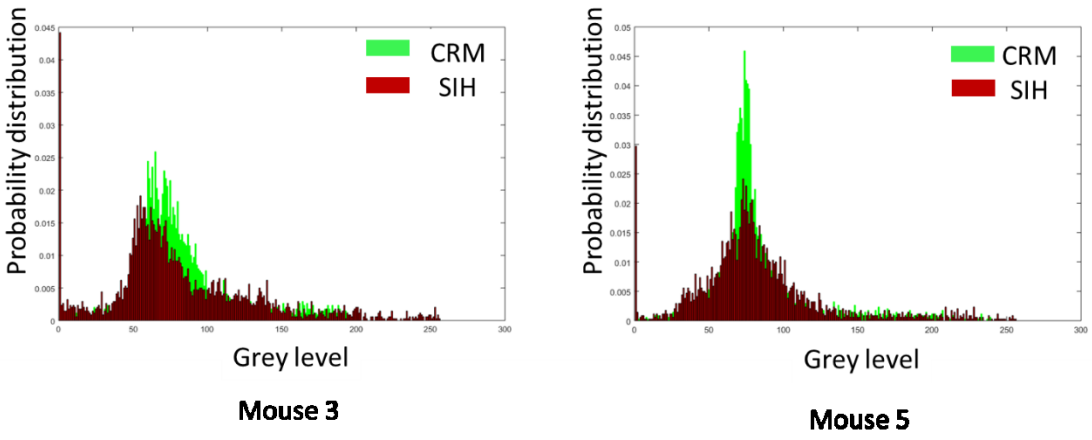

Figure 7.10: Comparison of normalised probability density function between CRM and SIH for whole brain.

The computation of global features is derived from the histogram of image pixel grey values. These features are average, STD, kurtosis and skewness of the image and these statistical features can be used to find similarities between two images.

In the previous section, QRM and CRM tumour maps were shown to be best able to identify the tumour region. Hence, this section will focus on those two tumour maps. For each map, we calculated the following features: (1) mean, (2) standard deviation, (3) skewness, and (4) kurtosis of the PDF. These measurements were calculated from a normalised PDF of the whole brain region. The PDF features showed that there was no statistical significance ($p>0.025$) observed in the mean, standard deviation, and skewness between QRM, CRM and SIH. It is a good indicator that, when compared with SIH, CRM shows most of the tumour region. Figure 7.11 summarizes the results in graph form for each of the PDF features.

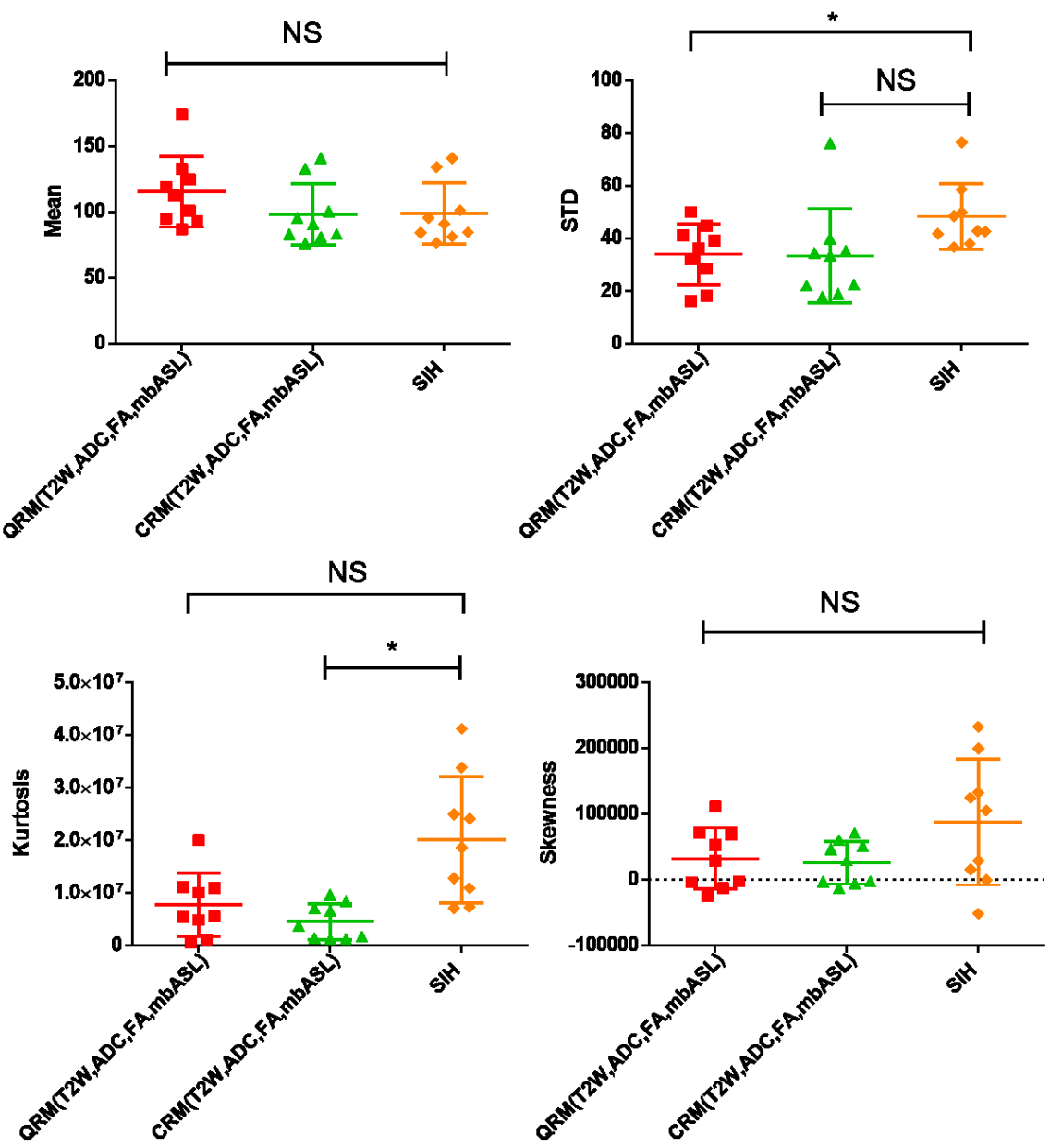

Figure 7.11: Volumetric comparison (mean and STD) between QRM, CRM and SIH shows that CRM describes SIH better than QRM. Statistical comparisons were made using a student's *t-test* unpaired with Bonferroni correction. * = statistically significant (p<0.025); NS = not statistically significant.

7.6 Discussion

The availability of different MRI pulse sequences yields varying contrasts that can be used to diagnose GB. However, these individual contrasts do not discriminate well between tumour cells and normal tissues using clinic MRI. It has been hypothesised that mpMRI can be used to better detect the tumour region (Marino et al., 2018). The purpose of the current study was to quantitatively test this

hypothesis for the first time, using a unique dataset of co-registered MRI and histology (Al-Mubarak et al., 2019).

Figure 7.5 shows a comprehensive visual comparison between MR imaging, regression maps, and SIH. Interestingly, regression maps for QRM and CRM show the best visual comparison with SIH. The QRM and CRM regression maps can clearly distinguish between the tumour region and normal tissue, which allows us to delineate the outline of the tumour boundary for the next steps.

The correlation coefficient is a statistical measure that calculates the strength of the relationship between variables, with values ranging between 0 and 1. The correlation between QRM, CRM and SIH is larger than 0.5, which is considered a good correlation (for more details see Fig.7.6). In fact, the high correlation between CRM, QRM and SIH allows us to clearly distinguish the tumour outline, including any infiltration region.

Quantitative image analysis and statistical methods can quantify precise parameters of the region. These parameters might include area, volume, intensity, roundness, and other physical features. For example, the volume of tumour can be quantitatively measured and validated with a mesoscopic scale (histology). Volumetric analysis (Figs. 7.8 and 7.9) indicates that tumour volumes which are extracted from QRM (16.98±4.18 mm^3) and CRM (14.5±3.48 mm^3) maps and from MR images (T2W, ADC, FA and mbASL) are not statistically significant ($p>0.0083$) when compared with tumour volumes derived from histology SIH (15.73±2.54 mm^3). However, the selection of tumour volume is limited by several factors such as the partial volume effect and the contrast of the tumour against the background.

A histogram is used to describe the voxel intensity distribution between two images. Figure 7.10 shows a normalized PDF calculated from the corresponding histogram to visually compare CRM and SIH mouse brain images. In Fig.7.11, the PDF parameters, including mean, standard deviation, skewness (a measure of asymmetry of the probability distribution), kurtosis (a measure of the shape of the probability distribution), were extracted and compared. The analysis shows no statistical significance between CRM and SIH (for mean, STD, and skewness with the exception of kurtosis $p>0.025$). We conclude that CRM is better at describing

SIH than QRM. The limitation is that the histogram's measurements do not provide information regarding the relative spatial position and intensity distribution of voxels to one another. This can be achieved by using a grey level co-occurrence matrix (second-order of texture).

7.7 Conclusion

Using a unique dataset of co-registered MRI and histology maps for a mouse model of GB, the hypothesis was tested using a voxel-by-voxel multiple regression analysis. For the first time we are able to conclude that mpMRI is better at identifying the whole tumour region than when using individual MR images alone. Development and translation of such techniques could allow improved brain tumour diagnosis, prognosis, and monitoring.

7.8 Future directions

Adding new imaging modalities such as MRS or PET to identify more tumour characteristics and metabolic parameters would provide additional insight into various biological mechanisms occurring within the tumour. For example, MRS imaging can measure glucose metabolites that may allow detection of extra phenotypes of tumours (Di Costanzo et al., 2006) that cannot be detected by morphological and functional MRI techniques.

Future studies should concentrate on using quantitative information from mpMRI to create computer assisted diagnostic software. This information could help radiologists in their reporting. Such technology, combined with special training in tumour mpMRI, may help to improve inter-observer variability and increase the accuracy of reports.

Chapter 8

General Discussion and Conclusion

8.1 Discussion

This thesis addresses the problem of detecting glioblastoma invasion beyond the oedema region by using several MRI techniques. Two methods were proposed to detect brain tumour invasion. The first method used perfusion weighted imaging derived from mbASL as a biomarker of tumour invasion. The second method used mpMRI from T2W, ADC, FA and mbASL with multi-regression analysis to reconstruct a single tumour map for better detection of the tumour region, including infiltration of tumour cells beyond the oedema. However, these methods require a quantitative ground truth model in order to assess with MRI. Therefore, it was decided to develop a new validation method, where MR images are co-registered with 'stacked in-plane histology', which allows for quantitative and voxel by voxel analysis.

It is widely accepted that histology is the gold standard to study of the microscopic structure and functional of biological tissues. A key step during the development of an imaging biomarker is to validate the signal measured *in vivo*. Histology is commonly used as a ground truth during the preclinical development of an imaging biomarker in order to validate that the signal detected *in vivo* corresponds to the underlying tissue of interest. In animal models of disease, histology is widely used to highlight neuropathological markers of brain tumour that can be used to validate MRI. However, most of these validations are done by visual inspection (qualitative) which may influence pathologists' opinion. This type of analysis is not sufficiently accurate, because many biologically relevant features cannot be easily identified and analysed by the human eye. For example, the different nucleus size of two tumours, delineation of the volume of high glioma grade and so on. On the other hand, quantitative validation methods for the analysis of the brain section for cellular and pathological markers may solve this issue.

In chapter 5, the methods currently used to validate non-invasive imaging biomarkers were inadequate. Therefore, it was decided to develop a new method of combining multiple histology sections, cut in the MRI plane. This "stacked in-plane histology" then better represents the actual imaging slice, which is often orders of magnitude thicker than histology.

This approach of improving the quality of the histological technique was shown to be far superior when compared to the traditional single slice approach, typically employed in validating non-invasive imaging (MRI).

The proposed model 'stacked in-plane histology' was used to quantitatively validate different MRI modalities as imaging biomarkers of GB. For example, SIH has proved that MRI is not accurate to detect whole tumour region by comparing regions of different MRI modalities (T2W, DWI, and ADC) with SIH. Also, tumour volume measurements made by SIH maps display a lower standard deviation which allows for better validation with MRI. The lower stander deviation of SIH tumour volume measurements has important implications such as reduced the number of the animals in the experiment which is agreed with police of Replacement, Refinement and Reduction of Animal in research.

Several studies attempt to use a quantitative analysis between MRI and histology. One of these studies was carried out by (Jardim-Perassi et al., 2019). They used an MRI-guided 3D printer to facilitate the register of MRI with histology to enable the evaluation of the MRI habitat. Where is other studies carried out by using co-register MRI with histology to improve the capabilities of non-invasive imaging to characterise cancerous tissue (Alic et al., 2010, Chappelow et al., 2007). However, these studies were limited by not accounting of histology section thickness and orientation.

The SIH could be used to assess the performance of a range of MRI modalities and it is a significant step toward quantitative and voxel by voxel evaluation of ability of preclinical MRI protocols to probe tumour and evaluation treatment plan. According to our knowledge, this is a first time using histology for quantitative and voxel by voxel evaluation of MRI modalities which open door for accurate and new applications.

In chapter 6, a negative correlation between the tumour cells burden at an early stage and perfusion of MRI signal, was discovered in the infiltration region beyond the contrast enhance region. Perfusion measurements exhibited the largest tumour regions in this early stage of infiltration model, confirming the strong links between tumour infiltration and small host vessels reported elsewhere (Geer et al., 2012). Clinical studies tend to focus on the regions surrounding CE-T1

enhancement where the ASL signal is expected to be stronger because of angiogenesis. Several clinical researchers have studied cerebral blood flow in the marginal tumour regions. For example, Lin et al. (2016) observed a negative perfusion gradient at the margins of metastatic regions that could be related to the co-option. Blasel et al. (2011) found that cerebral blood volume (rCBV) increased in the region adjacent to the contrast enhancement on MRI of glioblastomas. However, the results in this chapter show that there is a negative relationship between perfusion and infiltration of tumour cells and tumour cell are infiltrated beyond the oedema region. Later, this result has been confirmed by using a human study which have been done by (Noth et al., 2019). They found that quantitative T1map differences between pre and post gadolinium contrast agent are better for detecting infiltration inside and beyond the peritumoral oedema of glioblastomas.

To observe angiogenesis in a preclinical model it is necessary to reproduce solid tumour conditions (e.g. significant tumour burden, hypoxia). However, these conditions require either a non-infiltrative model that lacks realism or a considerable size of tumour, thus compromising animal survival. Most infiltrative preclinical models will therefore tend to present a phase of vascular co-option that can lead to a detectable perfusion drop (Cha et al., 2003). As far as can be established, this is the first-time perfusion MRI has been suggested an imaging biomarker of tumour cell infiltration beyond CE-T1 and even T2W enhancement regions. In this work, the infiltration-related drop in perfusion was confirmed both by perfusion and histology. The significant relation observed between infiltrated tumour burden and perfusion at the margins suggests that probing abnormal perfusion gradients far from the CE-T1 enhancement regions could facilitate the characterisation of marginal glioblastoma infiltration into healthy tissue.

In chapter 7, the first use of mpMRI with multi-regression analysis to improve the delineation of tumour regions of orthotopic G7 tumour growth in mice was proposed. In recent years, there has been a growing trend in designing *in vivo* neuroimaging to prognostic and diagnostic of brain tumour. Many of studies have reported promising prediction performances with the claim that brain tumour can be diagnosed robustly and accurately. For example, cMRI which includes T2W, CE-T1, DWI and FLAIR is an excellent non-invasive imaging tool to longitudinally assess

morphological and functional changes in a brain tumour. However, individual cMRI is not accurate to probe whole tumour region specially infiltration of tumour cells.

Quantitative MRI maps (qMRI) are often used when numeric values of signal intensities are measured and they are more closely related to the tissue pathophysiology. The combination of the different quantitative MRI techniques (DTI, CBV, CBF, T2map and T1map) could increase the accuracy of the results. However, in this study, T2map couldn't improve the detection of infiltration of tumour cells. Therefore, the decision has been made to remove it from the study and replace with T2W.

The combination of several MRI modalities using mpMRI may overcome the limitations of each individual modality and provide morphological, functional, and molecular information about tumour. The combination of different MRI modalities allowed complementary assessment of tumour growth characteristics, including total tumour volume and infiltration of tumour regions beyond the oedema. However, until now, mpMRI have not been fully integrated into the clinic, based to our knowledge, the main reason for this is that are not assessed be histology, amount of post-processing analysis required, lack of clinical trial data, and lack of radiology training (Hyare et al., 2017).

In this chapter, computer has given ability to solve the problem of accurate detection of tumour boarders by Machine learning. Machine learning studies could be revolutionary to detect infiltration of tumour cells, For example, the multi-regression method could be used to find a relationship between dependent (histology) and multiple independent variables (MRI) and multi-regression coefficients (b_i) which are calculated by using this method can be used later to reconstruct a single tumour map. Unfortunately, using average of these coefficients and for all mice to reconstruct a single tumour map has failed due to a huge variation between these coefficients. However, using average of multiple variables linear regression model coefficients to reconstruct a single tumour map give us better results.

Another advantage co-registering MRI with histology, is that it enables quantitative analysis via a voxel-wise approach. This allows for the exploration of more ROIs than would be possible with manual selection. Voxel-wise analysis

pushes exploratory analysis even further by enabling analysis at the voxel-level. This enables the detection of effects that cannot be easily–characterised by ROIs such as; local effects or diverging effects within a close region. For example, in chapter 6 and 7, voxel-wise analysis was used to detect the tumour region, including infiltration of tumour cells into normal tissue.

8.1.1 Limitations

With hindsight and reflection, a number of limitations have been identified in this thesis:

1- Only one mouse model of GB was employed. It would have been preferable to have used multiple models, which could have provided a more vigorous test of our methods.

2- Animals were only scanned at two time point (9 weeks and 12 weeks). It would have been preferable to have more time points to analyse and compare the results in the early and later stages of tumour invasion.

3- Another limitation of this study is the lack of quantitative longitudinal histology. Histology at different time points would have provided concrete evidence of the various morphological and functional changes occurring within the tumour rather than the processes based on last time point histology. This could have been achieved by having several groups of animals, with each group terminated at a different time point.

8.2 Conclusion

The main aim of this thesis was to develop quantitative medical image analysis methods that allow for quantitative assessment imaging biomarkers with the ground truth (histology). Though these methods can be applied to any disease model, we initially chose to apply them to an infiltrative glioblastoma mouse model. Furthermore, developing a new quantitative medical image analysis method to improve the delineation of tumour regions including infiltrative regions, may lead to the improvement in therapy planning, assessment of drug treatments and identifying the chances of patients developing future complications.

This thesis proposed several scientific contributions to the main components of medical imaging analysis. The summary of these contributions and potential future directions are provided as follows:

Firstly, histology is the ground truth of assisting non-invasive imaging biomarking. However, most of the validation approach involves visual inspection (qualitative). Therefore, it was decided to develop a new technique to advance the quality of histology. Multiple histological sections were cut in the MRI imaging plane and thickness to produce a stacked in-plane histology map that can be used as the best available ground truth with which to quantitatively validate imaging biomarkers. A high-level accuracy of co-register histology and MRI allows for the application of quantitative and voxel by voxel analysis comparison between MRI mortality and histology. For example, a quantitative volume comparison between clinical MRI and histology shows that clinic MRI cannot detect a whole tumour region especially infiltrative tumour cells in normal tissue. This study highlighted the importance of histology section thickness to measure of tumour volume because assessment based exclusively on single histology section was not reliable and did not truly reflect the GB extension in each animal.

Secondly, in chapter 6, this study identified that a negative relationship between tumour cell in the margins of tumour and cerebral perfusion, which can potentially be used as an imaging biomarker for tumour invasion beyond oedema region. In addition, this chapter indicated that cMRI is not useful in the detection of the invasion of tumour cells beyond the oedema which may be responsible for tumour recurrence after surgery.

The robust protocol that were developed to assess the performance of a range of MRI modalities by using histology is a significant step toward quantitative evaluation of the ability of preclinical MRI protocols in to probe regions of infiltration of tumour cells.

Thirdly, chapter 7 demonstrated that mpMRI, coupled with multi-regression analysis, allows assessment of the detectability of tumour infiltration by assessment of relaxation, diffusion, and perfusion properties, potentially allowing better delineation of the infiltrative region beyond the peritumoural oedema region. Development and translation of such a technique, which strengthens the

links between *in vivo* imaging biomarkers and the structural / functional properties of tissue, has the potential to provide predictive models to improve brain tumour prognosis, and monitoring. This approach shows much promise in probing the boundaries of tumour cell infiltration in glioblastoma.

8.3 Future directions

The potential future direction of development in the detection of tumour cells beyond the oedema region by quantitative medical image analysis is shown below:

1- The quantitative analysis of the multimodality of MRI images which can significantly increase the accuracy of tumour detection requires further investigation.
2- PET/MRI is a hybrid imaging technology that incorporates MRI soft tissue morphological and PET functional imaging. It can provide both anatomical and metabolic information about abnormal tissues which is useful for tumour diagnosis and delineation. MRI that is integrated with different medical image modalities will benefit disease diagnosis, therapy evaluation and drug assessment. It is anticipated to be one of the most promising topics in the future.
3- The potential role of multi-parametric MRI in the delineation of glioblastoma has been highlighted by the results in chapter 7 of the thesis. Notwithstanding this, further investigation is required in the future. Future research should concentrate on adding quantitative MRI techniques such as CBF, CBV and semi-quantitative DCE.
4- Computer assisted diagnostic software should be developed to help radiologists to diagnose. Techniques such as this combined with specialist training in tumour detection and delineation may help to improve inter-reporter variability and hence consistency in reporting.
5- The next steps arising from chapter 7 will be to take multiple regression analyses to use as guide for potential future studies involving novel therapies and the assessment of efficacy.
6- Recently, machine learning has seen a huge development that leading to a lot of interest from medical field. Train artificial neural networks by using histology ‘ground truth’ can be more accurate and less time consuming.

7- One of promising technique to analysis the data is radiomics which is refers to the extraction and analysis of large amounts of imaging features. These features have the potential to find disease characteristics that fail to be appreciated by the pathologist's eye.

9.1 References

ABUL-KASIM, K., THURNHER, M., PUCHNER, S. & SUNDGREN, P. 2013. Multimodal magnetic resonance imaging increases the overall diagnostic accuracy in brain tumours: Correlation with histopathology. *South African Journal of Radiology,* 17**,** 4-10.

AGARWAL, N., XU, X. & GOPI, M. 2016. Robust registration of Mouse brain slices with severe histological artifacts. *Tenth Indian Conference*. India.

AL-MUBARAK, H., VALLATOS, A., GALLAGHER, L., BIRCH, J. L., GILMOUR, L., FOSTER, J. E., CHALMERS, A. J. & HOLMES, W. M. 2019. Stacked in-plane histology for quantitative validation of non-invasive imaging biomarkers: Application to an infiltrative brain tumour model. *J Neurosci Methods,* 326**,** 108372.

ALIC, L., HAECK, J. C., KLEIN, S., BOL, K., VAN TIEL, S. T., WIELEPOLSKI, P. A., BIJSTER, M., NIESSEN, W. J., BERNSEN, M., VEENLAND, J. F. & DE JONG, M. 2010. Multi-modal image registration: matching MRI with histology. *Medical Imaging 2010: Biomedical Applications in Molecular, Structural, and Functional Imaging,* 7626**,** 762603.

ALTIOK, N., ERSOZ, M. & KOYUTURK, M. 2011. Estradiol induces JNK-dependent apoptosis in glioblastoma cells. *Oncol Lett,* 2**,** 1281-1285.

ATKINSON, A., COLBURN, W., DEGRUTTOLA, V., DEMETS, D., J, D. G., HOTH, D., OATES , J. A., PECK, C. C., SCHOOLEY, R., SPIKER, B., WOODECOCK, J. & ZEGER, S. 2001. Biomarkers and surrogate endpoints: preferred definitions and conceptual framework. *Clin Pharmacol Ther,* 69**,** 89-95.

AXEL, L., COSTANTINI, J. & LISTERUD, J. 1987. Intensity correction in surface-coil MR imaging. *AJR Am J Roentgenol,* 148**,** 418-20.

BALAFAR, M. A., RAMLI, A. R., SARIPAN, M. I. & MASHOHOR, S. 2010. Review of brain MRI image segmentation methods. *Artificial Intelligence Review,* 33**,** 261-274.

BALDOCK, A. L., ROCKNE, R. C., BOONE, A. D., NEAL, M. L., HAWKINS-DAARUD, A., CORWIN, D. M., BRIDGE, C. A., GUYMAN, L. A., TRISTER, A. D., MRUGALA, M. M., ROCKHILL, J. K. & SWANSON, K. R. 2013. From patient-specific mathematical neuro-oncology to precision medicine. *Front Oncol,* 3**,** 1-11.

BALLABH, P., BRAUN, A. & NEDERGAARD, M. 2004. The blood-brain barrier: an overview: structure, regulation, and clinical implications. *Neurobiol Dis,* 16**,** 1-13.

BASKAR, R., LEE, K. A., YEO, R. & YEOH, K. W. 2012. Cancer and radiation therapy: current advances and future directions. *Int J Med Sci,* 9**,** 193-9.

BELSARE, A. D. 2012. Histopathological Image Analysis Using Image Processing Techniques: An Overview. *Signal & Image Processing : An International Journal,* 3**,** 23-36.

BERNAS, L. M., FOSTER, P. J. & RUTT, B. K. 2007. Magnetic resonance imaging of in vitro glioma cell invasion. *J Neurosurg,* 106**,** 306-13.

BHATTACHARJEE, S., MUKHERJEE, J., NAG, S., MAITRA, I. K. & BANDYOPADHYAY, S. K. 2014. Review on Histopathological Slide Analysis using Digital Microscopy. *International Journal of Advanced Science and Technology,* 62**,** 65-96.

BLASEL, S., FRANZ, K., ACKERMANN, H., WEIDAUER, S., ZANELLA, F. & HATTINGEN, E. 2011. Stripe-like increase of rCBV beyond the visible border of glioblastomas: site of tumor infiltration growing after neurosurgery. *J Neurooncol,* 103**,** 575-84.

BLOCH, F. 1946. Nuclear Induction. *Physical Review,* 70**,** 460-474.

BLYSTAD, I., WARNTJES, J. B. M., SMEDBY, O., LUNDBERG, P., LARSSON, E. M. & TISELL, A. 2017. Quantitative MRI for analysis of peritumoral edema in malignant gliomas. *PLoS One,* 12**,** e0177135.

BOGDANSKA, M. U., BODNAR, M., PIOTROWSKA, M. J., MUREK, M., SCHUCHT, P., BECK, J., MARTINEZ-GONZALEZ, A. & PEREZ-GARCIA, V. M. 2017. A mathematical model describes the malignant transformation of low grade gliomas: Prognostic implications. *PLoS One,* 12**,** e0179999.

BRODY, W. & ZERHOUNI, E. 2000. *Hand book of medical imaging processing and analysis,* USA, Academic Press.

BURNET, N. G., THOMAS, S. J., BURTON, K. E. & JEFFERIES, S. J. 2004. Defining the tumour and target volumes for radiotherapy. *Cancer Imaging,* 4**,** 153-61.

CANCER RESEARCH UK. 2019. *Cancer incidence statistics* [Online]. UK: Cancer research. [Accessed 12/8/2019].

CARANCI, F., POLONARA, G., CARRIERO, A., POPOLIZIO, T., MUTO, M., STECCO, A., POLLICE, S. & TARTARO, A. 2012. Imaging Gliomas After Treatment.

CARRUTHERS, R. D. 2015. *Response to ionising radiation of glioblastoma stem-like cells.* PhD, Glasgow university.

CASELLES, V., KIMMEL, R. & SAPIRO, G. 1997. Geodesic active contours. *International Journal of Computer Vision,* 22**,** 61-79.

CHA, S., JOHNSON, G., WADGHIRI, Y. Z., JIN, O., BABB, J., ZAGZAG, D. & TURNBULL, D. H. 2003. Dynamic, contrast-enhanced perfusion MRI in mouse gliomas: correlation with histopathology. *Magn Reson Med,* 49**,** 848-55.

CHAPPELOW, J., MADABHUSHI, A., ROSEN, M., TOMASZEWESKI, J. & FELDMAN, M. 2007. A combined feature ensemble basedmutual information scheme for robust inter-modal, inter-protocol image registration. *IEEE*.

CHEN, C. C. 2011. *Advances in the biology, imaging and therapies for glioblastoma,* Croatia, InTech.

CLAES, A., IDEMA, A. J. & WESSELING, P. 2007. Diffuse glioma growth: a guerilla war. *Acta Neuropathol,* 114**,** 443-58.

COPE, F. W. & DAMADIAN, R. 1970. Cell Potassium by 39K Spin Echo Nuclear Magnetic Resonance. *Nature,* 228**,** 76-77.

COQUERY, N., FRANCOIS, O., LEMASSON, B., DEBACKER, C., FARION, R., REMY, C. & BARBIER, E. L. 2014. Microvascular MRI and unsupervised clustering yields histology-resembling images in two rat models of glioma. *J Cereb Blood Flow Metab,* 34**,** 1354-62.

CUDDAPAH, V. A., ROBEL, S., WATKINS, S. & SONTHEIMER, H. 2014. A neurocentric perspective on glioma invasion. *Nat Rev Neurosci,* 15**,** 455-65.

CUENOD, C. A. & BALVAY, D. 2013. Perfusion and vascular permeability: basic concepts and measurement in DCE-CT and DCE-MRI. *Diagn Interv Imaging,* 94**,** 1187-204.

DAI, W., GARCIA, D., DE BAZELAIRE, C. & ALSOP, D. C. 2008. Continuous flow-driven inversion for arterial spin labeling using pulsed radio frequency and gradient fields. *Magn Reson Med,* 60**,** 1488-97.

DAUGUET, J., DELZESCAUX, T., CONDE, F., MANGIN, J. F., AYACHE, N., HANTRAYE, P. & FROUIN, V. 2007. Three-dimensional reconstruction of stained histological slices and 3D non-linear registration with in-vivo MRI for whole baboon brain. *J Neurosci Methods,* 164**,** 191-204.

DE GOOIJER, M. C., GUILLEN NAVARRO, M., BERNARDS, R., WURDINGER, T. & VAN TELLINGEN, O. 2018. An Experimenter's Guide to Glioblastoma Invasion Pathways. *Trends Mol Med,* 24**,** 763-780.

DE VLEESCHOUWER, S. 2017. *Glioblastoma,* Australia, Codon Publications.

DEMIRKAYA, O., ASYALI, M. H. & SAHOO, P. K. 2008. *Image processing with MATLAB: applications in medicine and biology*, Taylor and Francis group.

DETRE, J. A., WANG, J., WANG, Z. & RAO, H. 2009. Arterial spin-labeled perfusion MRI in basic and clinical neuroscience. *Curr Opin Neurol,* 22**,** 348-55.

DI COSTANZO, A., SCARABINO, T., TROJSI, F., GIANNATEMPO, G. M., POPOLIZIO, T., CATAPANO, D., BONAVITA, S., MAGGIALETTI, N., TOSETTI, M., SALVOLINI, U., D'ANGELO, V. A. & TEDESCHI, G. 2006. Multiparametric 3T MR approach to the assessment of cerebral gliomas: tumor extent and malignancy. *Neuroradiology,* 48**,** 622-31.

DIAZ, I., BOULANGER, P., GREINER, R. & MURTHA, A. 2011. A critical review of the effects of de-noising algorithms on MRI brain tumor segmentation. *Conf Proc IEEE Eng Med Biol Soc,* 2011**,** 3934-7.

DICE, L. R. 1945. Measures of the Amount of Ecologic Association Between Species. *Ecology,* 26**,** 297-302.

DOMINIETTO, M., RUDIN, M. 2014. Could magnetic resonance provide in vivo histology. *Frontiers in Genetics,* 4.

DOMINIETTO, M., TSINOREMAS, N. & CAPOBIANCO, E. 2015. Integrative analysis of cancer imaging readouts by networks. *Mol Oncol,* 9**,** 1-16.

DREVELEGAS, A. 2011. *Imaging of Brain Tumors with Histological Correlations,* Berlin, Springer.

EARNEST, F. T., KELLY, P. J., SCHEITHAUER, B. W., KALL, B. A., CASCINO, T. L., EHMAN, R. L., FORBES, G. S. & AXLEY, P. L. 1988. Cerebral astrocytomas: histopathologic correlation of MR and CT contrast enhancement with stereotactic biopsy. *Radiology,* 166**,** 823-7.

EIDEL, O., BURTH, S., NEUMANN, J. O., KIESLICH, P. J., SAHM, F., JUNGK, C., KICKINGEREDER, P., BICKELHAUPT, S., MUNDIYANAPURATH, S., BAUMER, P., WICK, W., SCHLEMMER, H. P., KIENING, K., UNTERBERG, A., BENDSZUS, M. & RADBRUCH, A. 2017. Tumor Infiltration in Enhancing and Non-Enhancing Parts of Glioblastoma: A Correlation with Histopathology. *PLoS One,* 12**,** e0169292.

ERDFELDER, E., FAUL, F. & BUCHNER, A. 1996. GPOWER: A general power analysis program. *Behavior Research Methods Instruments & Computers,* 28**,** 1-11.

FAGAN, A. J., MULLIN, J. M., GALLAGHER, L., HADLEY, D. M., MACRAE, I. M. & CONDON, B. 2008. Serial postmortem relaxometry in the normal rat brain and following stroke. *J Magn Reson Imaging,* 27**,** 469-75.

GARCIA-LORENZO, D., FRANCIS, S., NARAYANAN, S., ARNOLD, D. L. & COLLINS, D. L. 2013. Review of automatic segmentation methods of multiple sclerosis white matter lesions on conventional magnetic resonance imaging. *Med Image Anal,* 17**,** 1-18.

GEER, C. P., SIMONDS, J., ANVERY, A., CHEN, M. Y., BURDETTE, J. H., ZAPADKA, M. E., ELLIS, T. L., TATTER, S. B., LESSER, G. J., CHAN, M. D., MCMULLEN, K. P. & JOHNSON, A. J. 2012. Does MR perfusion imaging impact management decisions for patients with brain tumors? A prospective study. *AJNR Am J Neuroradiol,* 33**,** 556-62.

GERSTNER, E. R. & BATCHELOR, T. T. 2012. Antiangiogenic therapy for glioblastoma. *Cancer J,* 18**,** 45-50.

GHAFFARI, S., LEASK, R. L. & JONES, E. A. V. 2017. Blood flow can signal during angiogenesis not only through mechanotransduction, but also by affecting growth factor distribution. *Angiogenesis,* 20**,** 373-384.

GILLIES, R. J., SCHORNACK, P. A., SECOMB, T. W. & RAGHUNAND, N. 1999. Causes and effects of heterogeneous perfusion in tumors. *Neoplasia,* 1**,** 197-207.

GOLAY, HENDRIKSE, J. & LIM, T. C. 2004. Perfusion Imaging Using Arterial Spin Labeling. *Top Magn Reson Imaging,* 15.

GOMEZ-ROMAN, N., STEVENSON, K., GILMOUR, L., HAMILTON, G. & CHALMERS, A. J. 2017. A novel 3D human glioblastoma cell culture system for modeling drug and radiation responses. *Neuro Oncol,* 19**,** 229-241.

GONZALEZ, R. C. & WOODS, E. R. 2002. *digital image processing,* USA, Prentice-Hall.

GREGORI, J. 2015. *Arterial Spin Labeling (ASL) in Dementia* [Online]. 2015. Available: http://s434060124.online.de/aslindementiacms/basicprinciplesofasl2 [Accessed 2019].

GURCAN, M. N., BOUCHERON, L. E., CAN, A., MADABHUSHI, A., RAJPOOT, N. M. & YENER, B. 2009. Histopathological image analysis: a review. *IEEE Rev Biomed Eng,* 2**,** 147-71.

GUY, C. & FFYTCHE, D. 2005. *An Introduction to The Principles of Medical Imaging,* London, Imperial College Press.

HARDEE, M. E. & ZAGZAG, D. 2012. Mechanisms of glioma-associated neovascularization. *Am J Pathol,* 181**,** 1126-41.

HATTINGEN , E. & PILATUS, U. 2016. *Brain Tumor Imaging,* Berlin-Heidelberg, Springer.

HECKE, W. V., EMSELL, L. & SUNAERT, S. 2016. *Diffusion Tensor Imaging,* NewYork Springer.

HEJMADI, M. 2013. *Introduction to Cancer Biology*, Denmark, Ventus.

HENNING, E. C., AZUMA, C., SOTAK, C. H. & HELMER, K. G. 2007. Multispectral quantification of tissue types in a RIF-1 tumor model with histological validation. Part I. *Magn Reson Med,* 57**,** 501-12.

HEYN, C., BOWEN, C. V., RUTT, B. K. & FOSTER, P. J. 2005. Detection threshold of single SPIO-labeled cells with FIESTA. *Magn Reson Med,* 53**,** 312-20.

HILL, D. L. G. & HAWKES, D. J. 1994. Voxel similarity measures for automated image registration. *Proc. SPIE,* 2359**,** 205-216.

HOLASH, J., MAISONPIERRE, P. C., COMPTON, D., BOLAND, P., ALEXANDER, C. R., ZAGZAG, D., YANCOPOULOS, G. D. & WIEGAND, S. J. 1999. Vessel cooption, regression, and growth in tumors mediated by angiopoietins and VEGF. *Science,* 284**,** 1994-8.

HUISMAN, T. A. 2010. Diffusion-weighted and diffusion tensor imaging of the brain, made easy. *Cancer Imaging,* 10 S163-S171.

HYARE, H., THUST, S. & REES, J. 2017. Advanced MRI Techniques in the Monitoring of Treatment of Gliomas. *Curr Treat Options Neurol,* 19**,** 11.

INOUE, S., ICHIKAWA, T., KUROZUMI, K., MARUO, T., ONISHI, M., YOSHIDA, K., FUJII, K., KAMBARA, H., CHIOCCA, E. A. & DATE, I. 2012. Novel animal glioma models that separately exhibit two different invasive and angiogenic phenotypes of human glioblastomas. *World Neurosurg,* 78**,** 670-82.

JACOBS, V. L., VALDES, P. A., HICKEY, W. F. & DE LEO, J. A. 2011. Current review of in vivo GBM rodent models: emphasis on the CNS-1 tumour model. *ASN Neuro,* 3**,** e00063.

JAIN, K. K. 2018. A Critical Overview of Targeted Therapies for Glioblastoma. *Front Oncol,* 8**,** 419.

JARDIM-PERASSI, B. V., HUANG, S., DOMINGUEZ-VIQUEIRA, W., POLESZCZUK, J., BUDZEVICH, M. M., ABDALAH, M. A., PILLAI, S. R., RUIZ, E., BUI, M. M., ZUCCARI, D., GILLIES, R. J. & MARTINEZ, G. V. 2019. Multiparametric MRI and Coregistered Histology Identify Tumor Habitats in Breast Cancer Mouse Models. *Cancer Res,* 79**,** 3952-3964.

JARNUM, H., STEFFENSEN, E. G., KNUTSSON, L., FRUND, E. T., SIMONSEN, C. W., LUNDBYE-CHRISTENSEN, S., SHANKARANARAYANAN, A., ALSOP, D. C., JENSEN, F. T. & LARSSON, E. M. 2010. Perfusion MRI of brain tumours: a comparative study of pseudo-continuous arterial spin labelling and dynamic susceptibility contrast imaging. *Neuroradiology,* 52**,** 307-17.

JEGATHAMBAL, S. K., MOK, K., RUDKO, D. A. & SHMUEL, A. 2018. MRI Based Brain-Specific 3D-Printed Model Aligned to Stereotactic Space for Registering Histology to MRI. *Conf Proc IEEE Eng Med Biol Soc,* 2018**,** 802-805.

JENSEN, T. R. & SCHMAINDA, K. M. 2009. Computer-aided detection of brain tumor invasion using multiparametric MRI. *J Magn Reson Imaging,* 30**,** 481-9.

JOHNSON, D. R., OMURO, A. M. P., RAVELO, A., SOMMER, N., GUERIN, A., IONESCU-ITTU, R., SHI, S., MACALALAD, A. & UHM, J. H. 2018. Overall survival in patients with glioblastoma before and after bevacizumab approval. *Curr Med Res Opin,* 34**,** 813-820.

KALPATHY-CRAMER, J., GERSTNER, E. R., EMBLEM, K. E., ANDRONESI, O. & ROSEN, B. 2014. Advanced magnetic resonance imaging of the physical processes in human glioblastoma. *Cancer Res,* 74**,** 4622-4637.

KAO, H. W., CHIANG, S. W., CHUNG, H. W., TSAI, F. Y. & CHEN, C. Y. 2013. Advanced MR imaging of gliomas: an update. *Biomed Res Int*, 2013**,** 970586.

KARELLAS, A. & THOMADSEN, B. R. 2016. *Handbook of small animal imaging,* USA, Taylor & Francis Group.

KAZEROONI, F. A., MOHSENI, M., REZAEI, S., BAKHSHANDEHPOUR, G. & SALIGHEH RAD, H. 2015. Multi-parametric (ADC/PWI/T2-w) image fusion approach for accurate semi-automatic segmentation of tumorous regions in glioblastoma multiforme. *MAGMA,* 28**,** 13-22.

KELLY, P. J., DAUMAS-DUPORT, C., KISPERT, D. B., KALL, B. A., SCHEITHAUER, B. W. & ILLIG, J. J. 1987. Imaging-based stereotaxic serial biopsies in untreated intracranial glial neoplasms. *J Neurosurg,* 66**,** 865-74.

KENNETH W. FISHBEIN, J. C. M., AND RICHARD G. SPENCER Hardware for Magnetic Resonance Imaging.

KIESSLING, F. & PICHLER, B. J. 2011. *Small animal imaging basics and practical guide,* Germany, Springer.

KILKENNY, C., BROWNE, W., CUTHILL, I. C., EMERSON, M., ALTMAN, D. G. & GROUP, N. C. R. R. G. W. 2010. Animal research: reporting in vivo experiments: the ARRIVE guidelines. *Br J Pharmacol,* 160**,** 1577-9.

KIMT, T. S., SINGH, M. & SUNGKARA, W. 2000. Automatic registration of postmortem brain slices to MRI reference volume. *ICEE transactions on nuclear science,* 47**,** 1607-1613.

KONUKOGLU, E., CLATZ, O., BONDIAU, P. Y., DELINGETTE, H. & AYACHE, N. 2010. Extrapolating glioma invasion margin in brain magnetic resonance images: suggesting new irradiation margins. *Med Image Anal,* 14**,** 111-25.

KRAKHMAL, N. V., ZAVYALOVA, M. V., DENISOV, E. V., VTORUSHIN, S. V. & PERELMUTER, V. M. 2015. Cancer Invasion Patterns and Mechanisms. 7**,** 17-25.

LACROIX, M., ABI-SAID, D., FOURNEY, D. R., GOKASLAN, Z. L., SHI, W. M., DEMONTE, F., LANG, F. F., MCCUTCHEON, I. E., HASSENBUSCH, S. J., HOLLAND, E., HESS, K., MICHAEL, C., MILLER, D. & SAWAYA, R. 2001. A multivariate analysis of 416 patients with glioblastoma multiforme: prognosis, extent of resection, and survival. *Journal of Neurosurgery,* 95**,** 190-198.

LANGER, D. L., VAN DER KWAST, T. H., EVANS, A. J., TRACHTENBERG, J., WILSON, B. C. & HAIDER, M. A. 2009. Prostate cancer detection with multi-parametric MRI: logistic regression analysis of quantitative T2, diffusion-weighted imaging, and dynamic contrast-enhanced MRI. *J Magn Reson Imaging,* 30**,** 327-34.

LAUTERBUR, P. C. 1973. Image Formation by Induced Local Interactions: Examples Employing Nuclear Magnetic Resonance. *Nature,* 242(5394)**,** 190–191.

LE BIHAN, D., MANGIN, J. F., POUPON, C., CLARK, C. A., PAPPATA, S., MOLKO, N. & CHABRIAT, H. 2001. Diffusion tensor imaging: concepts and applications. *J Magn Reson Imaging,* 13**,** 534-46.

LEENDERS, W. P. J., KUSTERS, B. & DEWAAL, R. M. W. 2002. Vessel Co-Option: How Tumors Obtain Blood Supply in the Absence of Sprouting Angiogenesis. *Endothelium*.

LIN, L., XUE, Y., DUAN, Q., SUN, B., LIN, H., HUANG, X. & CHEN, X. 2016. The role of cerebral blood flow gradient in peritumoral edema for differentiation of glioblastomas from solitary metastatic lesions. *Oncotarget,* 7**,** 69051-69059.

LIU J., Li M., JianxinWang, Wu F., Liu T., Pan Y. 2014. A survey of MRI-based brain tumor segmentation methods. Tsinghua science and technology, 19, 578-595.

LIU, T. B., PERLIN, D. S. & XUE, C. 2012. Molecular mechanisms of cryptococcal meningitis. *Virulence,* 3**,** 173-81.

LOUIS, D. N., PERRY, A., REIFENBERGER, G., VON DEIMLING, A., FIGARELLA-BRANGER, D., CAVENEE, W. K., OHGAKI, H., WIESTLER, O. D., KLEIHUES, P. & ELLISON, D. W. 2016. The 2016 World Health Organization Classification of Tumors of the Central Nervous System: a summary. *Acta Neuropathol,* 131**,** 803-20.

MACHEIN, M. R. & PLATE, K. H. 2000. VEGF in brain tumors. *Journal of Neuro-Oncology,* 50**,** 109-120.

MADABHUSHI, A., FELDMAN, M. D., METAXAS, D. N., TOMASZEWESKI, J. & CHUTE, D. 2005. Automated detection of prostatic adenocarcinoma from high-resolution ex vivo MRI. *IEEE Trans Med Imaging,* 24**,** 1611-25.

MAINTZ, J. B. & VIERGEVER, M. A. 1998. A survey of medical image registration. *Med Image Anal,* 2**,** 1-36.

MANSFIELD, P. & GRANNELL, P. K. 1973. NMR 'diffraction' in solids? *Journal of Physics C: Solid State Physics,* 6**,** L422-L426.

MARINO, M. A., HELBICH, T., BALTZER, P. & PINKER-DOMENIG, K. 2018. Multiparametric MRI of the breast: A review. *J Magn Reson Imaging,* 47**,** 301-315.

MCCANN, M. T. 2015. *Tools for Automated Histology Image Analysis*. Doctor, Carnegie Mellon.

MCROBBIE, D. W., MOORE, E. A., GRAVES, M. J. & PRINCE, M. R. 2006. *MRI From Picture to Proton,* UK, Cambridge University Press.

MESCHER, A. L. 2016. *Junqueira's basic histology text and atlas,* USA, McGraw-Hill Education.

MORITANI, T., EKHOLM, S. & WESTESSON, P. L. 2005. *Diffusion-Weighted MR Imaging of the Brain,* Berlin Heidelberg, Springer.

MOUGIN, O. 2010. *Quantitative Methods in High Field MRI*. PhD, University of Nottingham.

MUJA, N. & BULTE, J. W. 2009. Magnetic resonance imaging of cells in experimental disease models. *Prog Nucl Magn Reson Spectrosc,* 55**,** 61-77.

MUKHERJEE, P., BERMAN, J. I., CHUNG, S. W., HESS, C. P. & HENRY, R. G. 2008. Diffusion tensor MR imaging and fiber tractography: theoretic underpinnings. *AJNR Am J Neuroradiol,* 29**,** 632-41.

NANDU, H., WEN, P. Y. & HUANG, R. Y. 2018. Imaging in neuro-oncology. *Ther Adv Neurol Disord,* 11**,** 1-19.

NIYAZI, M., BRADA, M., CHALMERS, A. J., COMBS, S. E., ERRIDGE, S. C., FIORENTINO, A., GROSU, A. L., LAGERWAARD, F. J., MINNITI, G., MIRIMANOFF, R. O., RICARDI, U., SHORT, S. C., WEBER, D. C. & BELKA, C. 2016. ESTRO-ACROP guideline "target delineation of glioblastomas". *Radiother Oncol,* 118**,** 35-42.

NOTH, U., TICHY, J., TRITT, S., BAHR, O., DEICHMANN, R. & HATTINGEN, E. 2019. Quantitative T1 mapping indicates tumor infiltration beyond the enhancing part of glioblastomas. *NMR Biomed***,** e4242.

OPPO, K., LEEN, E., ANGERSON, W. J., COOKE, T. G. & MCARDLE, C. S. 1998. Doppler perfusion index: an interobserver and intraobserver reproducibility study. *Radiology,* 208**,** 453-7.

OU, Y., SHEN, D., FELDMAN, M., TOMASZEWSKI, J. & DAVATZIKOS, C. 2009. Non-rigid registration between histological and MR images of the prostate: a joint segmentation and registration framework. *IEEE Computer Society Conference on Computer*. Miami, FL, USA: IEEE.

TRACQUI, G. C. C., D. E. WOODWARD, G. T. BARTOOLL, J. D. MURRAY AND E. C. ALVORD, JRLL 1995. A mathematical model of glioma growth: the effect of chemotherapy on spatio-temporal growth. *Cell ProliJ***,** 17-3 1.

PERONA, P. & MALIK, J. 1990. Scale-Space and Edge Detection Using Anisotropic Diffusion. *IEEE transactions on pattern analysis and machine intelligence,* 12**,** 629-639.

PERRIN, S. L., SAMUEL, M. S., KOSZYCA, B., BROWN, M. P., EBERT, L. M., OKSDATH, M. & GOMEZ, G. A. 2019. Glioblastoma heterogeneity and the tumour microenvironment: implications for preclinical research and development of new treatments. *Biochem Soc Trans*.

PETERS, S. R. 2003. The art of embedding tissue for frozen section part I: a system for precision face down cryoembedding of tissues using freezing temperture-embedding wells. *Journal of Histotechnology***,** 11-19.

PETERSEN, D. K. A., NYENGAARD, J. R. & GUNDERSEN, H. J. G. 2001. Tissue shrinkage and unbiased stereological estimation of particle number and size. *Journal of Microscopy,* 204.

PICHAT, J., IGLESIAS, J. E., YOUSRY, T., OURSELIN, S. & MODAT, M. 2018. A Survey of Methods for 3D Histology Reconstruction. *Med Image Anal,* 46**,** 73-105.

PIRTOLI, L. & GRAVINA, G. L. 2016. *Radiobiology of Glioblastoma Recent Advances and Related Pathobiology,* Switzerland, Springer International Publishing.

PRASAD, P. V. 2006. *Magnetic Resonance Imaging Methods and Biologic Applications,* New Jersey, Humana Press Inc.

PRICE, S. J. 2007. The role of advanced MR imaging in understanding brain tumour pathology. *Br J Neurosurg,* 21**,** 562-75.

PRICE, S. J. & GILLARD, J. H. 2011. Imaging biomarkers of brain tumour margin and tumour invasion. *Br J Radiol,* 84 Spec No 2**,** S159-67.

QUINN, G. P. & KEOUGH, M. J. 2002. *Experimental Design and Data Analysis for Biologists,* U.K., Cambridge University.

RABI, I. I., ZACHARIAS, J. R., MILLMAN, S. & KUSCH, P. 1938. A New Method of Measuring Nuclear Magnetic Moment. *Physical Review,* 53**,** 318-318.

RAY, K. S. 2010. *Glioblastoma molecular mechanisms of pathogenesis and current therapeutic strategies,* USA, Springer.

ROY, S., KUMAR JAIN, A., LAL, S. & KINI, J. 2018. A study about color normalization methods for histopathology images. *Micron,* 114**,** 42-61.

ROY, S., NAG , S., MAITRA, I. K. & BANDYOPADHYAY, S. K. 2013. A Review on Automated Brain Tumor Detection and Segmentation from MRI of Brain. *International Journal of Advanced Research in Computer Science and Software Engineering,* 3**,** 1706-1746.

SHIROISHI, M. S., CASTELLAZZI, G., BOXERMAN, J. L., D'AMORE, F., ESSIG, M., NGUYEN, T. B., PROVENZALE, J. M., ENTERLINE, D. S., ANZALONE, N., DORFLER, A., ROVIRA, A., WINTERMARK, M. & LAW, M. 2015. Principles of T2 *-weighted dynamic susceptibility contrast MRI technique in brain tumor imaging. *J Magn Reson Imaging,* 41**,** 296-313.

STEELE, B., CHANDLER, J. & REDDY, S. 2016. *Algorithms for data science,* Switzerland, Springer.

STEJSKAL, E. O. & TANNER, J. E. 1965. Spin Diffusion Measurements: Spin Echoes in the Presence of a Time-Dependent Field Gradient. *Journal of Chemical Physics,* 42**,** 288-+.

STERNBERG, E. J., LIPTON, M. L. & BURNS, J. 2014. Utility of Diffusion Tensor Imaging in Evaluation of the Peritumoral Region in Patients with Primary and Metastatic Brain Tumors. *American Journal of Neuroradiology,* 35**,** 439-444.

STILLE, M., SMITH, E. J., CRUM, W. R. & MODO, M. 2013. 3D reconstruction of 2D fluorescence histology images and registration with in vivo MR images: application in a rodent stroke model. *J Neurosci Methods,* 219**,** 27-40.

SURI, J. S., WILSON, D. L. & LAXMINARAYAN, S. 2005. *Handbook of Biomedical Image Analysis,* New York, Kluwer Academic / Plenum Publishers.

SWANSON, K. R., ALVORD, E. C., JR. & MURRAY, J. D. 2002. Virtual brain tumours (gliomas) enhance the reality of medical imaging and highlight inadequacies of current therapy. *Br J Cancer,* 86**,** 14-8.

SWANSON, K. R., BRIDGE, C., MURRAY, J. D. & ALVORD, E. C. 2003. Virtual and real brain tumors: using mathematical modeling to quantify glioma growth and invasion. *Journal of the Neurological Sciences,* 216**,** 1-10.

SZENDE, B. & SUBA, Z. 1999. *Introduction to Histopathology,* Germany, Medicina publishing co.

TOURDIAS, T., RODRIGO, S., OPPENHEIM, C., NAGGARA, O., VARLET, P., AMOUSSA, S., CALMON, G., ROUX, F. X. & MEDER, J. F. 2008. Pulsed arterial spin labeling applications in brain tumors: practical review. *J Neuroradiol,* 35**,** 79-89.

VALLATOS, A., AL-MUBARAK, H. F. I., BIRCH, J. L., GALLLAGHER, L., MULLIN, J. M., GILMOUR, L., HOLMES, W. M. & CHALMERS, A. J. 2018a. Quantitative histopathologic assessment of perfusion MRI as a marker of glioblastoma cell infiltration in and beyond the peritumoral edema region. *J Magn Reson Imaging,* 50**,** 529-540.

VALLATOS, A., GILMOUR, L., CHALMERS, A. J. & HOLMES, W. M. 2018b. Multiple boli arterial spin labeling for high signal-to-noise rodent brain perfusion imaging. *Magnetic Resonance in Medicine,* 79**,** 1020-1030.

VERGARA, J. R. & ESTÉVEZ, P. A. 2013. A review of feature selection methods based on mutual information. *Neural Computing and Applications,* 24**,** 175-186.

VICENT C., KIMMEL, R., SAPIRO, G. 1997. Geodesic Active Contours. *International Journal of Computer Vision,* 22(1)**,** 61–79.

VILLANUEVA-MEYER, J. E., MABRAY, M. C. & CHA, S. 2017. Current Clinical Brain Tumor Imaging. *Neurosurgery,* 81**,** 397-415.

WALLNER, B.K., EDELMAN R.R., BAJAKIAN R.L., KLEEFIELD J., ATKINSON D.J., MATTLE, H.P. 1990. Signal Normalization in Surface-Coil MR Imaging. American Society of Neuroradiology, 1271-1272.

WATKINS, S., ROBEL, S., KIMBROUGH, I. F., ROBERT, S. M., ELLIS-DAVIES, G. & SONTHEIMER, H. 2014. Disruption of astrocyte-vascular coupling and the blood-brain barrier by invading glioma cells. *Nat Commun,* 5**,** 4196.

WEINBERG, R. A. 2007. *The Biology of cancer,* USA, Garland Science,Taylor & Francis Group.

WEISHAUPT, D., KÖCHLI, V. D. & MARINCEK, B. 2006. *How Does MRI Work ?,* Verlag Berlin Heidelberg, Springer.

WELLS, W. M., 3RD, VIOLA, P., ATSUMI, H., NAKAJIMA, S. & KIKINIS, R. 1996. Multi-modal volume registration by maximization of mutual information. *Med Image Anal,* 1, 35-51.

WESTBROOK, C., ROTH, C. K. & TALBOT, J. 2011. *MRI in Practice,* U.K., A John Wiley & Sons, Ltd.

WHITE, N. S., MCDONALD, C., FARID, N., KUPERMAN, J., KAROW, D., SCHENKER-AHMED, N. M., BARTSCH, H., RAKOW-PENNER, R., HOLLAND, D., SHABAIK, A., BJORNERUD, A., HOPE, T., HATTANGADI-GLUTH, J., LISS, M., PARSONS, J. K., CHEN, C. C., RAMAN, S., MARGOLIS, D., REITER, R. E., MARKS, L., KESARI, S., MUNDT, A. J., KANE, C. J., CARTER, B. S., BRADLEY, W. G. & DALE, A. M. 2014. Diffusion-weighted imaging in cancer: physical foundations and applications of restriction spectrum imaging. *Cancer Res,* 74, 4638-52.

WORKMAN, P. A., E. O.BALKWILL, F.BALMAIN, A.BRUDER, G.CHAPLIN, D. J.DOUBLE, J. A.EVERITT, J.FARNINGHAM, D. A.GLENNIE, M. J.KELLAND, L. R.ROBINSON, V.STRATFORD, I. J.TOZER, G. M.WATSON, S.WEDGE, S. R.ECCLES, S. A. 2010. Guidelines for the welfare and use of animals in cancer research. *Br J Cancer,* 102, 1555-77.

WU, O., DIJKHUIZEN, R. M. & SORENSEN, A. G. 2010. Multiparametric magnetic resonance imaging of brain disorders. *Top Magn Reson Imaging,* 21, 129-38.

YANKEELOV, T. E., PICKENS, D. R. & PRICE, R. R. 2012. *Quantitative MRI in Cancer*, Taylor & Francis Group, LLC.

YEOM, K. W., MITCHELL, L. A., LOBER, R. M., BARNES, P. D., VOGEL, H., FISHER, P. G. & EDWARDS, M. S. 2014. Arterial spin-labeled perfusion of pediatric brain tumors. *AJNR Am J Neuroradiol,* 35, 395-401.

ZAGZAG, D., ESENCAY, M., MENDEZ, O., YEE, H., SMIRNOVA, I., HUANG, Y., CHIRIBOGA, L., LUKYANOV, E., LIU, M. & NEWCOMB, E. W. 2008. Hypoxia- and vascular endothelial growth factor-induced stromal cell-derived factor-1alpha/CXCR4 expression in glioblastomas: one plausible explanation of Scherer's structures. *Am J Pathol,* 173, 545-60.

ZHANG, Z., JIANG, H., CHEN, X., BAI, J., CUI, Y., REN, X., CHEN, X., WANG, J., ZENG, W. & LIN, S. 2014. Identifying the survival subtypes of glioblastoma by quantitative volumetric analysis of MRI. *J Neurooncol,* 119, 207-14.

ZOU, K. H., WARFIELD, S. K., BHARATHA, A., TEMPANY, C. M. C., KAUS, M. R., HAKER, S. J., WELLS, W. M., JOLESZ, F. A. & KIKINIS, R. 2004. Statistical validation of image segmentation quality based on a spatial overlap index1. *Academic Radiology,* 11, 178-189.